

**LASER PROCESSING OF SOLUTION  
BASED ANTIMONY DOPED TIN  
OXIDE THIN FILMS**

**Neranga Udayangani Abeywickrama**

A thesis submitted in partial fulfilment of the requirements of  
Nottingham Trent University for the degree of Doctor of Philosophy

School of Science and Technology  
Nottingham Trent University

**March 2013**

## **Declaration**

This work is the intellectual property of the author, and may also be owned by the research sponsor and/or Nottingham Trent University. You may copy up to 5% of this work for private study, or personal, non-commercial research. Any re-use of the information contained within this document should be fully referenced, quoting the author, title, university, degree level and pagination. Queries or requests for any other use, or if a more substantial copy is required, should be directed in the first instance to the author.

## Abstract

Antimony doped Tin oxide ( $\text{SnO}_2\text{:Sb}$ , or ATO) is of interest as an alternative to Indium Tin Oxide (ITO) for large area optoelectronic applications. There is a particular interest in the potential for solution based coatings based on nanoparticulate suspensions of  $\text{SnO}_2\text{:Sb}$ . However, solution processed films typically require a high temperature ( $\sim 700^\circ\text{C}$ ) annealing step to achieve the desired electrical and optical properties. This is disadvantageous for applications that would benefit from low cost, low temperature/flexible substrates. As an alternative to conventional high temperature annealing, excimer laser processing can provide highly localized energy dissipation, and is an attractive technique to functionalise coated materials. Therefore the work presented in this thesis investigates the use of excimer laser processing to optimise the electrical and optical properties of solution deposited  $\text{SnO}_2\text{:Sb}$  thin films for use in electroluminescent display devices.

Thin films of  $\text{SnO}_2\text{:Sb}$  were deposited using dip coating, inkjet printing and the spin coating technique. By varying the numbers of spin coatings deposited, a series of samples were prepared on Eagle XG glass substrates with different thicknesses of  $\text{SnO}_2\text{:Sb}$  (ranging from  $0.2\ \mu\text{m}$  to  $1.4\ \mu\text{m}$ ). The initial sheet resistance, optical transmission and crystal structure of the deposited films was studied. The films were subsequently post processed using three different annealing techniques: (i) Laser Processing: samples were laser processed in air to optimise the sheet resistance and optical transmission. Excimer (KrF, 248 nm, 20 ns pulse) irradiation of between 1 and 1000 pulses was applied at fluences in the range  $20\text{-}70\ \text{mJ}/\text{cm}^2$ . (ii) Thermal Annealing: samples were thermally annealed at temperatures in the range  $100^\circ\text{C}$  -  $700^\circ\text{C}$  in air. (iii) Combined Processing: samples were initially annealed in air at temperatures in the range  $100^\circ\text{C}$  -  $400^\circ\text{C}$  and then KrF laser processed with the optimum laser fluence ( $60\ \text{mJ}/\text{cm}^2$ ) and number of laser pulses (1000). It has been found that grain boundary scattering limits the electron conduction when films were laser processed or low temperature thermal annealed and with higher temperature thermal annealing ionized impurity scattering dominates.

The sheet resistance of the as-deposited films were in the  $\text{M}\Omega$  range with the optical transmission was  $>85\%$  (at 550 nm). Further to KrF laser processing, the sheet resistance of the  $\text{SnO}_2\text{:Sb}$  films was reduced to around  $20\ \text{k}\Omega/\text{sq}$  and the optical transmission remained  $>75\%$ . The films that were thermally annealed at  $700^\circ\text{C}$  showed a resultant sheet resistance of around  $120\ \Omega/\text{sq}$ , and the combined processed films showed a resultant sheet resistance of  $700\ \Omega/\text{sq}$ , which facilitated use as transparent electrodes in electroluminescent device fabrication. TEM studies indicated grain growth associated with the post processing for all three techniques, and Hall effect measurement confirms improvement in carrier concentration (i.e.  $2 \times 10^{19}\ \text{cm}^{-3}$  for KrF laser processed films and  $2.8 \times 10^{20}\ \text{cm}^{-3}$  for thermally annealed films as compared to  $1.8 \times 10^{17}\ \text{cm}^{-3}$  for as-deposited).

Luminescent studies of Alternating Current Electroluminescent (ACEL) display devices fabricated with spin coated  $\text{SnO}_2\text{:Sb}$  transparent electrodes showed that the combined processing of low temperature thermal annealing ( $400^\circ\text{C}$ ) followed by laser treatment gives the same order of luminescence as high temperature ( $700^\circ\text{C}$ ) processed devices. The results presented demonstrated that spin coating deposition followed by combined low temperature/photonic post processing offers the potential to use solution processed  $\text{SnO}_2\text{:Sb}$  layers for low temperature, low cost transparent electrode applications.

## **Acknowledgement**

This research work was part of Technology Strategy Board (TSB) funded research program - FAB3D, in collaboration with Printed Electronics Ltd., Keeling and Walker Ltd., Oxley Developments Ltd., Johnson Matthey, Intrinsic Materials and Brunel University. The author would like to acknowledge TSB for the financial support and the collaborative partners for their support.

Firstly and for mostly I would like to express my sincere thanks to my Director of Studies Prof. Wayne Cranton for giving me this opportunity to do this research work and also his vision, supervision and guidance to complete this work. He has supported me throughout my work and often encouraged me to dig deeper into my research. Words simply cannot express my gratitude to him. I am also indebted to my second supervisors Dr. Demosthenes Koutsogeorgis and Dr. Robert Ranson for their supervision, guidance and encourage throughout my work. This work would not have been completed without your direction and support.

Many thanks go to Dr. Steve Jones at Printed Electronic Ltd for giving me the opportunity to training on their inkjet printing system and print my own samples. Also I would like to acknowledge Dr. Paul Harris, Brunel University, UK and Andy Spiller, Keeling & Walker Ltd, UK for their support throughout the project by providing samples and helping with the characterisation.

At Nottingham Trent University, I would like to thank Dr. Costas Tsakonas, for his support and invaluable knowledge throughout my work. Also I would like to thank Prof. Bob Stevens for his support during my writing up work. Thank you to Dr. Gary Hix with the XRD work and Dr. David Belton and Gordon Arnott for their assistance with the SEM. I would like to acknowledge my colleagues Dr. Gabriel Boutaud, Dr. Thomas Miller, Carly Farrow and Khairi Abusabee for their encouragement and help.

Lastly and most importantly my everlasting gratitude goes to my lovely family for their endless encouragement, support and love throughout this work. Special thank goes to my husband Hasitha, little daughter Senudi and all the immediate family back in Sri Lanka specially including my parents for their continuous and unconditional love, support and financial help throughout my studies. You all are the true meaning of my life and would like to dedicate this thesis to you all.

# Contents

Declaration.....	ii
Abstract.....	iii
Acknowledgement .....	iv
List of Figures.....	ix
List of Tables .....	xii
Abbreviations and symbols.....	xiii
Variables .....	xiv
<b>1. INTRODUCTION .....</b>	<b>1-1</b>
<b>1.1 Overview.....</b>	<b>1-1</b>
<b>1.2 Aims and Objectives .....</b>	<b>1-2</b>
1.2.1. Objectives.....	1-3
<b>1.2 Research collaboration .....</b>	<b>1-3</b>
<b>1.4 Structure of the thesis .....</b>	<b>1-4</b>
<b>2. BACKGROUND REVIEW &amp; THEORY .....</b>	<b>2-1</b>
<b>2.1 Transparent conducting oxides .....</b>	<b>2-1</b>
2.1.1. Introduction.....	2-1
2.1.2. Electron band structure of TCOs .....	2-4
2.1.3. Optical properties of TCOs .....	2-5
2.1.3.1 Strong absorption region .....	2-6
2.1.3.2 Infrared region .....	2-8
2.1.4. Electrical conduction of TCOs.....	2-9
2.1.4.1 Grain boundary scattering .....	2-10
2.1.4.2 Ionized impurity scattering .....	2-11
2.1.4.3 Neutral impurity scattering.....	2-11
<b>2.2 Tin oxide .....</b>	<b>2-12</b>
2.2.1. Structure of SnO <sub>2</sub> .....	2-12
2.2.2. Antimony doped Tin Oxide .....	2-14
2.2.3. Antimony doped Tin Oxide vs other TCOs.....	2-16
<b>2.3 TCO deposition techniques .....</b>	<b>2-16</b>
2.3.1. Sputter deposition.....	2-18
2.3.2. Dip coating.....	2-19
2.3.3. Spin coating .....	2-20
2.3.4. Spray pyrolysis .....	2-22
<b>2.4 Inkjet printing technology .....</b>	<b>2-23</b>
2.4.1. Continuous inkjet printing .....	2-23
2.4.2. Drop on demand (DOD) inkjet printing .....	2-24
<b>2.5 Post processing of TCOs .....</b>	<b>2-26</b>
2.5.1. Thermal annealing .....	2-27
2.5.2. Photonic processing .....	2-29

<b>2.6 Applications of TCOs</b> .....	<b>2-31</b>
2.6.1. Display devices .....	2-31
2.6.2. Solar cells .....	2-31
2.6.3 Gas sensors .....	2-32
2.6.4 Low emissivity windows in buildings .....	2-33
2.6.5. Defrosting windows .....	2-33
2.6.6. Other applications .....	2-34
<b>3 EXPERIMENTAL PROCEDURES</b> .....	<b>3-1</b>
<b>3.1 Introduction</b> .....	<b>3-1</b>
<b>3.2 Thin film deposition technologies</b> .....	<b>3-1</b>
3.2.1 SnO <sub>2</sub> :Sb ink preparation and Spin Coating technique .....	3-1
3.2.2 Inkjet printing system .....	3-2
<b>3.3 Processing Technologies</b> .....	<b>3-4</b>
3.3.1 Laser Processing system .....	3-4
<b>3.4 Metrology systems</b> .....	<b>3-5</b>
3.4.1 Optical transmission .....	3-5
3.4.2 Surface roughness and step height .....	3-7
3.4.3 Surface morphology .....	3-8
3.4.3.1 Transmission Electron Microscopy (TEM) .....	3-8
3.4.3.2. Scanning Electron Microscopy (SEM) .....	3-9
3.4.4 X-ray diffraction (XRD) .....	3-10
3.4.5 X-ray Photoelectron Spectrometry (XPS) .....	3-12
3.4.6 Sheet resistance .....	3-13
3.4.6.1 Four Point Probe .....	3-13
3.4.6.2 Van der Pauw technique .....	3-15
3.4.7 Hall Effect .....	3-16
<b>4. POST PROCESSING OF INKJET PRINTED AND DIP COATED SnO<sub>2</sub>:Sb</b> .....	<b>4-1</b>
<b>4.1 Introduction</b> .....	<b>4-1</b>
<b>4.2 Dip coated SnO<sub>2</sub>:Sb on glass substrate</b> .....	<b>4-1</b>
4.2.1 Electrical and optical characterisation of as-deposited SnO <sub>2</sub> :Sb .....	4-3
4.2.2 Excimer laser processing of Dip coated SnO <sub>2</sub> :Sb .....	4-5
<b>4.3 Inkjet printing of SnO<sub>2</sub>:Sb</b> .....	<b>4-10</b>
4.3.1 Excimer laser processing of inkjet printed SnO <sub>2</sub> :Sb .....	4-12
4.3.2 Thermal annealing and laser processing of Inkjet printed SnO <sub>2</sub> :Sb .....	4-13
4.3.3 Coffee ring effect .....	4-15
4.3.3.1 Damming structures .....	4-15
4.3.3.2 Drying conditions .....	4-16
<b>4.4 Summary and Discussion</b> .....	<b>4-19</b>
<b>5. POST PROCESSING OF SPIN COATED SnO<sub>2</sub>:Sb</b> .....	<b>5-1</b>
<b>5.1 Introduction</b> .....	<b>5-1</b>
<b>5.2 Thickness optimisation of as- deposit SnO<sub>2</sub>:Sb layers</b> .....	<b>5-2</b>
5.2.1 Sheet Resistance .....	5-2
5.2.2 Film thickness .....	5-4

5.2.3 Transmission .....	5-5
5.2.4 XRD .....	5-7
<b>5.3 Thermal annealing of the spin coated SnO<sub>2</sub>:Sb.....</b>	<b>5-9</b>
5.3.1 Sheet resistance .....	5-9
5.3.2 Transmission.....	5-10
5.3.3 XRD .....	5-11
<b>5.4 Excimer laser processing of spin coated SnO<sub>2</sub>:Sb layers .....</b>	<b>5-13</b>
5.4.1 KrF laser processing of different thickness spin coated SnO <sub>2</sub> :Sb.....	5-14
5.4.1.1 Sheet resistance .....	5-14
5.4.1.2 Optical transmission.....	5-16
5.4.1.3 XRD.....	5-17
5.4.2 ArF laser processing of spin coated SnO <sub>2</sub> :Sb .....	5-19
5.4.2.1 Sheet resistance .....	5-20
<b>5.5 Combined processing-Thermal annealing followed laser processing of SnO<sub>2</sub>:Sb .....</b>	<b>5-21</b>
5.5.1 Lower temperature thermal annealing of different thickness SnO <sub>2</sub> :Sb .....	5-21
5.5.1 Excimer laser processing of the thermal annealed different thickness SnO <sub>2</sub> :Sb.....	5-23
<b>5.6 Discussion: .....</b>	<b>5-25</b>
<b>6. ANALYSIS &amp; CONDUCTION MECHANISM OF SPIN COATED SnO<sub>2</sub>:Sb .....</b>	<b>6-1</b>
<b>6.1 Introduction .....</b>	<b>6-1</b>
<b>6.2 Analysis of spin coated SnO<sub>2</sub>:Sb films .....</b>	<b>6-2</b>
6.2.1 Electrical properties.....	6-2
6.2.2 Optical properties.....	6-5
6.2.3 Structure and morphology .....	6-9
6.2.3.1. As-deposited SnO <sub>2</sub> :Sb.....	6-12
6.2.3.3 Excimer laser processed SnO <sub>2</sub> :Sb .....	6-15
6.2.4. Chemical composition and oxidation states.....	6-16
<b>6.3 Some thoughts on the conduction mechanism of spin coated SnO<sub>2</sub>:Sb .....</b>	<b>6-20</b>
<b>6.4 Key findings and summary .....</b>	<b>6-23</b>
6.4.1. As-deposited SnO <sub>2</sub> :Sb .....	6-23
6.4.2. Thermal annealed SnO <sub>2</sub> :Sb .....	6-24
6.4.3 Excimer laser processed SnO <sub>2</sub> :Sb .....	6-24
<b>7. ACEL DEVICE FABRICATION AND CHARACTERISATION.....</b>	<b>7-1</b>
<b>7.1 Introduction .....</b>	<b>7-1</b>
<b>7.2 Alternating Current Electroluminescent (ACEL) Display devices .....</b>	<b>7-1</b>
7.2.1. Introduction.....	7-1
7.2.2. Device structure and operation of ACEL .....	7-2
<b>7.3 ACEL device fabrication.....</b>	<b>7-5</b>
7.3.1. Post processing of transparent electrode layer.....	7-5
7.3.1. Fabrication of other layers .....	7-8
<b>7.4 ACEL device characterisation.....</b>	<b>7-8</b>
<b>7.5 Discussion .....</b>	<b>7-11</b>

<b>8. CONCLUSIONS AND FUTURE WORK .....</b>	<b>8-I</b>
<b>8.1 Conclusions .....</b>	<b>8-I</b>
<b>8.2 Future Work .....</b>	<b>8-I</b>

**List of References**

**APPENDIX A. List of presentations**

**APPENDIX B. Excimer Laser processing of  $Y_2O_3:Eu$**

**APPENDIX C. Comparison of sheet resistance measured by four point probes and using Hall Effect data**

## List of Figures

Figure 2.1 : Schematic diagram of the optical window of TCOs [28] $\lambda_{bg}$ and $\lambda_p$ are the wavelengths where band gap absorption and free electron absorption takes place .....	2-2
Figure 2.2 : Electron band structure of (a) TCO host (b) Degeneracy doped TCO (c) density of states of degeneracy doped TCO [32].....	2-5
Figure 2.3 : Transmission spectrum of TCO thin films [28].....	2-6
Figure 2.4 : $(\alpha h\nu)^2$ dependence on the photon energy of TCO grown at different temperatures [35] ....	2-7
Figure 2.5 : The sketch of (a) grain boundary scattering with low degree of crystallinity (b) Ionized impurity scattering in TCO [38] .....	2-11
Figure 2.6 : Crystal structure of SnO <sub>2</sub> [34]. .....	2-12
Figure 2.7 : Thin film deposition processes: CVD- Chemical vapour deposition, PLD- pulsed laser deposition, MBE-Molecular beam epitaxy; ARE- Activated reactive evaporation, ICBD-Ionized Cluster Beam Epitaxy .....	2-17
Figure 2.8 : Schematic diagram of dip coating.....	2-19
Figure 2.9 : Schematic diagram of the substrate positioning during spin coating.....	2-21
Figure 2.10 : Schematic diagram of continuous inkjet printer-multiple deflection system.....	2-24
Figure 2.11 : Piezoelectric inkjet designs (a) Bend mode (b) Push mode (c) Shear mode.....	2-25
Figure 2.12 : Schematic diagram of flash lamp annealing system [71].....	2-29
Figure 3.1 : Inkjet printing facilities at PEL (a) High precision inkjet printing system (b) Xaar printer head setup .....	3-3
Figure 3.2 : Schematic of KrF laser processing system showing the homogenised beam delivery system and sample stage.....	3-4
Figure 3.3 : Filmetrics F20 set up configuration for transmission measurements.....	3-6
Figure 3.4 : Schematic setup of the Wyko NT1100 system for optical profiling [90].....	3-7
Figure 3.5 : The reduced form of Scanning Electron Microscope [94]. .....	3-10
Figure 3.6 : Schematic of X-ray diffractometer [95] .....	3-11
Figure 3.7 : Schematic drawing of the linear four point probe.....	3-14
Figure 3.8 : Geometry of the Van der Pauw technique for measurement of sheet resistivity.....	3-15
Figure 3.9 : The standard geometry for the Hall Effect .....	3-16
Figure 4.1 : Sheet resistance variation of the as-deposited dip coated SnO <sub>2</sub> :Sb. ....	4-3
Figure 4.2(a) : KrF laser ablated area of dip coated SnO <sub>2</sub> :Sb film .....	4-4
Figure 4.3 : The variation in sheet resistance pre and post laser processing as a function of number of pulses and laser fluence. ....	4-6
Figure 4.4 : XRD of as-deposited and laser processed dip coated SnO <sub>2</sub> :Sb.....	4-7
Figure 4.5 :Transmission spectra for dip coated SnO <sub>2</sub> :Sb on glass substrate laser processed with (a) 20 mJ.cm <sup>-2</sup> (b) 40 mJ.cm <sup>-2</sup> .....	4-9

Figure 4.6 : Inkjet printed (3 passes) SnO <sub>2</sub> :Sb onto Eagle XG glass substrate (top) and photo paper (bottom).....	4-10
Figure 4.7 : Initial sheet resistance of inkjet printed SnO <sub>2</sub> :Sb on glass substrates. ....	4-12
Figure 4.8 : The variation in sheet resistance of inkjet printed SnO <sub>2</sub> :Sb as a function of number of laser pulses and laser fluence. ....	4-13
Figure 4.9 : The variation of sheet resistance post laser processing as a function of number of laser pulses and laser fluence for thermal annealed SnO <sub>2</sub> :Sb.....	4-14
Figure 4.10 : SnO <sub>2</sub> :Sb layers building up with in the UV wall for (a) 1 inkjet pass (b) 3 inkjet passes and (c) 6 inkjet passes.....	4-16
Figure 4.11: Inkjet printed SnO <sub>2</sub> :Sb: Oven dried at different temperatures (a) 120°C (b) 80°C.....	4-17
Figure 4.12 : Inkjet printed SnO <sub>2</sub> :Sb: oven dried at 80°C for 1 hr (a) in air (b) in vacuum .....	4-18
Figure 5.1 : Sheet resistance variation between batches of different thickness SnO <sub>2</sub> :Sb .....	5-3
Figure 5.2: Spin coated SnO <sub>2</sub> :Sb layers on Eagle XG glass substrate : left-12 spun layers right- 6 spun layers.....	5-4
Figure 5.3 : Measured film thickness of as- deposited SnO <sub>2</sub> :Sb vs number of spun layers .....	5-5
Figure 5.4 : Transmission variation with respect to the film thickness of the as-deposited SnO <sub>2</sub> :Sb .....	5-6
Figure 5.5 : Sheet resistance and optical transmission at 550 nm variation with respect to film thickness of as-deposited SnO <sub>2</sub> :Sb .....	5-6
Figure 5.6 : XRD patterns of as-deposited spin coated SnO <sub>2</sub> :Sb layers.....	5-7
Figure 5.7 : Sheet resistance variation of the spin coated SnO <sub>2</sub> :Sb layers with thermal anneal temperature .....	5-10
Figure 5.8 : Transmission spectra of the thermal annealed SnO <sub>2</sub> :Sb layers .....	5-11
Figure 5.9 : XRD patterns of thermal annealed SnO <sub>2</sub> :Sb layers .....	5-12
Figure 5.10: Post KrF laser annealing sheet resistance variation of spin coated 1100 nm thickness SnO <sub>2</sub> :Sb films with respect to number of laser pulses and laser fluence. The zero point represents the as-deposited sheet resistance .....	5-15
Figure 5.11 : Post KrF laser annealing sheet resistance variation of spin coated 190 nm thickness SnO <sub>2</sub> :Sb films with respect to number of laser pulses and laser fluence. ....	5-15
Figure 5.12 : Variation of the transmission of spin coated SnO <sub>2</sub> :Sb films KrF laser processed with 20,40,50 and 60 mJ.cm <sup>-2</sup> at 1000 pulses. ....	5-16
Figure 5.13 : Variation of the transmission of spin coated SnO <sub>2</sub> :Sb films KrF laser processed at 60 mJ.cm <sup>-2</sup> with 1,10,100 and 1000 pulses. ....	5-17
Figure 5.14 : XRD patterns of spin coated SnO <sub>2</sub> :Sb samples KrF laser processed at 60 mJ.cm <sup>-2</sup> with different number of laser pulses. ....	5-18
Figure 5.15 : Post ArF laser annealing sheet resistance variation of spin coated 1100 nm thickness SnO <sub>2</sub> :Sb films with respect to number of laser pulses and laser fluence. ....	5-20
Figure 5.16 : Variation of the sheet resistance with SnO <sub>2</sub> :Sb film thickness for thermal annealed at 400°C films and combined processed films. ....	5-24

Figure 6.1 : Carrier mobility and carrier concentration variation of spin coated SnO <sub>2</sub> :Sb films as a function of (a) thermal annealed temperature (b) excimer laser fluence .....	6-4
Figure 6.2 : Transmission (above) and Reflection spectra (bellow) of: As-deposited, thermal annealed (TA), and Excimer laser processed (LA) at 60 mJ.cm <sup>-2</sup> , SnO <sub>2</sub> :Sb .....	6-5
Figure 6.3 : Variation of absorption coefficient ( $\alpha$ ) with wavelength of as-deposited SnO <sub>2</sub> :Sb .....	6-6
Figure 6.4 : Representative absorption curves of thermal annealed SnO <sub>2</sub> :Sb for optical band gap extraction. ....	6-7
Figure 6.5 : Representative absorption curves of laser processed at 60mJ/cm <sup>2</sup> SnO <sub>2</sub> :Sb for optical band gap extraction.....	6-8
Figure 6.6 : TEM cross section of a 10 layers SnO <sub>2</sub> :Sb coating on glass substrate. ....	6-12
Figure 6.7 : Electron diffraction pattern of the as-deposited SnO <sub>2</sub> :Sb layer – where the rings correspond to lattice spacings of: A= 0.3345 Å, B= 0.2652 Å, C= 0.2365 Å, D= 0.1747 Å, E= 0.1634 Å, F= 0.1544 Å and G= 0.1418 Å.....	6-13
Figure 6.8 : Cross sectional TEM of SnO <sub>2</sub> :Sb thermal annealed at 700°C (a) Bright field (b) Dark field	6-14
Figure 6.9 : TEM images of the lower surface region of KrF laser processed SnO <sub>2</sub> :Sb at 60 mJ.cm <sup>-2</sup> , 1000 pulses (a) Dark field (b) Bright field.....	6-15
Figure 6.10 : Complete XPS spectrum of as-deposited SnO <sub>2</sub> :Sb.....	6-17
Figure 6.11 : Complete XPS spectrum of thermal annealed SnO <sub>2</sub> :Sb at 700°C.....	6-18
Figure 6.12 : Complete XPS spectrum of the excimer laser processed SnO <sub>2</sub> :Sb.....	6-18
Figure 6.13 : Complete XPS spectrum of the combined processed SnO <sub>2</sub> :Sb .....	6-19
Figure 6.14 : Mobility vs. carrier concentration for SnO <sub>2</sub> :Sb films: experimental values for thermal annealed, laser processed and as-deposited films, and theoretical mobility due to ionized impurity scattering- $\mu$ is (dashed line).....	6-22
Figure 7.1 : Structure of typical AC powder EL device [126].....	7-3
Figure 7.2 : Schematic energy band diagram of AC powder EL devices. Reproduced from [127] .....	7-4
Figure 7.3 : Dimensions of the excimer laser processed transparent electrode for ACEL devices .....	7-7
Figure 7.4 : Luminescence as a function of applied RMS voltage for ACEL devices fabricated with SnO <sub>2</sub> :Sb as transparent electrode drive at (a) 400 Hz (b) 800 Hz .....	7-9
Figure 7.5 : ACEL device fabricated with spin coated & combined processed SnO <sub>2</sub> :Sb front electrode...	7-10

## List of Tables

<i>Table 2.1: Summary of SnO<sub>2</sub> deposition techniques and their electro –optical properties .....</i>	<i>2-14</i>
<i>Table 2.2: Summarized electrical properties of SnO<sub>2</sub>:Sb with respect to deposition techniques.....</i>	<i>2-15</i>
<i>Table 4.1: Summary of the Dip coated SnO<sub>2</sub>:Sb samples from K&amp;W Ltd and PEL. ....</i>	<i>4-2</i>
<i>Table 4.2: Crystalline size (nm) of SnO<sub>2</sub>:Sb calculated using Scherrer equation.....</i>	<i>4-8</i>
<i>Table 4.3: Summary of the inkjet printed SnO<sub>2</sub>:Sb samples. ....</i>	<i>4-11</i>
<i>Table 5.1 : Summary of XRD findings- As deposited spin coated SnO<sub>2</sub>:Sb.....</i>	<i>5-8</i>
<i>Table 5.2: Summary of XRD findings: Spin coated SnO<sub>2</sub>:Sb –Thermal annealed at 100°C ,200°C ,400°C &amp; 700°C .....</i>	<i>5-13</i>
<i>Table 5.3 : Summary of XRD findings: Spin coated SnO<sub>2</sub>:Sb –KrF laser processed at 60 J.cm<sup>-2</sup> with 1,10,100 and 1000 pulses .....</i>	<i>5-19</i>
<i>Table 5.4 : Summary of the samples used for different thickness thermal annealing of SnO<sub>2</sub>:Sb.....</i>	<i>5-21</i>
<i>Table 5.5: Sheet resistance (KΩ/sq) of thermal annealed SnO<sub>2</sub>:Sb films with respect to annealing temperature and the film thickness . ....</i>	<i>5-22</i>
<i>Table 5.6: Variation of combined processed and thermal annealed sheet resistances (kΩ/sq) of SnO<sub>2</sub>:Sb layers with respect to the thermal annealing temperature and film thicknesses. ....</i>	<i>5-23</i>
<i>Table 6.1: Summary of the spin coated SnO<sub>2</sub>:Sb films used for Hall Effect measurement. The sheet resistance was measured using four point probes. ....</i>	<i>6-3</i>
<i>Table 6.2: Cell parameters of as-deposited and post processed SnO<sub>2</sub>:Sb.....</i>	<i>6-11</i>
<i>Table 6.3: d-spacing corresponds to standard SnO<sub>2</sub> lattice (PDF file No: 21-1250) and measured from TEM analysis .....</i>	<i>6-13</i>
<i>Table 6.4: Sample details of the XPS analysed spin coated SnO<sub>2</sub> :Sb .....</i>	<i>6-17</i>
<i>Table 6.5: Sample details of the XPS analysed spin coated SnO<sub>2</sub>:Sb . The relative peak area is defined as a ratio of [Sb<sup>3+</sup>] in each sample area and [Sb<sup>3+</sup>] found in as- deposited sample. ....</i>	<i>6-19</i>
<i>Table 6.6: Estimated carrier mobility and mean free path of spin coated SnO<sub>2</sub>:Sb.....</i>	<i>6-22</i>
<i>Table 7.1: Post annealing conditions of ACEL transparent electrode.....</i>	<i>7-6</i>
<i>Table 7.2: Sheet resistance and optical transmission variation of spin coated and functionalised SnO<sub>2</sub>:Sb layers.....</i>	<i>7-7</i>

## Abbreviations and Symbols

AC	Alternating Current
ACEL	Alternating Current Electroluminescent Displays
ATO	Antimony doped Tin Oxide
AZO	Aluminium doped Zin Oxide
CCD	Charge Coupled Device
CIJ	Continuous inkjet printing
CNT	Carbon nanotubes
CTA	Classical thermal annealing
CVD	Chemical Vapour Deposition
DC	Direct current
DOD	Drop on demand inkjet printing
ECSA	Electron Spectroscopy for chemical Analysis
FIB	Focus Ion Beam
FLA	Flash lamp annealing
GTP	Global Tungsten and Powders
HiTUS	High Target Utilisation Sputtering
IR	Infrared
ITO	Indium Tin Oxide
IZTO	Indium Zinc Tin Oxide
K&W	Keeling & Walker Ltd
LA	Laser processing
MBE	vacuum based techniques
NTU	Nottingham Trent University
PEL	Printed Electronics Limited
PET	Polyethylene terephthalate
PLD	Pulsed Laser Deposition
PSI	Phase - shifting Interferometry
PVD	Physical Vapour Deposition
RF	Radio frequency
RTA	Rapid Thermal Annealing
SEM	Scanning Electron Microscopy
TA	Thermal annealing
TCO	Transparent Conducting Oxides
TEM	Transmission Electron Microscopy
VSI	Vertical –Scanning interferometry
XPS	X-ray photoelectron spectrometry
XRD	X-ray diffraction

## Variables

$\alpha$	Optical absorption coefficient
$\hbar$	Planck's constant
$E_{bg}$	Band gap Energy
$\beta$	Full width at half maximum height
$\tau$	Carrier relaxation time
$2\theta$	Diffraction angle
$B_x$	Applied magnetic field
$D$	Particle Diameter
$E_F$	Fermi Energy
$I$	Current
$KE$	Kinetic energy
$L$	Luminance
$n$	Bulk charge carrier density
$q$	Elementary charge
$R$	Resistance
$R_H$	Hall coefficient
$T$	Transmission
$T_g$	Transition temperature
$U_o$	Withdrawal speed
$V_H$	Hall voltage
$\eta$	Solution viscosity
$\lambda$	Wavelength
$\lambda_{bg}$	Band gap wavelength
$\lambda_p$	Plasma wavelength
$\rho$	Solution density
$\sigma$	Solution surface tension
$N$	Carrier concentration
$\mu$	Carrier mobility
$\rho$	Electrical resistivity
$l^1$	Grain size
$\epsilon_\infty$	High frequency dielectric constant
$\epsilon_0$	Permittivity of free space
$\phi_b$	Potential barrier height
$\phi$	Spectrometer work function

# 1. Introduction

## 1.1 Overview

Printed electronics (particularly related to plastic electronics) is a rapidly growing technology in electronic manufacturing which deposits electronic layers of organic or inorganic materials, typically in solution-based format onto substrates using direct writing, or printing techniques. This technology is capable of producing lightweight and robust electronics at low cost on large area, flexible substrates. Some applications which will benefit from the printed electronics technology and are likely to be main contenders in future flexible electronics market include: sensors, electronics papers, photovoltaic cells, and hybrid organic/inorganic displays [1, 2]

Direct write technologies are designed to create features in a sequential, additive manner with defined architecture and composition via a process of depositing or dispensing only where needed [3]. As the industry moves towards finer feature sizes, well established and low cost screen printing and stencil printing techniques [4, 5] face difficulty in achieving the resolution required, because of rough edges and higher optical transmission losses due to the rough surface finish. The traditional thin film deposition technique of vapour deposition followed by lithographic patterning can achieve feature resolution down to nanometres (nm) range, but is not suitable for low cost, disposable microelectronic applications [6-8]. Hence, with the capability of producing features from micro to nanoscale size, and the promise of robust manufacturing onto conformal surfaces without use of masks and at low temperatures, direct write techniques such as inkjet printing fill the niche of traditional low cost thin film deposition solutions.

Inkjet printing is a non-impact dot matrix printing technology where streams of drops are ejected onto a media to render an image [9, 10]. Much of recent interest in printed electronics concerns the use of conductive inks. Several materials have been studied,

including molten metal, conductive polymer and metallic nanoparticle suspensions. Due to the possibility of printing at room temperature and overall better performance and conductivity, metallic nanoparticle suspensions have attracted significant interest as potential conductive inks [11-15].

However, an important issue is that the creation of material structures with defined functional properties on a substrate typically includes two stages, (i) material deposition and (ii) material post processing. Post processing is used to realize functional layers and may involve sintering, chemical decomposition, annealing or novel methods such as photonic curing. The selection of post deposition technique is dependent on the material, the substrate used, and the required electrical and optical properties.

Due to the thermodynamic size effect [15], nanoparticle based materials can be potentially deposited and sintered onto low temperature substrates, but the requirement for thermal post deposition processing still presents technical challenges to achieve an overall low temperature method of production. Hence, the use of an alternative – approach, such as via optical irradiation treatments, is of interest as a localised technique that can have minimal thermal effect on substrates and underlying layers. Such low temperature processing is of great interest as a manufacturing tool, and there is consequently a major interest in understanding how to apply the most effective post processing technique as a vital step towards manufacturing low cost microelectronics devices on flexible substrates [16, 17].

## **1.2 Aims and Objectives**

The aim of the research presented here is to investigate the use of a laser processing technique as a potential post processing method to functionalise solution processed nanoparticulate layers suitable for electronic applications. Specifically, in collaboration with industrial partners through a Technology Strategy Board funded project, this work investigates the effect of laser processing of inkjet printed, spin coated and dip coated

thin films of SnO<sub>2</sub>:Sb (ATO) nanoparticles for the realisation of functional nano-layers. The research is based on an experimental study to examine the physical processes involved, with a specific application target of use in electroluminescent displays.

### **1.2.1. Objectives**

- Undertake a review of laser processing application to optimising the performance of inorganic layers
- Examine the effect of thermal annealing, laser processing and combined processing (thermal annealing and laser processing) for dip coated, inkjet printed and spin coated SnO<sub>2</sub>:Sb thin films on electrical and optical properties.
- Undertake electrical, optical and structural characterisation of ATO thin films.
- Liaise with the project collaborators to fabricate a low temperature processed Electroluminescent display with a printed SnO<sub>2</sub>:Sb layer as the front electrode.

## **1.2 Research collaboration**

This research was performed as part of a Technology Strategy Board funded collaborative Research Programme - FAB3D. The partnership consists of two universities: Brunel University and Nottingham Trent University (NTU), and five companies: Printed Electronics Ltd, Keeling & Walker Ltd, Oxley Development Ltd, Johnson Matthey Ltd, and Intrinsic Materials Ltd. The “Centre for Phosphors and Display materials”, at Brunel University is a leader in research relating to the development of luminescent materials, specialising in displays and lighting industrial sectors, providing the novel light emitting nanoparticles and expertise to the FAB3D project. Keeling & Walker are the world leading producer and exporter of Tin Oxide and produced the transparent conductive oxide materials and the SnO<sub>2</sub>:Sb ink for this research work. Johnson Matthey Ltd and Intrinsic Materials provided additional conductive nanoparticulate materials for the FAB3D project. Printed Electronics Limited (PEL) was the Fab3D project coordinator and is a UK Company focussed on the development of process and systems for the commercial fabrication of electronic

circuits, structures and devices using inkjet methods. Hence, the Inkjet printing process that is used to evaluate the results of this research programme was developed by PEL, and was made available to NTU for this research project.

Nottingham Trent University was responsible, through the research presented here, for undertaking the laser processing of solution processed layers and performing characterization of the materials to develop new techniques for the realisation of functional layers. This work has built on excimer laser processing techniques previously investigated by the group at NTU [18], and utilised the specialist laser processing facilities available at the Clifton site.

Throughout this work the following characterisation facilities utilized. Via collaboration, the X-ray Photoelectron spectrometry (XPS) was conducted at Brunel University. The Hall Effect measurements were carried out at Oxford University and the University of Warwick. Also the Transmission Electron Microscopy (TEM) was conducted at the Sonsam Ltd, Glebe Laboratories, Ireland.

## **1.4 Structure of the thesis**

This thesis consists of eight chapters, with Chapter 1 providing an overview of the thesis, including research collaborations, objectives of this study and the thesis structure.

Chapter 2 discusses the background knowledge required for this work. This includes a review of transparent conducting oxides (TCO) - the electrical and optical properties, deposition techniques and applications.

The experimental techniques and the various systems used to undertake this work are detailed in Chapter 3. This includes the inkjet printing system used at PEL, and the excimer laser processing system and electrical and optical characterisation techniques used at NTU throughout this project work.

Chapter 4 presents the results of the study of processing solution based depositions via the dip coating and inkjet printing of SnO<sub>2</sub>:Sb onto glass and flexible photo paper substrates. This contains results relating to excimer laser processing and electrical, optical and structural characterisation of dip coated SnO<sub>2</sub>:Sb films and the results of inkjet printed SnO<sub>2</sub>:Sb films pre and post excimer laser processing along with some issues identified during inkjet printing of SnO<sub>2</sub>:Sb.

The experimental results relating to the spin coating of SnO<sub>2</sub>:Sb are discussed in the Chapter 5 chapter. The first part of the chapter focusses on the results of as-deposited films of SnO<sub>2</sub>:Sb films at different thicknesses. The second half contains the results of excimer laser processing, thermal annealing and combined processing of spin coated SnO<sub>2</sub>:Sb films and their electrical, optical and structural characterisation pre and post processing.

Chapter 6 discusses the electrical, optical and structural characteristics of spin coated SnO<sub>2</sub>:Sb, including analysis of Hall effect measurements, X-ray photoelectron spectrometry (XPS) and Transmission Electron Microscopy (TEM) characterisation. This underpins a discussion on the conduction mechanism of the excimer laser processed SnO<sub>2</sub>:Sb.

Chapter 7 presents the application of the research to the fabrication of alternating current electroluminescent displays (ACEL). Test ACEL devices were fabricated by using the optimum processed SnO<sub>2</sub>:Sb films as front electrodes. Chapter 7 therefore presents the background of electroluminescent displays, and the fabrication details.

Finally, Chapter 8 provides a summary of the key findings of this work and suggests some potential future works relating to this project.

During the FAB3D project, the author has also undertaken excimer laser processing of other solution processed materials such as Y<sub>2</sub>O<sub>3</sub>:Eu to use as an EL layer in ACTFEL devices. This additional work is summarised in Appendix 1.

## **2. Background Review & Theory**

### **2.1 Transparent conducting oxides**

#### **2.1.1. Introduction**

Transparent conducting oxides (TCO) are considered as an unusual class of materials due to their unique physical properties: high electrical conductivity and high optical transparency in the visible region of the electromagnetic spectra. This peculiar combination of properties is considered to be mutually limited and only exists if the material has sufficiently large band gap  $> 3$  eV and the presence of free charge carriers - conduction band electrons [19].

The applications utilising TCOs date back to World War II, where they were used as transparent heaters to de-ice aircraft windshields [20] . Presently, TCOs are used in wide variety of applications in the areas of optoelectronic, mechanical, and architectural systems. TCOs are commonly used as transparent electrodes in organic and inorganic display devices [1, 2, 21, 22], solar cells [7, 23], heat mirrors [24], energy efficient windows and gas sensors [25, 26, 1, 273, 12]. (Section 2.6 contains further details about applications of TCOs).

When applied to such a wide range of applications, the TCO materials used require different characteristics. For example, when used in a passive electrical manner as transparent electrodes or transparent hot mirrors, the TCO films must have high conductivity and high transparency in the visible region. But when in an active manner, such as the channel layer in thin film transistors, TCOs should have semiconducting properties, with a lower carrier concentration. This range in characteristics can be addressed by carefully controlling, via co-doping, the electrical conductivity and the optical window of the material. The optical window of the TCOs is shown in figure 2.1.

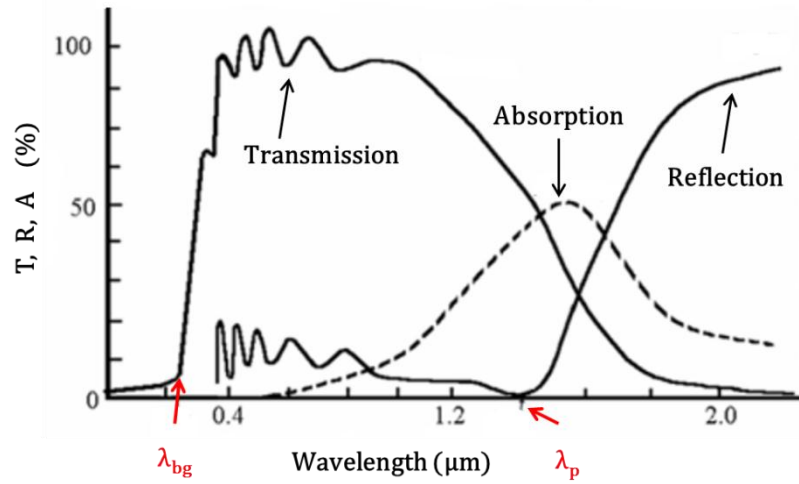


Figure 2.1 : Schematic diagram of the optical window of TCOs [28]  $\lambda_{bg}$  and  $\lambda_p$  are the wavelengths where band gap absorption and free electron absorption takes place

As shown in figure 2.1 the optical window of the TCO is defined by two cut-off wavelengths  $\lambda_{bg}$  and  $\lambda_p$ . The wavelength which separates the absorption zone in the ultra violet (UV) range from the transparent zone in the visible region,  $\lambda_{bg}$ , corresponds to the threshold of inter-band absorptions and correlates to the optical band gap of the material,  $E_{bg}$ , by

$$E_{bg} = \frac{\hbar c}{\lambda_{bg}} \geq 3 \text{ eV} \quad \text{Eq 2.1}$$

Where,

$\hbar$  = Planck's constant ( $\hbar = 6.63 \times 10^{-34}$  J.s) and

$c$  = Velocity of the light ( $c = 2.99 \times 10^8$  ms<sup>-1</sup>)

In the electromagnetic spectra, visible light is falling in the range of 400 nm to 700 nm which corresponds to the energy range of 3.1 eV to 1.8 eV. Therefore for a TCO to be transparent in the visible region, their direct band gap has to be  $\geq 3$  eV.

The wavelength which corresponds to the front rise of the reflectivity in the infrared (IR) region,  $\lambda_p$ , is generally known as the plasma wavelength and corresponds to intra-

band absorption in the conduction band of the electrode material. The plasma wavelength,  $\lambda_p$  can be expressed as,

$$\lambda_p = \left( \frac{\epsilon_0 \epsilon_\infty \tau}{N e \mu} \right)^{1/2} \quad \text{Eq 2.2}$$

Where N is the carrier concentration in the conduction band,  $\mu$  is the carrier mobility,  $\tau$  is the carrier relaxation time and  $\epsilon_0$  and  $\epsilon_\infty$  represent the permittivity of free space and high frequency dielectric constant of the involved media respectively.

The conductivity type and the free carrier concentration of the TCO can be varied by adding intentional impurities to the host material – known as doping. The n-type doping occurs as a result of the incorporation of dopant atoms in a bonding configuration that does not use all the valence electrons, while p-type occurs due to additional valence electrons taken (accepted) from the host lattice. Dopant incorporated into a lattice mainly occupies substitutional lattice sites [29]. In TCOs, the lattice site can be either a cation or an anion site. Which of the two sites is preferred by a dopant depends on many factors, including the valence electron correlation between dopant and host, the bond strength between the dopant atom and the surrounding host lattice, and the ionic size of the dopant.

The first ever TCO semiconducting film goes as far as back to 1907, where Bideker first reported work on cadmium oxide (CdO) films by thermal oxidation of sputtered cadmium. From that point onwards there has been tremendous interest in TCOs with the advancement of optoelectronic technology [30]. Over the past decades, a large class of n-type conducting TCOs have been reported and they are based on either:

- Non-stoichiometric binary compounds:  $\text{In}_2\text{O}_{3-x}$ ,  $\text{Zn}_{1+x}\text{O}$ ,  $\text{SnO}_{2-x}$
- Doped binary compounds :  $\text{In}_{2-x}\text{Sn}_x\text{O}_3$  (ITO),  $\text{SnO}_{2-x}\text{F}$  (FTO),  $\text{Sn}_{2-x}\text{Sb}_x\text{O}_2$  (ATO),  $\text{Zn}_{1-x}\text{Al}_x\text{O}$  (AZO) and
- Non-stoichiometric ternary compounds:  $\text{Cd}_2\text{SnO}_{4-x}$ ,  $\text{Zn}_2\text{SnO}_{4-x}$ ,  $\text{Zn}_2\text{In}_2\text{O}_{5-x}$ ,  $\text{ZnSnO}_{3-x}$

Where  $x$  denotes the deviation of the compound from stoichiometry, by oxygen vacancies or interstitial cation or by the addition of dopants.

In addition to these n-type TCOs, continuous effort is been made to find p-type conducting TCOs [31], but the electron–acceptor states responsible for the p-type conductivity have not been clearly identified.

The most commonly used transparent conductors are Indium Oxide ( $\text{In}_2\text{O}_3$ : band gap = 3.75 eV), Tin Oxide ( $\text{SnO}_2$ : band gap = 3.6 eV) , Zinc oxide ( $\text{ZnO}$ : band gap = 3.35 eV) and Cadmium stannate ( $\text{Cd}_2\text{SnO}_4$ ). Among them Sn doped Indium oxide ( $\text{In}_2\text{O}_3\text{:Sn}$ ), commonly known as ITO is the most widely used in industry. For this research work antimony doped tin oxide ( $\text{SnO}_2\text{:Sb}$ ) is considered as the material of interest and details are discussed later in this chapter under section 2.3.

### **2.1.2. Electron band structure of TCOs**

As shown in figure 2.2 (a) the TCO host is an insulator with a band gap of  $E_g$  and a dispersed parabolic conduction band which originates from interaction between metal  $s$  and oxygen  $p$  states. Typically, the conventional TCO hosts are oxides of the post transition metals with  $(n-1)d^{10} ns^2$  electronic configuration and have densely packed structures with four or six metal ions.

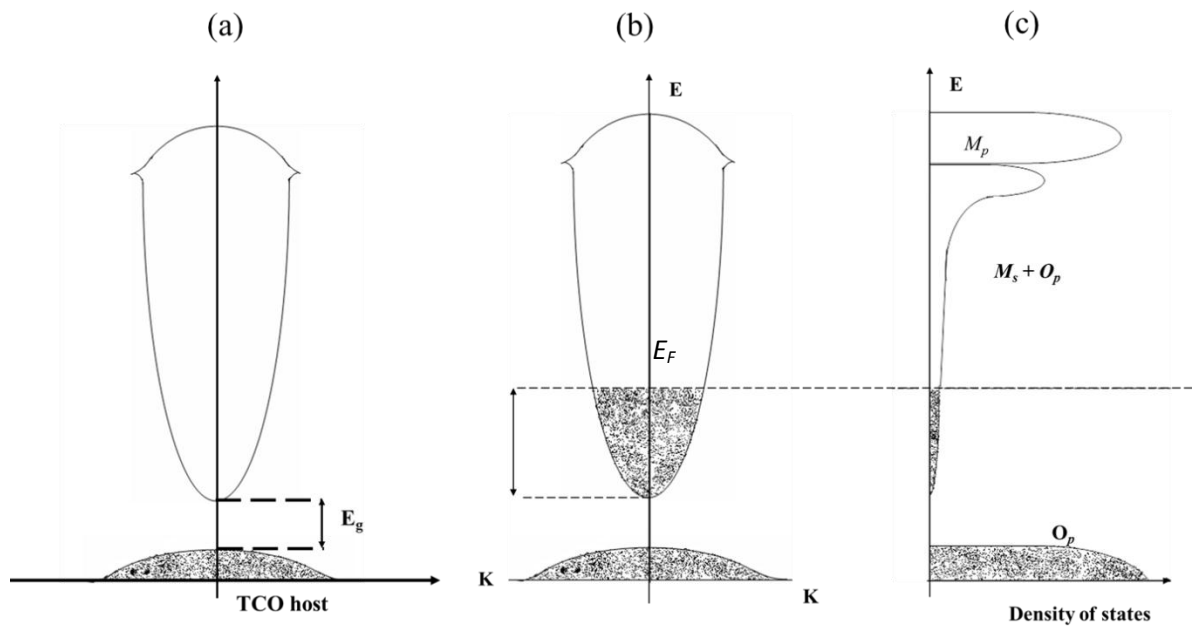


Figure 2.2 : Electron band structure of (a) TCO host (b) Degeneracy doped TCO (c) density of states of degeneracy doped TCO [32]

Figure 2.2 (b) and (c) shows the degenerate doping of the host material and the doping generates electron-donor energy states in the Metal  $s$  and Oxygen  $p$  character. These electron-donor centers are spontaneously ionized and liberate high mobility extra carriers due to small effective mass and also low optical absorption due to low density of states in the conduction band. This high energy concentration of electrons in the conduction band ensures a prominent Fermi level ( $E_F$ ) displacement up above the conduction band minimum level. This is known as Burstein-Moss shift. This shift helps to broaden the optical transparency window and also making the material conducting.

### 2.1.3. Optical properties of TCOs

The optical properties are a powerful tool to study the material band gap, localized defects and impurity levels. Therefore these properties are strongly dependent upon the material deposition technique, growth parameters and microstructure. The typical transmission spectrum of a TCO is shown in figure 2.3. In this UV-visible spectrum two

regions can be identified as (a) strong absorption region and (b) interference transmission region. In the strong absorption region, the fundamental absorption which corresponds to electron excitation from the valence band to the conduction band can be used to determine the nature and value of the optical band gap.

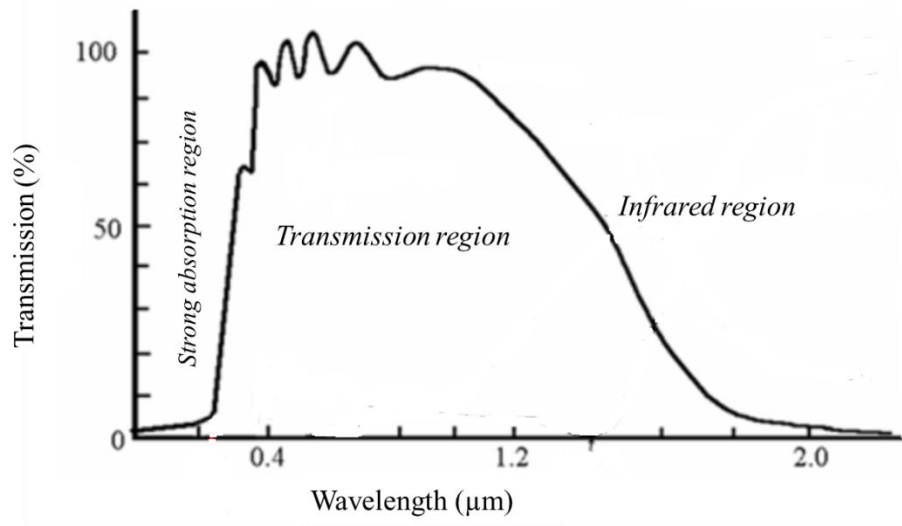


Figure 2.3 : Transmission spectrum of TCO thin films [28]

### 2.1.3.1 Strong absorption region

The transmission  $T$ , of a TCO can be expressed as;

$$T = \exp(-\alpha t) \quad \text{Eq 2.3}$$

Therefore for a known thickness,  $t$ , the absorption coefficient,  $\alpha$  can be calculated by using the transmission spectra  $T$  as,

$$\alpha = -\ln(T)/t \quad \text{Eq 2.4}$$

Hence the extinction coefficient,  $k$  can be evaluated as,

$$k = \alpha\lambda/4\pi \quad \text{Eq 2.5}$$

The absorption coefficient,  $\alpha$  is related to the incident photon energy  $h\nu$  as,

$$\alpha = \frac{K (h\nu - E_g)^{n/2}}{h\nu} \quad \text{Eq 2.6}$$

Where  $K$  is a constant and a function of refractive index, reduced mass and speed of light.  $E_g$  is the optical band gap and the value of  $n$  is equal to 1 for direct band gap materials such as SnO<sub>2</sub>.

By using the above Equation 2.6, the direct band gap of the material can be evaluated by plotting  $(\alpha h\nu)^2$  as a function of incident radiation  $h\nu$  and then extrapolating the straight linear part of the curve and intercept with energy axis [33] (figure 2.4). For the indirect allowed transitions, the band gap can be determined by extrapolating the straight linear part of the  $(\alpha h\nu)^{1/2}$  vs  $h\nu$  curve to the zero [34].

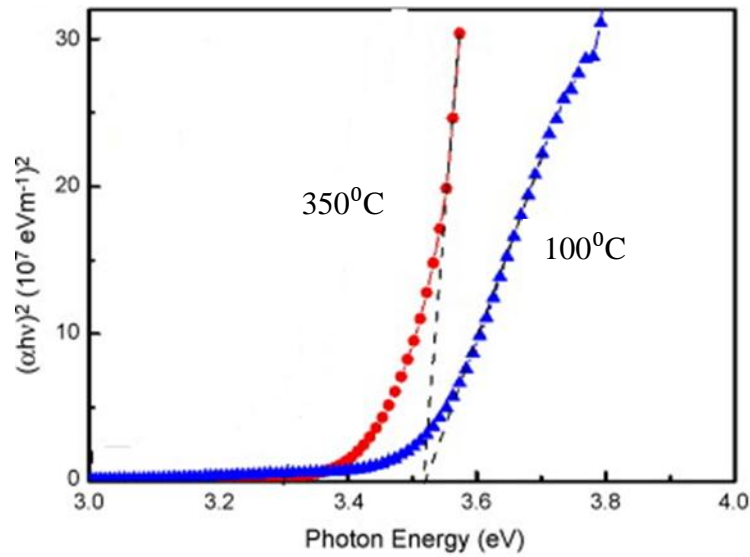


Figure 2.4 :  $(\alpha h\nu)^2$  dependence on the photon energy of TCO grown at different temperatures [35]

### 2.1.3.2 Infrared region

In this region the optical phenomenon can be explained by using Drude's theory for free electrons in metals. According to the Drude's theory, the relative permittivity  $\epsilon$ , can be expressed as;

$$\epsilon = (n - ik)^2 = \epsilon_1 + i\epsilon_2 \quad \text{Eq 2.7}$$

Where,

$$\epsilon_1 = (n^2 - k^2) = \epsilon_\infty \left( 1 - \frac{\omega_p^2}{\omega^2 + \gamma^2} \right) \quad \text{Eq 2.8}$$

And

$$\epsilon_2 = 2nk = \epsilon_\infty \left[ \frac{\omega_p^2 \gamma}{\omega(\omega^2 + \gamma^2)} \right] \quad \text{Eq 2.9}$$

The plasma resonance frequency  $\omega_p$  is given by;

$$\omega_p = \left( \frac{Ne^2}{\epsilon_0 \epsilon_\infty m_e^*} \right)^{1/2} = \frac{2\pi c}{\lambda_p} \quad \text{Eq 2.10}$$

The  $\epsilon_0$  and  $\epsilon_\infty$  represents the free space and high frequency dielectric constants respectively. The effective mass of the charge carriers are denoted by  $m_e^*$ .  $N$  and  $\lambda_p$  represents the carrier concentration and the plasma wavelength respectively.

The  $\gamma$  is equivalent to  $1/\tau$ , and is related to the mobility ( $\mu$ ) as;

$$\gamma = \frac{1}{\tau} = \frac{e}{m_e^* \mu} \quad \text{Eq 2.11}$$

Where  $\tau$  is the relaxation time.

For the free carriers, three different frequency regions can be identified as;

1. Absorbing region :  $0 < \omega \ll 1/\tau$
2. Reflecting region :  $1/\tau < \omega < \omega_p$  and
3. Transparent region :  $\omega > \omega_p$

In the absorbing region, the imaginary part of the relative permittivity,  $\epsilon_2$  is much higher than the real part  $\epsilon_1$  and the films are strongly reflecting. In the reflection region the absorption constant falls rapidly and the real part of relative permittivity,  $\epsilon_1$ , becomes negative. Therefore the reflectivity can be given as;

$$R = 1 - \frac{2}{\omega_p \tau \epsilon_\infty^{1/2}} \quad \text{Eq 2.12}$$

In the transparent region the real part of relative permittivity,  $\epsilon_1$  becomes positive and therefore the reflection power becomes minimum and the films are transparent.

The carrier concentration,  $N$  has a two fold effects and firstly it models the plasma wavelength and secondly it influences the subsequent reflection gradient according to Eq 2.12. As explained in Eq 2.10, for higher the carrier concentrations the plasma absorption wavelength shifts towards the visible region and results in a lower value.

Correlating the electrical and optical data of TCOs, one can estimate the electron density and mobility values from the optical data. Also for known values of  $n$  and  $k$  from optical data in the plasma resonance region and the  $N$  and  $\mu$  from electrical data, the value of effective mass of charge carriers can be calculated by using the Eq 2.9 to Eq 2.11.

#### 2.1.4. Electrical conduction of TCOs

The electrical properties of the TCOs are strongly dependent on the deposition technique used, doping concentration, substrate temperature, annealing technique and other growth parameters [36]. (The basic theory relating to the transport phenomena in

semiconductor thin films is discussed later in chapter 3 relating to sheet resistance and Hall Effect measurements and only the conduction phenomena is discussed here).

The change of the electrical resistivity may be attributed mainly due to three different contributions: microstructural defects, increase of the degree of crystallinity, and the scattering of charge carriers by the film surface [37]. Several scattering mechanisms are identified in TCOs, such as ionized impurity scattering, neutral centre scattering, grain boundary scattering and scatterings due to structural defects (vacancies, dislocations, stacking faults). Other than that, in degenerately doped semiconductors, non-parabolicity of the conduction band and formation of impurity clusters also contribute to the scattering process [38].

#### 2.1.4.1 Grain boundary scattering

Grain boundary scattering is present in polycrystalline semiconductors with the conduction mechanism dominated by inter-crystalline boundaries. The grain barriers generally contain high densities of interface states which are charged by carriers from the grains. The charge balance creates a depletion region on both sides of a grain barrier and, due to this effect; band bending occurs and causes a potential barrier to charge transport as shown in figure 2.5(a) [39]. According to the model by Petritz [40] the conductivity of charge carriers dominated by grain boundary can be expressed as;

$$\sigma_g = eN\mu_0 \exp\left(\frac{-e\phi_b}{kT}\right) \quad \text{Eq 2.13}$$

Where,  $\phi_b$  is the potential barrier height and N is the carrier concentration. The  $\mu_0 = (M/n_c k_B T)$ ,  $n_c$  is the number of crystallites per unit length along the film and M is a factor that depends on the barrier.

By using eq 2.8, the general grain boundary limited mobility can be expressed as [28];

$$\mu_g = e l' \{8/(\pi\beta^2 k T m^*)\}^{1/2} \exp\left(\frac{-e\phi_b}{kT}\right) \quad \text{Eq 2.14}$$

Where,  $l'$  is the grain size.

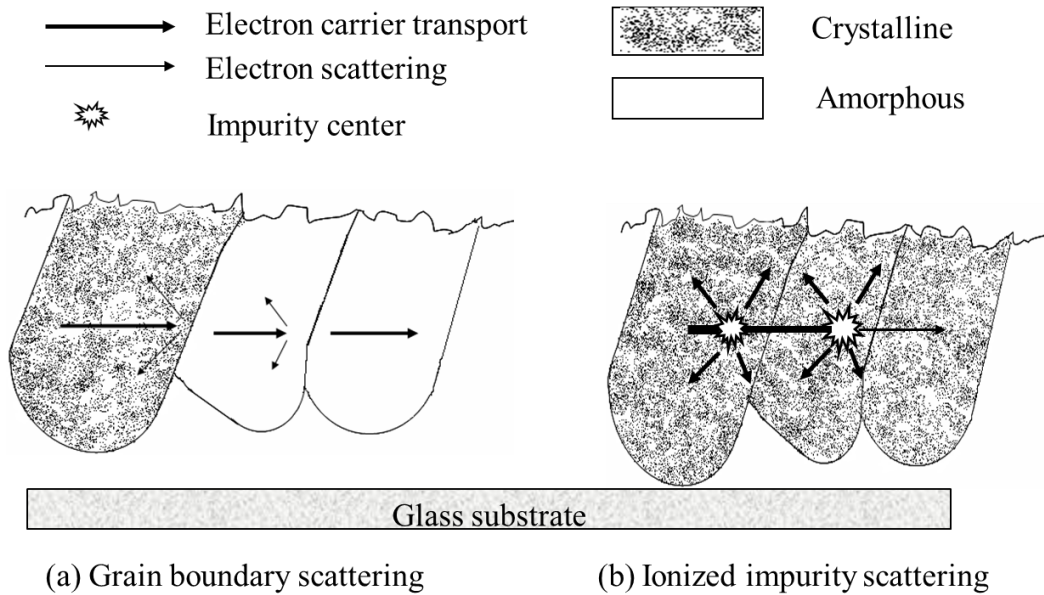


Figure 2.5 : The sketch of (a) grain boundary scattering with low degree of crystallinity (b) Ionized impurity scattering in TCO [38]

#### 2.1.4.2 Ionized impurity scattering

In degenerate TCOs, scattering due to ionized impurities are the major mechanism limiting the carrier mobility. Figure 2.4(b) shows an imaginary sketch for ionized impurity scattering [39] with high carrier concentration. The contribution due to ionized impurity scattering can be expressed as;

$$\mu_{IS} = \frac{4e}{h} \left(\frac{\pi}{3}\right)^{1/3} N^{-2/3} \quad \text{Eq 2.15}$$

#### 2.1.4.3 Neutral impurity scattering

Scattering due to neutral impurities at room temperature in a crystal lattice is similar to the scattering of low energy electrons in a gas. The mobility due to neutral impurity scattering can be expressed as;

$$\mu_n = \frac{m^* e^3}{20 \epsilon \epsilon_0 \hbar^3 N_n} \quad \text{Eq 2.16}$$

Where  $N_n$  is the concentration of neutral impurities.

## 2.2 Tin oxide

### 2.2.1. Structure of SnO<sub>2</sub>

SnO<sub>2</sub> is an n-type, wide band gap semiconductor with a band gap of ~ 3.6 eV and in the form of thin films it has attractive electrical and optical properties as a TCO [41].

SnO<sub>2</sub> has a Tetragonal rutile structure at ambient temperature and pressure [42]. The unit cell contains six atoms- two tin and four oxygen. The tin cations are located at (0,0,0) and (  $\frac{1}{2}$ ,  $\frac{1}{2}$ ,  $\frac{1}{2}$  ) positions in the unit cell, and the oxygen anions at  $\pm(u,u,0)$  and  $\pm(\frac{1}{2}+u, \frac{1}{2}-u, \frac{1}{2})$  positions where the internal parameter  $u = 0.307$ . As shown in figure 2.6, the tin atom in the unit cell is surrounded by six oxygen atoms placed approximately at the corners of a regular octahedron. Each oxygen atom is surrounded by three tin atoms approximately at the corners of an equilateral triangle. The lattice parameters are  $a = b = 4.737\text{\AA}$  and  $c = 3.185\text{\AA}$ .

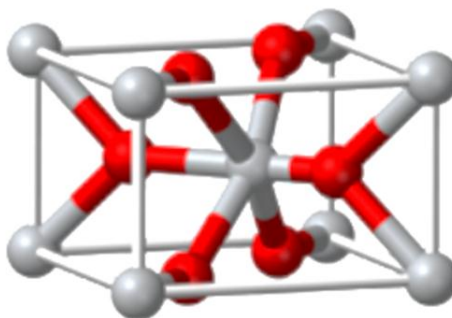
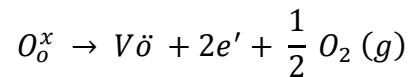


Figure 2.6 : Crystal structure of SnO<sub>2</sub> [36]. Tin atoms show in grey colour and the oxygen atoms in red.

SnO<sub>2</sub> is a wide band gap semiconductor and therefore in the stoichiometric form it has to be an insulator or at most an ionic conductor. However, in practical films, the material is typically electrically conducting. The electrical conduction of SnO<sub>2</sub> results from the defects in the crystal due to either oxygen vacancies or interstitial tin atoms or other intentionally added impurities. The electron generation due to oxygen vacancies can be described by Kroger-Vink notation as:



According to the above equation, the oxygen anions escaping the crystal structure ( $\frac{1}{2} O_2$ ) from an occupied oxygen site creates a double ionized vacancy site ( $V\ddot{o}$ ) and two free electron carriers. Due to minimisation of carrier scattering on crystal impurities this sort of multiple carrier creations from single defects are highly desired [43].

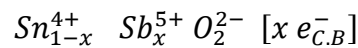
In SnO<sub>2</sub>, the cation has two valence states +2 and +4, with replacement of higher valance 4+ states by an impurity in the oxide increasing the n-type conductivity while replacement of lower valency cation produces a hole which acts as a trap in p-type semiconductors and decreases the conductivity. In the case of SnO<sub>2</sub>, Antimony (Sb) and Fluorine (F) are used as cation dopant and anion dopants respectively. Although these dopants generally increase the conductivity, the electrical and optical properties of these materials are highly dependent on the deposition and processing techniques used. Table 2.1 summarises some of the deposition techniques used to produce SnO<sub>2</sub> thin films and their key electrical and optical properties.

Deposition technique	Resistivity $\Omega.cm$	Optical Transmission (%)	Hall mobility ( $cm^2 V^{-1} s^{-1}$ )	Carrier concentration ( $cm^{-3}$ )	Reference
Dip coating	$5.4 \times 10^{-3}$	90	0.90	$2 \times 10^{19}$	[44]
Ion beam sputtering	$1.3 \times 10^{-2}$	75	-	$1.3 \times 10^{20}$	[45]
Metal organic deposition (MOD)	$6.19 \times 10^{-1}$	-	2.75	$3 \times 10^{18}$	[46]
Spray pyrolysis	$6.33 \times 10^{-3}$	75	3.81	$2.59 \times 10^{20}$	[47]
RF magnetron sputtering	$6.1 \times 10^{-3}$	95.2	7.72	$1.33 \times 10^{20}$	[48]

Table 2.1: Summary of SnO<sub>2</sub> deposition techniques and their electro–optical properties

### 2.2.2. Antimony doped Tin Oxide

The electronic n- type conductivity of the SnO<sub>2</sub> can be highly enhanced by doping it with pentavalent cations such as Sb<sup>5+</sup>. Once the cation added the electron- donor centres are spontaneously ionised, and release free electrons n to the conduction band which leads to the metal type conductivity. The presence of the free electrons in the conduction band can be expressed as



SnO<sub>2</sub>:Sb is considered as important member of the TCO family, due to its capability to produce nano scale particles. These nano structural SnO<sub>2</sub>:Sb can be formulated as inks

and show greater sensitivity, specially for gas sensor applications due to the higher surface to volume ratio. Several projects have been carried out to functionalise nanoparticulate SnO<sub>2</sub>:Sb ink for large area low cost microelectronics applications [49-51]. In addition, Leon-Brito et al [52] reported successful electrospinning of SnO<sub>2</sub>:Sb nanofibers for sensor applications. These nanofibres showed monotonically varied resistivity with temperature as 714 Ω.cm at 2 K to 0.1 Ω.cm at 300 K.

The electrical properties of the SnO<sub>2</sub>:Sb films are highly depend on deposition technique, post processing techniques and the doping concentration. Table 2.2 summarizes some of the electrical properties of SnO<sub>2</sub>:Sb with respect to deposition techniques.

Deposition technique	Resistivity Ω.cm	Optical Transmission (%)	Hall mobility (cm <sup>2</sup> V <sup>-1</sup> s <sup>-1</sup> )	Carrier concentration (cm <sup>-3</sup> )	Reference
Inkjet printing	5.9 x 10 <sup>-2</sup>	85	0.1	1 x 10 <sup>21</sup>	[51]
Dip coating	4.0 x 10 <sup>-4</sup>	80	0.29	6 x 10 <sup>19</sup>	[44]
DC magnetron sputtering	3.3 x 10 <sup>-3</sup>	68	6.0	3.25 x 10 <sup>20</sup>	[46]
Spray pyrolysis	1.22 x 10 <sup>-3</sup>	75	9.83	5.19 x 10 <sup>20</sup>	[47]
Ion beam sputtering	8.5 x 10 <sup>-3</sup>	60.0	-	2.7 x 10 <sup>20</sup>	[48]

Table 2.2 : Summarized electrical properties of SnO<sub>2</sub>:Sb with respect to deposition techniques.

### **2.2.3. Antimony doped Tin Oxide vs other TCOs**

Indium Tin Oxide (ITO) is the TCO of choice for many applications, especially as a transparent conductor, because of its two chief properties: high electrical conductivity and high optical transparency, both achievable when ITO is applied in thin films. The existing market for ITO alone, as part of the overall transparent conductor market is worth well over \$4 billion [53] and it is always been a challenge to supply the current demand with this single dominant material. In addition, alternatives to ITO are of interest due to the high cost and availability of indium. Several alternative options exist for TCOs, and among them nanoparticulate materials are always of interest as they have potential for manufacture by solution-processable techniques.  $\text{SnO}_2:\text{Sb}$  is considered as a promising alternative to ITO for various reasons. It shows better thermal and chemical stabilities compared with ZnO based TCOs [54] as well as well lower cost compared to ITO. Also it can be easily produced as a nanomaterial, which leads to use it as a material of choice for low cost large area applications.

### **2.3 TCO deposition techniques**

Typical thin film deposition processes can be divided into two groups as: physical and chemical processes. The physical processes are comprised of physical vapour deposition (PVD), while the chemical processes includes chemical vapour deposition (CVD) and chemical solvent deposition techniques. Figure 2.7 shows the typical deposition processes used to deposit thin films of materials [55].

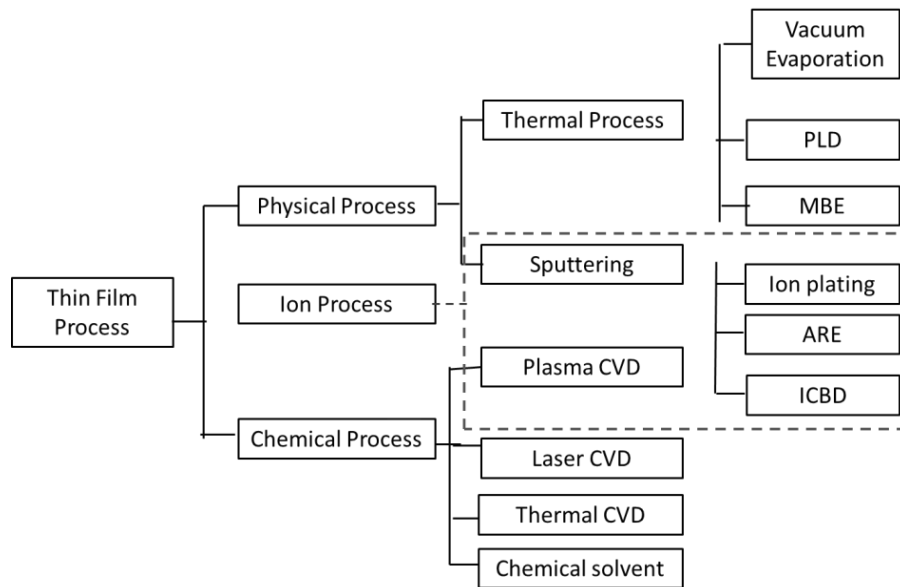


Figure 2.7 : Thin film deposition processes: CVD- Chemical vapour deposition, PLD- pulsed laser deposition, MBE- Molecular beam epitaxy; ARE- Activated reactive evaporation, ICBD- Ionized Cluster Beam Epitaxy

Vacuum evaporation, pulsed laser deposition (PLD) and molecular beam epitaxy (MBE) are vacuum based techniques and are not further discussed in this chapter as they are not feasible for low cost, large area applications, which is the focus of this research.

Ion plating and activated reactive evaporation (ARE) are quite similar vacuum based deposition techniques and in both cases evaporated ions are ionized at the plasma region and accelerated by the electrical field prior to deposition at the substrate. In the ARE reactive gas is injected into the plasma region to achieve the reaction between evaporated atoms and the reactive gas atoms. Although the ion plating technique developed for large area flexible applications, still not feasible for low cost disposable applications.

The chemical vapour deposition (CVD) techniques usually involve very high temperatures ( $\sim 1000^{\circ}\text{C}$ ) and are thus not feasible to use for deposition of materials on flexible substrates and therefore not included to this study. The following sections are therefore concerned with discussion of sputtering techniques, solution based deposition

techniques and inkjet printing as viable TCO deposition techniques for low cost, large area optoelectronic applications.

### **2.3.1. Sputter deposition**

Sputtering is a mature technique to deposit thin films with high purity and homogeneity. This process involves deposition in a vacuum chamber at low gas pressure via the collision of surface atoms in a solid target with energetic atoms such as accelerated particles formed in a plasma discharge. The widely used approach for growing thin films by sputter deposition is the use of a magnetron source in which positive ions present in the plasma of a magnetically enhanced glow discharge bombard the target [56]. Depending on the way the target is powered the sputtering can be achieved in many ways including radio frequency (RF) magnetron sputtering [57], pulsed magnetron sputtering, alternating current (AC) magnetron sputtering and direct current (DC) magnetron sputtering [58]. The DC magnetron sputtering technique is mainly used for conductive targets while the RF magnetron sputtering is used for non-conducting targets. Other than the above mentioned techniques, specialist magnetron sputtering techniques such as high target utilisation sputtering (HiTUS) also used to deposit TCO in lower substrate temperatures by remotely generating plasma in a side chamber opening to the main process chamber [59].

Even though these sputtering techniques deposit high purity and homogeneous TCO films, the associated loss of the target materials during sputtering and expense for the treatment of non-environment friendly wastes limits the use of these techniques for low cost optoelectronic applications [60]. Thus the following sections will discuss inkjet printing and solution based techniques as viable TCO low cost, large area deposition techniques.

### 2.3.2. Dip coating

Dip coating is a low cost solution deposition technique to coat irregular and complex surfaces onto different substrates. In this process the substrate is immersed into a coating bath containing the coating solution. The film is produced by either removing the substrate vertically from the solution or by draining the solution from the reservoir at constant speed. The deposition stage therefore has three key stages: immersion, dwell time, withdrawal, film formation, solvent evaporation and continued drainage of the excess solution. Figure 2.8 shows the film withdrawal stage of the dip coating process.

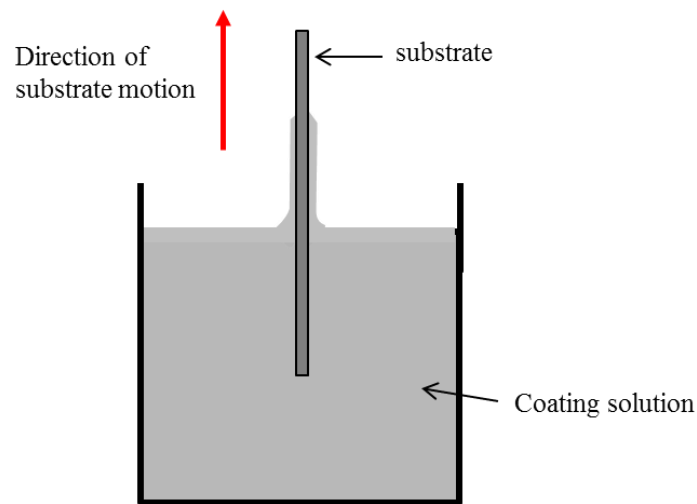


Figure 2.8 : Schematic diagram of dip coating

In this technique different thickness films can be achieved by controlling the properties of the solutions and the parameters of the dip coater - such as withdrawal speed. According to Landau and Levich, the thickness of the film formed is determined by withdrawal speed ( $U_0$ ), solution viscosity ( $\eta$ ), solution density ( $\rho$ ) and solution surface tension ( $\sigma$ ) [61] as follows;

$$h_0 = 0.944 \frac{(\eta U_0)^{2/3}}{\sigma^{1/6} (\rho g)^{1/2}} \quad \text{Eg 2.17}$$

Where  $h_0$  is the limiting film thickness and  $g$  is the acceleration caused by gravity.

As seen in the above equation, for a given solution, the film thickness is directly proportional to two thirds power of the withdrawal speed. Therefore for thicker films the withdrawal speed has to be faster.

The common defects associates with this technique are voids, pin holes, thickness variations and wavy surfaces. By carefully handling the solution, the air entrapment of the film and the surface contamination can be minimised to help reduce these defects. The dip coating technique has been used to deposit SnO<sub>2</sub>:Sb layers in several reports [21, 44, 62, 63]. Among them Hammond et al [44] achieve resistivity of  $5.4 \times 10^{-4} \Omega \cdot \text{cm}$  on dip coated films with transmission of 96% when Sb-doped at 2% at. Also Zhang et al reported transmission values of 80 - 90% of the dip coated SnO<sub>2</sub>:Sb films with the sheet resistance of 85 - 100  $\Omega \cdot \text{cm}^{-2}$ .

### **2.3.3. Spin coating**

Spin coating is a useful technique to deposit materials in liquid form on to flat substrates. This process differs to the dip coating due to centrifugal draining and evaporation stages associated with the deposition. In this technique, a substrate is placed on motor driven vacuum chuck and the coating solution is dispensed onto the substrate. The substrate is then spun at fairly high angular velocities (depending on application) to produce uniform thin films by spinning off the excess liquid from the substrate. The typical angular velocities used to spin coat materials are ~ 300 - 10,000 rpm [64]. Figure 2.9 shows the schematic of typical spin coating technique.

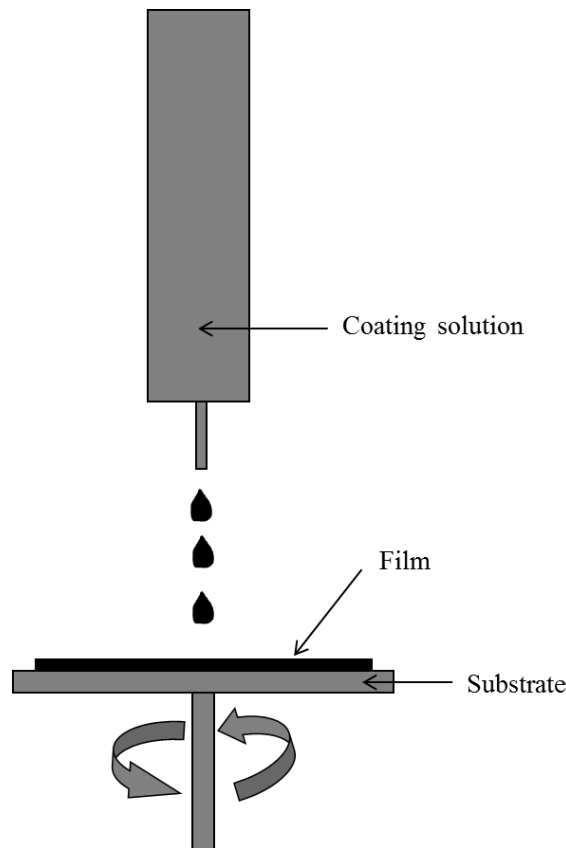


Figure 2.9 : Schematic diagram of the substrate positioning during spin coating

This technique produces uniform thick films due to the fact that the viscosity is not shear dependant and does not vary over the substrate. During the spin off, two forces act in opposite directions are balanced to produce uniform films: The viscous force determined by the viscosity of the ink, which acts inwards and the centrifugal forces created by the rapid spinning, which drives flow outwards [65].

In this technique the film thickness can be varied by controlling the viscosity of the ink, spin speed and the spinning time. For a given ink with constant viscosity and density, the film thickness is proportional to the spinning rate by,

$$h(t) \propto \frac{1}{\sqrt{\omega}} \quad \text{Eq 2.18}$$

Comparing to other deposition techniques, reproducibility, uniformity, low cost, and ability to use for different substrate materials are the key advantages of this technique. But this technique cannot be used to deposit complex structures and the only possibility to deposit on flat surfaces is one of the the main drawbacks of this method.

When spin coating  $\text{SnO}_2\text{:Sb}$ , Dua et al [66] reported resistivity values of  $1.19 \times 10^{-3} \Omega\cdot\text{cm}$  and transmission of around 90% for the films of 30 wt % Sb. Also Goebbert et al [67] reported resistivity values of  $1.7 \times 10^{-2} \Omega\cdot\text{cm}$  and transmission of >90% for 200 nm thickness  $\text{SnO}_2\text{:Sb}$  films sintered at  $550^\circ\text{C}$ .

#### **2.3.4. Spray pyrolysis**

Spray pyrolysis is a widely used solution based process to deposit metal and metal oxide powders and this process can be described as the conversion of micro sized liquid droplets of precursors or a precursor mixture into solid particles. The spray pyrolysis deposition process involves several steps [68],

- Generation of micron sized liquid precursor or precursor mixture
- Evaporation of solvent and condensation of solute
- Decomposition and reaction of solute
- Sintering of solid particles

Several groups have reported spray pyrolysis deposition of  $\text{SnO}_2\text{:Sb}$  and other TCO onto glass substrates. Zhang et al [69] report transmission of 67% in the visible region with carrier concentration of  $7.4 \times 10^{20} \text{cm}^{-3}$  and Hall mobility of  $2.5 \text{cm}^2\text{V}^{-1}\text{s}^{-1}$  for their  $\text{SnO}_2\text{:Sb}$  films, with the Sb concentration of 2.0 wt%. Also, Rajpure et al [70] reported resistivity as low as of  $4 \times 10^{-3} \Omega\cdot\text{cm}$  with average transmission of 80% for their films when thermal annealed at  $520^\circ\text{C}$ . Other than that, for PEDOT:PSS films that were spray deposited by Na et al [7] onto glass substrate for ITO free solar cell applications, the reported properties were a sheet resistance of  $63.3 \Omega/\text{sq}$  and transmission of 89%.

## **2.4 Inkjet printing technology**

The market for inkjet printing has been rapidly growing in recent decades. It is not limited to home or office printing, but for functional inks on different substrates. This is a non-contact printing technology where ink droplets are jetted from an orifice directly to a specific position on the substrate to create an image. The first inkjet device dates back to 1951, where Elmqvist patented as ‘Measuring instrument of the recording type’ [71]. Depending on the way the droplets are generated, inkjet technology can be divided into two distinctive types as: continuous inkjet printing (CIJ) and drop on demand inkjet printing (DOD).

### **2.4.1. Continuous inkjet printing**

In continuous inkjet printing, a stream of uniform size and space droplets are formed at high frequency by forcing a liquid ink under pressure through a nozzle. In CIJ printing, when the drop break off mechanism was controlled, electrostatically charged drops were formed out of the continuous ink stream. In order to place these ink droplets on the required positions, the droplets are then passed through an electric field between deflector plates. When passing through the electrical field between the deflector plates, the charged droplets are guided to the media while the uncharged droplets are collected into a gutter. Depending on the drop deflection technique, the CIJ printers can be divided into two groups: binary deflection systems and multiple deflection systems. In the binary deflection system, the charged droplets are directly flying to the media while the uncharged ones are deflected to the gutter for recirculation. In a multiple deflection system, the charge of each droplet is varied to accurately position the droplets onto the media. Figure 2.10 shows the droplet formation and deposition in a continuous inkjet printer.

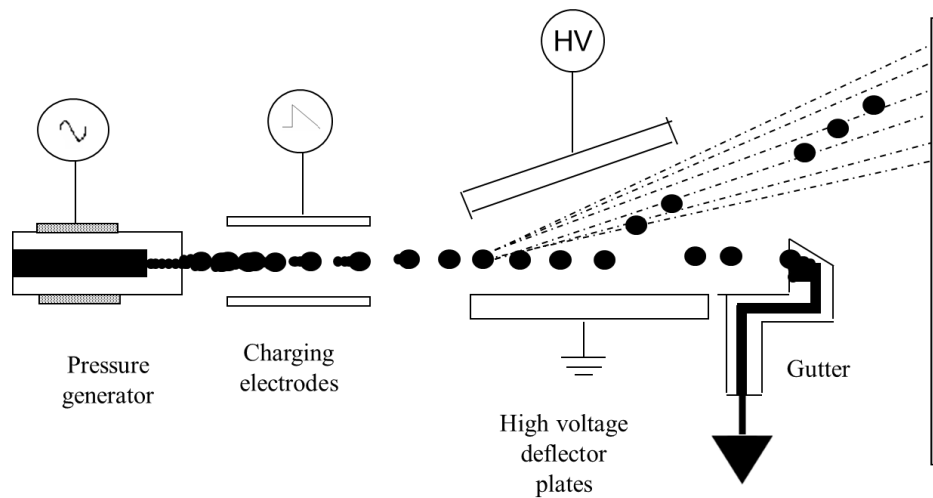


Figure 2.10 : Schematic diagram of continuous inkjet printer- multiple deflection system

#### 2.4.2. Drop on demand (DOD) inkjet printing

The DOD method is widely used in today's inkjet printers due to the fact that in this method the device ejects ink droplets only when they are used in imaging. Therefore this approach eliminates complexity of drop charging and deflection hardware required in CIJ systems. Most of the DOD printers in the market are using either a thermal or piezoelectric principle of operation.

The thermal inkjet method is mainly used in Canon, Xerox and Lexmark print heads. Depending on the location of the orifice, these printheads are again divided into two groups as: roof shooter and side shooter thermal inkjet. In the roof shooter heads, the orifice is located on the top of the printhead while in the side shooter it is located on the side nearby the header. These thermal inkjet printer heads contain a series of tiny chambers with heater for each chamber. Therefore in order to eject an ink droplet from each chamber a current pulse is passed through the heating element causing nucleation of ink bubbles at around  $300^{\circ}\text{C}$  -  $400^{\circ}\text{C}$ . Therefore even though this method is cost effective, it is not used for functional inks as these inks contains some materials which are not compatible with such temperatures.

The piezoelectric inkjet printheads are one of simplest form of printer heads to use and are commonly used for functional inks. Depending on piezoceramic deformation mode these printheads can be divided into four main types as: squeeze, bend, push and shear [72].

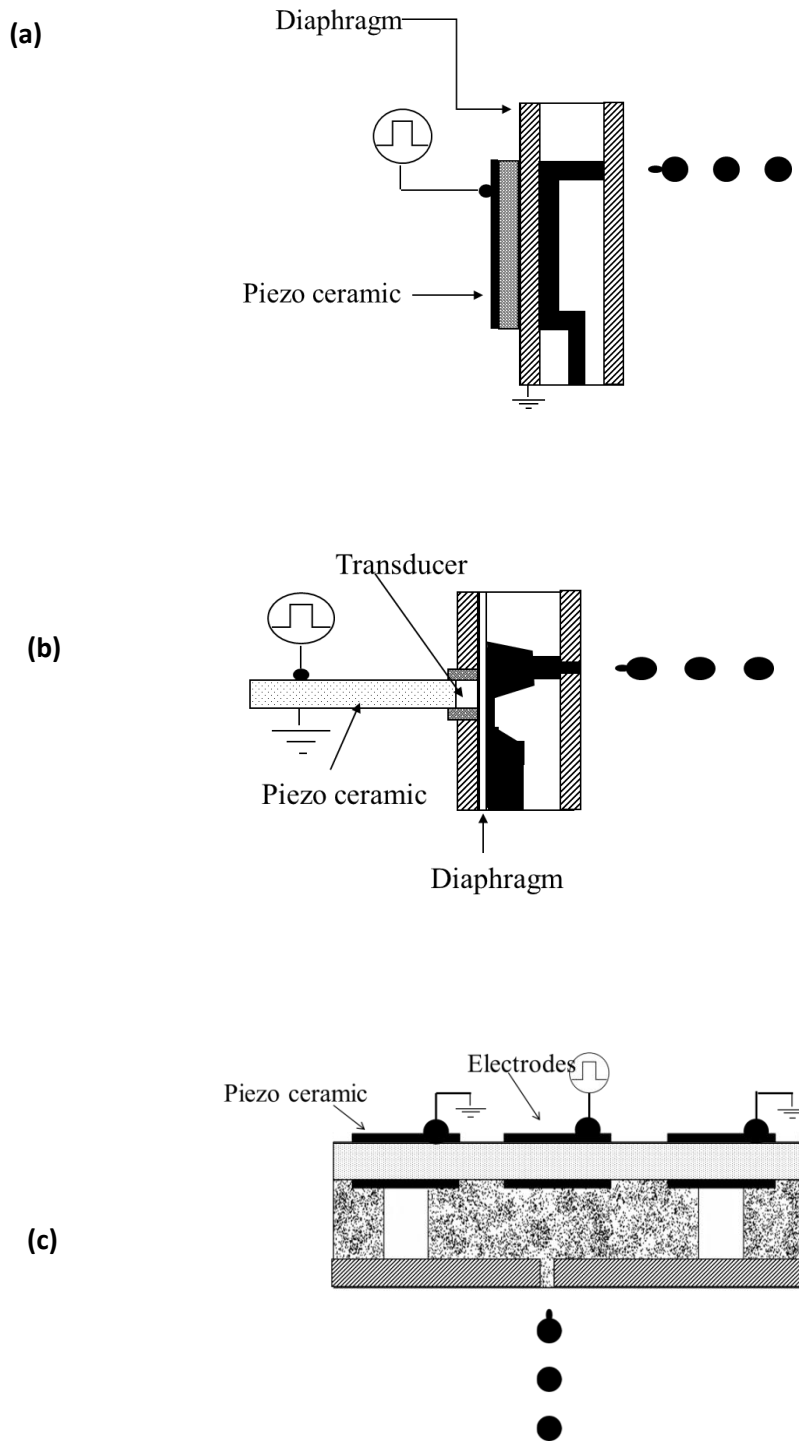


Figure 2.11 : Piezoelectric inkjet designs (a) Bend mode (b) Push mode (c) Shear mode

Generally, these printer heads contains nozzles and ink channels. In this technique the droplets are ejected by deforming piezoelectric transducers which leads to reduction in the volume of the ink chamber, and hence causes the drop ejection. Figure 2.11 shows three modes of piezoelectric inkjet heads, depending on the geometric arrangement of the transducer. (Xaar printer heads based on shear mode piezoelectric design principle were used to conduct the inkjet printing for this research work). In the shear mode, the shear action deforms the piezo plates against the ink to eject ink droplets. In term of design, the interaction between ink and piezomaterial is a key parameter for shear mode head design [72].

Epson and Tektronix are using bend mode configuration for their piezoelectric printer heads. In the bend mode the piezoelectric plates are bonded to the diaphragm to form a bi-laminator array of transducers to eject the ink droplets while in push mode, piezoelectric rod expands and pushes against the ink to form the droplets.

## **2.5 Post processing of TCOs**

Post processing or sintering is a vital process step for TCO production, especially for ink base deposition techniques to render the precursor compounds conductive and achieve crystallisation and the desired electrical and optical properties. The selection of post processing technique is mainly dependent on the substrate used, since high processing temperatures are not compatible with paper or flexible substrates that have relatively low glass transition temperature ( $T_g$ ), such as polyethylene terephthalate (PET).

In contemporary semiconductor devices, thermal annealing is widely used as the post processing technique to achieve the desired electrical and optical properties. When moving towards the flexible devices and due to the progressive reduction of device dimensions, novel annealing techniques such as laser material processing and flash lamp curing are required to reduce annealing time and temperature [73]. Another factor is that with these novel annealing techniques, the annealing time can be effectively

reduced to the seconds range and therefore can limit the thermally induced dopant diffusion to a required level.

The following sections discuss thermal annealing, photonic processing and other relevant post processing techniques that can be used to functionalise TCO and other materials.

### **2.5.1. Thermal annealing**

Thermal annealing is widely used to improve the crystalline quality and the dopant distribution of the as-deposited material by providing sufficient energy and mean free path of diffusion to atoms/ions to move into crystallographic sites. Typically for TCOs, high annealing temperatures ( $>500^{\circ}\text{C}$ ) and annealing times are required to achieve desired properties. The selection of the optimum annealing temperature and annealing time for TCOs are crucial as they depend on many factors. The TCO deposition technique, deposition parameters, the substrate, film thicknesses, dopant concentrations and post annealing environment are some of the key factors that can affect the selection of optimum annealing parameters.

Depending on the annealing time, thermal annealing is divided into two categories as: classical thermal annealing (CTA) and rapid thermal annealing (RTA). CTA is a process up to tens of minutes or hours and usually uses furnaces. In this process the heat can be either transferred by radiation, conduction or convection. The processing environment can be atmospheric conditions, high vacuum or gaseous environment. With RTA the processing time is usually several seconds or less and high intensity lamps (tungsten halogen bulbs, arc noble gas discharge lamps), hot chucks or hot plates are used. This is a cleaner process and less probable to contaminate than CTA.

Several workers have investigated the effect of CTA and RTA on TCOs. There are many reports about classical thermal annealing of sputtered and solution processed TCOs, but for clarification, only key works relating to  $\text{SnO}_2:\text{Sb}$  are discussed in this section.

Leem et al [74] carried out thermal annealing investigation for room temperature RF magnetron deposited ATO films for photovoltaic applications. They reported improved physical properties, such as crystallinity, resistivity, carrier concentration and Hall mobility when the films were annealed at 500<sup>0</sup>C. But with the higher annealing temperatures up to 700<sup>0</sup>C, the electrical properties of the films were degraded due to highly enhanced cracks along the grain boundaries.

Jeng [75] investigated the effect of thermal annealing in N<sub>2</sub> and O<sub>2</sub> environments for sol-gel spin coated films. The resistivity of the films annealed at 500<sup>0</sup>C in N<sub>2</sub> and O<sub>2</sub> environments with 5% of Sb concentration was observed to be reduced. He also reported about improvement to the crystallinity of the films with the annealing temperature.

Park et al [76] reported thermal annealing of sol-gel dip coated SnO<sub>2</sub>:Sb on ceramic Nextel and E-glass cloths. In this investigation the layers were annealed between 550<sup>0</sup>C and 900<sup>0</sup>C. With the increase of temperature, the sheet resistance was reduced around 30 - 15 Ω/sq. These films were also initially fired at 500<sup>0</sup>C for shorter periods during the deposition between each layer.

Rapid thermal annealing is not extensively studied for SnO<sub>2</sub>:Sb, but used for other TCOs such as ZnO [77][78], Indium Zinc Tin Oxide (IZTO) [79] and ITO [80].

Recently Lim et al [51] reported successful RTA for inkjet printed SnO<sub>2</sub>:Sb films in oxygen/nitrogen gas chamber and for about 5 mins. The results show that when annealing at 700<sup>0</sup>C, the sheet resistance was reduced to 1.7 x 10<sup>3</sup> Ω/sq for 350 nm thick films.

Boudiar et al [81] reported about successive RTA of SnO<sub>2</sub>:Sb for thinner layers (<150 nm) deposited by sol-gel dip coating technique. These films shows some densification and crystallite size increases and found to be more homogeneous compared to CTA films.

### 2.5.2. Photonic processing

With the advancement of technology there is a clear and increasing interest in short duration (far below one second) post processing techniques such as photonic processing. Laser processing and flash lamp annealing (FLA) are well known photonic processing techniques, where processing times are in milliseconds (ms) to femtosecond (fs) range.

Even though FLA is still not fully implemented process to functionalise TCOs, during the past decade a number of groups have reported work in this area. Figure 2.12 show the typical flash lamp system used for annealing. The main issues relating to this process are reproducibility of the conditions, homogeneity over the process area and diffusion of heat into the substrate [73].

Skorupa et al [82] reported about flash lamp annealing of ITO and ZnO films. For the ITO films a reduction of resistance was reported with the increase of flash lamp voltage for the layers deposited on glass and PET plastic foil substrates.

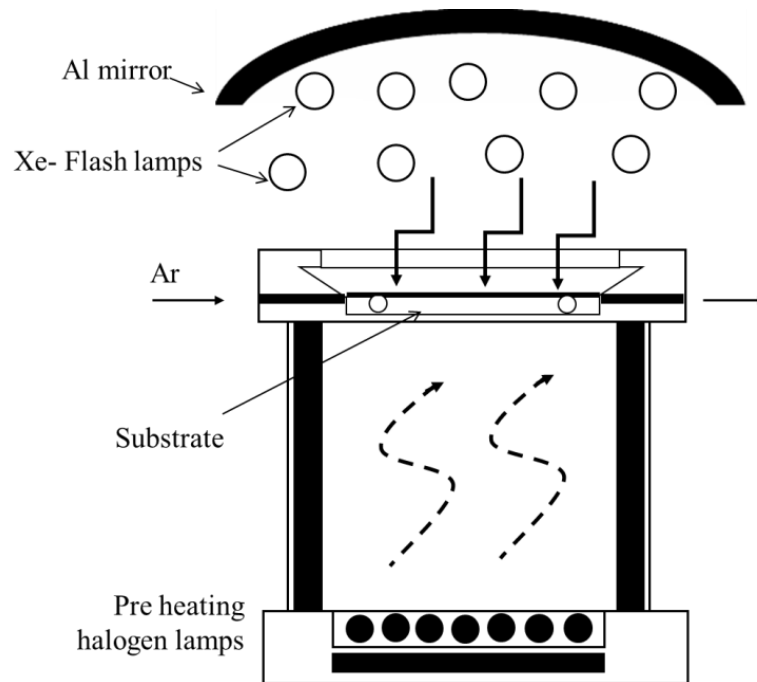


Figure 2.12 : Schematic diagram of flash lamp annealing system [73]

Since the invention of lasers (Light Amplification by Stimulated Emission of Radiation) by Schawlow at Bell Laboratories in 1958, science has found a number of applications of lasers from communication to materials modification. The interest in using lasers to improve material properties have increased in the last decades due to several reasons. Among them less risk of contamination, high precision processing capability, and the ability to control the processing depth without damaging the substrate which are unique to laser processing compared to the other techniques.

Several studies have reported successful functionalization of TCOs by laser processing.

Wang et al [45] reported on the use of UV pulse laser operating at 355 nm to perform heat treatment on the upper surface of Sb to induce diffusion process between Sb and SnO<sub>2</sub> bi-layers. The results shows that laser irradiation successfully resulted in the inter-diffusion of elements in the interface of Sb/SnO<sub>2</sub> bi-layer and as a result the resistivity of the laser treated films was reduced compared to the as-deposited films.

Aegerter et al [83] used a CO<sub>2</sub> laser to sinter SnO<sub>2</sub>:Sb films and reported an increase in particle size and packing density resulting in a reduction of resistivity that is four times less than the conventional furnace method.

Sandu et al [50, 84] reported about the possibility to use excimer lasers emitting at 248 nm and 193 nm to functionalise SnO<sub>2</sub>:Sb layers deposited by sol-gel dip coating techniques. The crystallisation of these films induces a gradient of grain sizes in the film thicknesses, the sheet resistance were reduced with the increase of laser fluence and number of pulses.

At Nottingham Trent University, the Thin Film and Displays research group has studied the use of excimer laser to functionalise the TCOs such as SnO<sub>2</sub>:Sb [8, 49] and ZnO, as well as thin films for luminescent applications. During the initial studies of SnO<sub>2</sub>:Sb, layers were deposited on glass and flexible substrates using solution based and sputtering techniques. In all cases the sheet resistance of the films was reduced with the increase of laser fluence and number of laser pulses. These studies formed the basis for this research study to investigate the detailed deposition, processing and analysis of

structural, electrical and optical properties of solution deposited, excimer laser processed SnO<sub>2</sub>:Sb films.

## **2.6 Applications of TCOs**

As previously mentioned in this chapter, today TCOs have a wide variety of applications not only in optoelectronics, but also in architectural and mechanical systems. This section briefly summarises some of the key applications of TCOs. It has been difficult to conclude which TCO is best for a specific application, because a given application may constrain the method of preparation and thereby affect the material choice.

### **2.6.1. Display devices**

TCOs are widely used as light transmitting electrodes in optoelectronic applications such as flat panel displays, light emitting diodes, emissive displays and touch panel controls, due to their metallic like conductivity and high optical transmission in the visible spectra. Tin doped indium oxide (ITO) is the material of choice for most transparent electrode applications, due to high etchability, high conductivity and ability to deposit at lower temperatures. But alternative materials like ZnO, SnO<sub>2</sub>:Sb are also of interest due to the fact that ITO is expensive for low cost large area applications and there is interest in the capability of alternative materials to produce nanoparticulate inks for low temperature deposition. Chapter 7 explains the application of SnO<sub>2</sub>:Sb used in this research as the transparent electrode for alternating current electroluminescent (ACEL) display devices.

### **2.6.2. Solar cells**

TCOs are applied in the front surface of the thin film solar cells to use as transparent electrodes to extract separated charge carriers from the absorbing region. These

materials enable the opportunity to fabricate large scale solar cells suitable for terrestrial applications. Recently, considerable interest has been directed to fabricate transparent oxide based solar cells [7, 85-88]. The TCOs are more effective in solar cells because of:

- The high transmission of TCOs, solar radiation can directly transmit to active region of the cell with no or little attenuation. This leads to an improvement in the sensitivity of the photon- energy portion of the solar spectra.
- Ease to fabricate the junction due to low fabrication temperatures
- The possibility to reduce the internal series resistance of the cell, which leads to improvement in output power.

SnO<sub>2</sub>:F is the material of choice for Cadmium telluride and some amorphous-silicon solar cells due to its thermal stability and lower fabrication cost. Also SnO<sub>2</sub>:F is used when making low-resistance electrical contacts in p-type amorphous silicon layers due to its high work function. In addition, lower temperature deposited TCOs are of interest for amorphous silicon based solar cells which are fabricated on flexible steel or plastic substrates.

### **2.6.3 Gas sensors**

Gas sensors are a major application of TCOs due to the unique properties of these semiconducting materials against other metal films. In metal films the conduction variation due to absorption (gas pressure) is very small, because it is caused by changes in mobility due to changes in surface scattering. But in TCOs, the conduction variation is mainly due to the changes in conduction band electrons or valance band hole concentration. The electron conduction variation with respect to the gas pressure is linear and rapid compared to the variation of mobility against pressure. So, due to this large and reversible variation in conductance with gas pressure, TCOs are more attractive as a material of choice for gas sensing electronic devices.

Tin oxide is the mostly common material to fabricate gas sensors to detect H<sub>2</sub>, CH<sub>4</sub> and LPG to prevent gas leakages and also to detect Carbon monoxide for pollution control and alcohol sensors to monitor drink driving [36].

#### **2.6.4 Low emissivity windows in buildings**

TCO films are commonly applied in window glasses to improve the energy efficiency of buildings. In window glass applications usually the conductivity of the TCO is irrelevant, but rather the plasma wavelength and durability of the material is important to obtain good light transmission in the visible range, while minimizing heat transmission. This feature is used to minimize air conditioning costs in the summer, and heating costs in the winter, in buildings equipped with appropriately coated windows. Further description about heat mirror applications can be found in [89].

Usually during winter months most of the solar spectrum needs to be transmitted into the buildings and therefore higher plasma wavelength materials are used as window coatings. SnO<sub>2</sub>:F is widely used for this purpose due to its considerable long plasma wavelength (>1.6 μm), durability and low cost for deposition. On the other hand for the summer months, the near infra-red portion of the incident light has to be reflected out to minimize the heat generation inside the buildings. Therefore shorter plasma wavelength materials are used [20].

#### **2.6.5. Defrosting windows**

Defrosting coatings are widely used in airplane cockpits, freezers in supermarkets, and some automobile windshields. By passing electric current through them, the coatings heat up and prevent moisture in the air condensing on the screens and obstructing the view. For large area applications like supermarket freezer windows, SnO<sub>2</sub> is used as the material for its high durability and low cost. But for airplane cockpits ITO is currently used as the material because of its lower resistivity and therefore ability to defrost with a lower voltage. The automobile industry still uses a thin layer of metallic alloys as the

material of choice on their windshields, because the 12V system in automobiles requires very low resistive coatings to pass the electrical current.

#### **2.6.6. Other applications**

Other than the previously mentioned applications, SnO<sub>2</sub> and other TCOs are widely used in oven windows, static dissipation coatings, in electromagnetic shielding and invisible security circuits. When using on ovens, the TCOs are helps to lower the outside temperature of the glass to a safe level. This is very useful in domestic ovens where the inside temperature can reach very high values. In security circuits, TCO coated glass is used over valuable pieces of arts and etc to protect from theft.

## **3 Experimental Procedures**

### **3.1 Introduction**

This chapter explains the experimental systems and techniques used throughout the research work. This includes the deposition, processing and characterisation of SnO<sub>2</sub>:Sb thin films, at NTU and via collaboration with FAB3D project partners.

With the industry trend towards large area, low cost, low volume microelectronic devices, traditional well established thin film deposition techniques have limits to use. Therefore this work is focused on direct writing and layering technologies to deposit solution processed materials to provide inexpensive, efficient and low temperature material deposition methods [90]. The first part of this chapter explains the ink preparation and solution based techniques used to deposit SnO<sub>2</sub>:Sb thin films. This chapter also discusses the excimer laser processing technique, which has been used to functionalise the deposited SnO<sub>2</sub>:Sb layers. Finally, the techniques used to undertake electrical and optical characterisation of the deposited, and post processed SnO<sub>2</sub>:Sb layers, are also presented.

### **3.2 Thin film deposition technologies**

#### **3.2.1 SnO<sub>2</sub>:Sb ink preparation and Spin Coating technique**

As part of the FAB3D project, ink preparation and the spin coating of ATO onto Eagle XG glass substrates was carried out by Keeling & Walker Ltd to provide samples for post processing and characterisation at NTU. The precise method of ink preparation and spin coating of ATO is proprietary to Keeling & Walker, however a summary of the process is as follows; The ATO is initially prepared as a high surface area powder which comprises nano-sized particles in an agglomerated form. This powder is then milled to break down the agglomerates and to obtain a stable colloidal dispersion

stabilised with ammonia solution. The average particle size of the dispersion is not greater than 50 nm. A stable aqueous dispersion is obtained by controlling the zeta potential simply by adjusting the pH during the milling process.

To prepare a basic ink suitable for spin-coating, the colloidal dispersion is diluted with water to reduce the solid content to 10 – 15% w/w. A small amount of wetting agent (0.2% Triton X100) is also added to aid substrate wetting. This ink has very low viscosity at around 1-2 cP.

A ChemSols CS-05 spin coater unit was used to spin coat the SnO<sub>2</sub>:Sb layers onto glass substrates. 50x50 mm Eagle XG glass substrates were used to deposit layers with the ink spun at a low speed of 1500 rpm for few seconds for each layer. Thicker layers were built up by repeating the application of ink and spinning, drying each layer before depositing the next consecutive layer. After deposition, the SnO<sub>2</sub>:Sb films were oven dried at lower temperature to remove ink residuals. For this research work, the number of spun layers were varied between 4 to 14 to obtain SnO<sub>2</sub>:Sb film thicknesses in the range of 0.15 to 1.2 μm.

### **3.2.2 Inkjet printing system**

The inkjet printing of the nanoparticulate ink of ATO was carried out by the author at Printed Electronics Ltd (PEL), Tamworth, UK. Initially the author undertook training on the printing equipment with PEL. Specifically, an ITI MDS 300 high precision material deposition system was used to inkjet print the ATO onto glass and other substrates. This deposition system utilizes inkjet printer head technology and the drop on demand ejection based technique to deposit materials as explained in 2.4.2. The PEL inkjet printing system and the associated Xaar printer head array set up are illustrated in figure 3.1. This inkjet printer head array set up allows the simultaneous printing of different inks and it also can be used to deposit chemically reactive species to perform chemical reactions on the substrate. A circulated water system is attached to the printer heads to control the ink temperature during printing. Using this system, the temperature

of the high viscosity inks can be increased to a certain level to ease the ink dragging from nozzles.

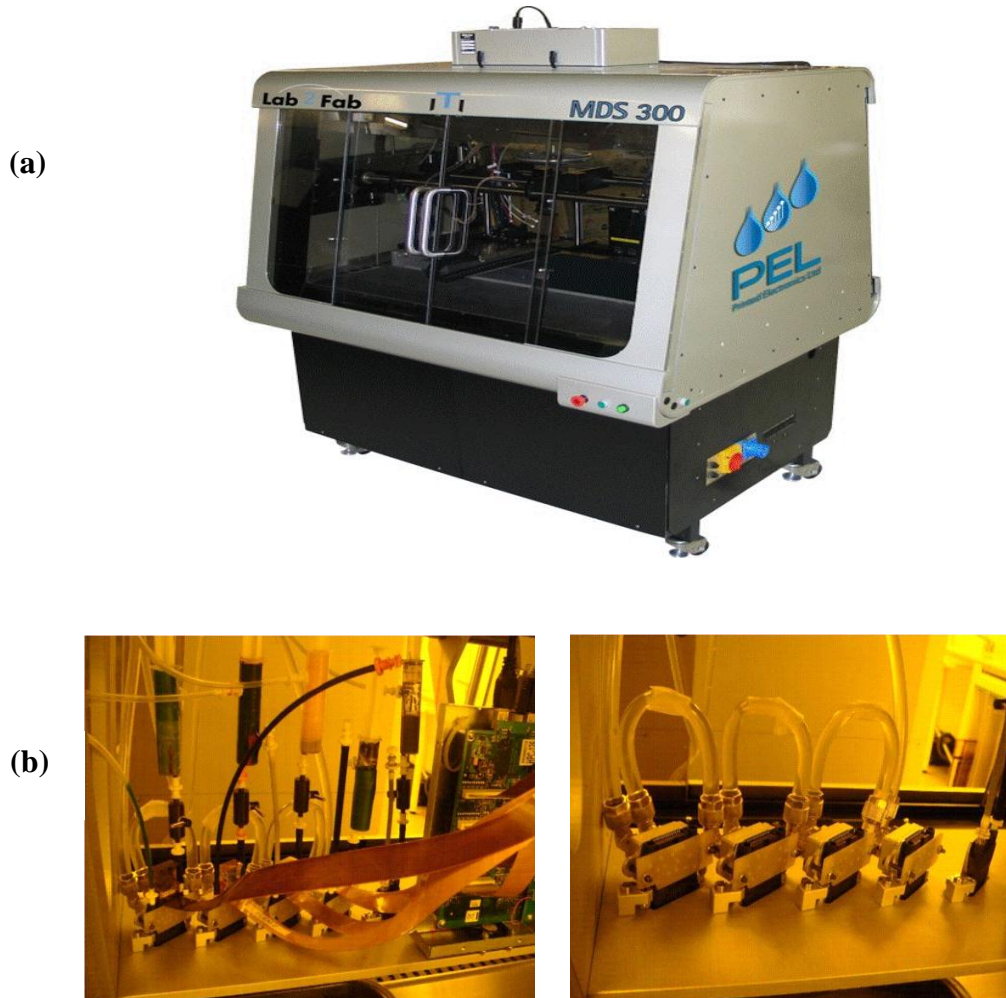


Figure 3.1 : Inkjet printing facilities at PEL (a) High precision inkjet printing system (b) Xaar printer head setup

Prior to inkjet print, the substrate was cleaned and surface treated using a Tantec Corona System. When depositing aqueous inks, surface modification of the substrate layer plays an important part as these inks shows lower wetting properties due to high surface tension. The ink was then printed on to the substrate. By varying the number of inkjet print passes the ATO layer thickness was controlled. After inkjet printing, samples were oven dried at 100<sup>0</sup>C for nearly 30 min to reduce the ink residuals.

### 3.3 Processing Technologies

#### 3.3.1 Laser Processing system

Excimer laser processing has been demonstrated as an effective post processing technique to functionalise TCOs [8, 49, 50, 91]. For this research work the SnO<sub>2</sub>:Sb samples were laser processed using the NTU Lambda Physik LPX305i excimer laser system. As shown in figure 3.2, the laser system consists of an excimer laser, configurable beam delivery and a sample manipulation stage. The excimer laser can be charged with Krypton Fluoride (KrF) or Argon Fluoride (ArF), emitting 20 ns pulses at  $\lambda = 248$  nm and  $\lambda = 193$  nm respectively. With the KrF configuration, the maximum energy density of the system is approximately 1.5 J.cm<sup>2</sup>. The laser pulse frequency can be varied between 1 - 25 Hz.

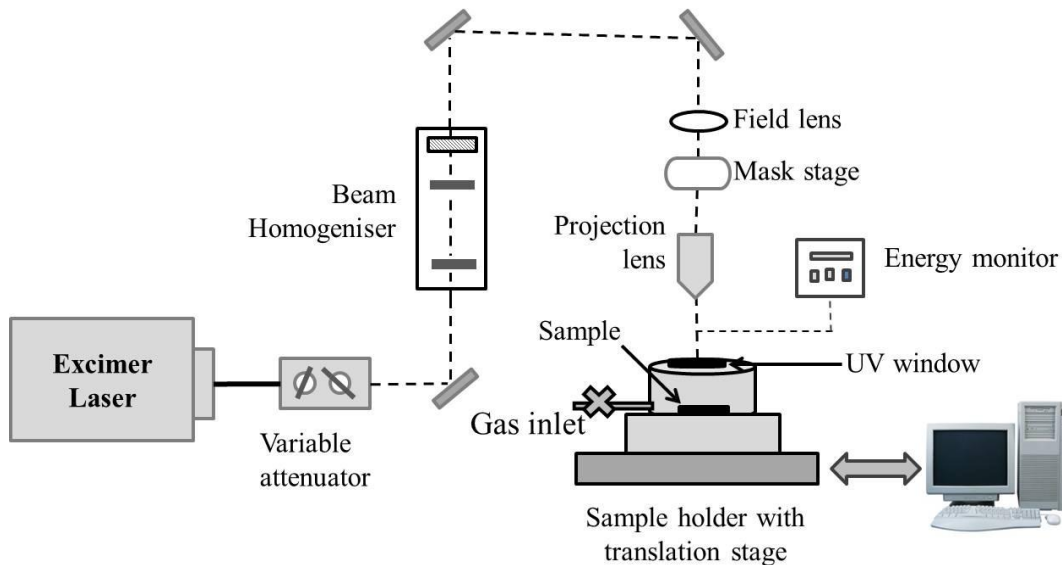


Figure 3.2 : Schematic of KrF laser processing system showing the homogenised beam delivery system and sample stage

When operating at 248 nm, the raw output beam of an excimer laser is a quasi-rectangular beam, approximately 10 x 40 mm with poor uniformity. Before it enters the homogeniser the laser beam is reflected by a 248 nm mirror and passes through a variable attenuator. Because the laser is run in constant energy mode, the variable

attenuator is used to change the fluence delivered to the sample. The homogeniser takes the raw, non-uniform laser beam and slices the input beam horizontally and vertically by using the 1<sup>st</sup> lens array. These beamlets are mapped across the entire output beam profile by using the 2<sup>nd</sup> lens array and a condenser lens. By varying the focal length of the condenser lens the spot size at the sample plane and the sample distance can be varied. With the current setup, a fixed condenser lens which is focused to a point 1m from the homogeniser to the sample plane was used. Field and projection lens sets were used to create a 10x10 mm (1x magnification) or 3x3 mm (5x magnification) spot sizes at the sample plane. The rotatable mask stage contains several masks which can be used to anneal/ ablate only the required sample area and patterns. The sample is placed in a pressure cell which has a quartz window and this enables processing at variable pressure and environments. The pressure cell was fixed to an X-Y translation stage which allows accurate step and repeat sample positioning for laser material processing.

### **3.4 Metrology systems**

Electrical and optical characterization facilities available at NTU and at partner laboratories have been utilised to characterise the as-deposited, thermal annealed, Laser processed and combined processed (thermal and laser processed) SnO<sub>2</sub>:Sb layers.

#### **3.4.1 Optical transmission**

For transparent conducting materials it is very important that the material is transparent to the visible region of the spectrum. In order to do that the plasma frequency of the material has to be near the border separation of visible and near infrared regions and the material absorption coefficient should be very low in the near UV-Visible- IR region. The transmission in the UV region is limited by the Band gap,  $E_g$ , of the material as photons with higher energy than  $E_g$  are absorbed. Materials such as Tin Oxide have absorption in the UV part of the UV-VIS-IR spectrum and the reflection in the NIR making it a perfect candidate as a TCO.

For this research work the transmission spectra of the ATO samples were measured using a Filmetrics F20 thin film analyser. Figure 3.3 shows the Filmetrics F20 setup configuration for transmission measurements. The spectrometer uses an in-built tungsten-halogen bulb to generate the light and measure the transmission between the  $\lambda = 395$  and  $\lambda = 1000$  nm. During the transmission measurement the sample is illuminated with white light. A fibre optic bundle is used to deliver the light to and from the sample. The collected light from the sample is then passed to the spectrometer. The spectrometer uses a diffraction grating and a linear photodiode array to disperse the light and to measure the light at different wavelengths. For the transmission measurements the sample has to be flat and the front and backsides are required to be parallel.

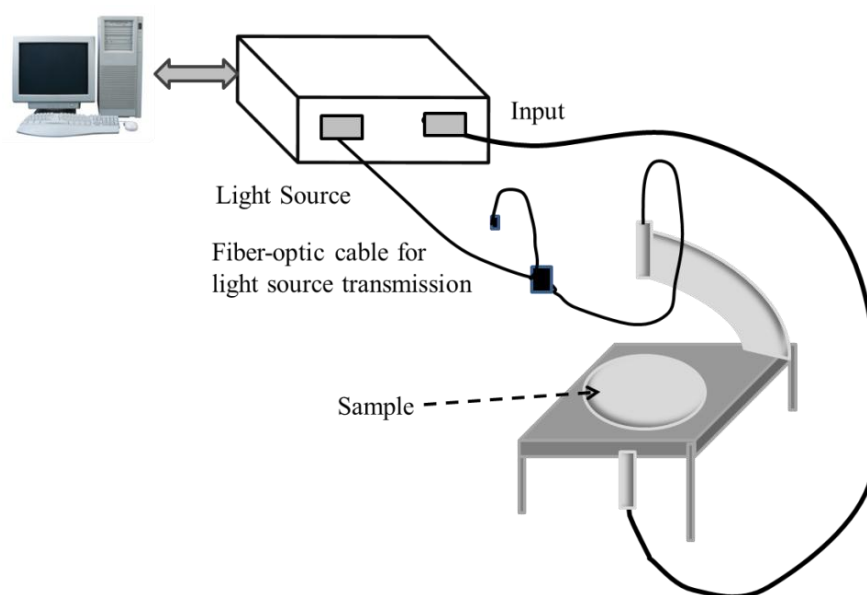


Figure 3.3 : Filmetrics F20 set up configuration for transmission measurements.

To measure a sample first the spectrometer was set to transmission mode and was switched on for at least 15 minutes to get a stabilised light. Then a baseline measurement and the dark measurement were taken.

### 3.4.2 Surface roughness and step height

A VeecoWyko NT1100 optical profiling system was used to image the spin coated, inkjet printed, and dip coated ATO layers for the surface roughness and step height measurements. Figure 3.4 illustrates the schematic diagram of the Wyko NT 1100 setup. The optical profiler has two modes of operations;

- Phase - Shifting Interferometry (PSI) and
- Vertical –Scanning interferometry (VSI)

The PSI mode allows measurement of smooth surfaces and small steps (up to 160 nm) while to resolve rougher surfaces, and steps up to few millimetres height the optical surface profilers use VSI mode.

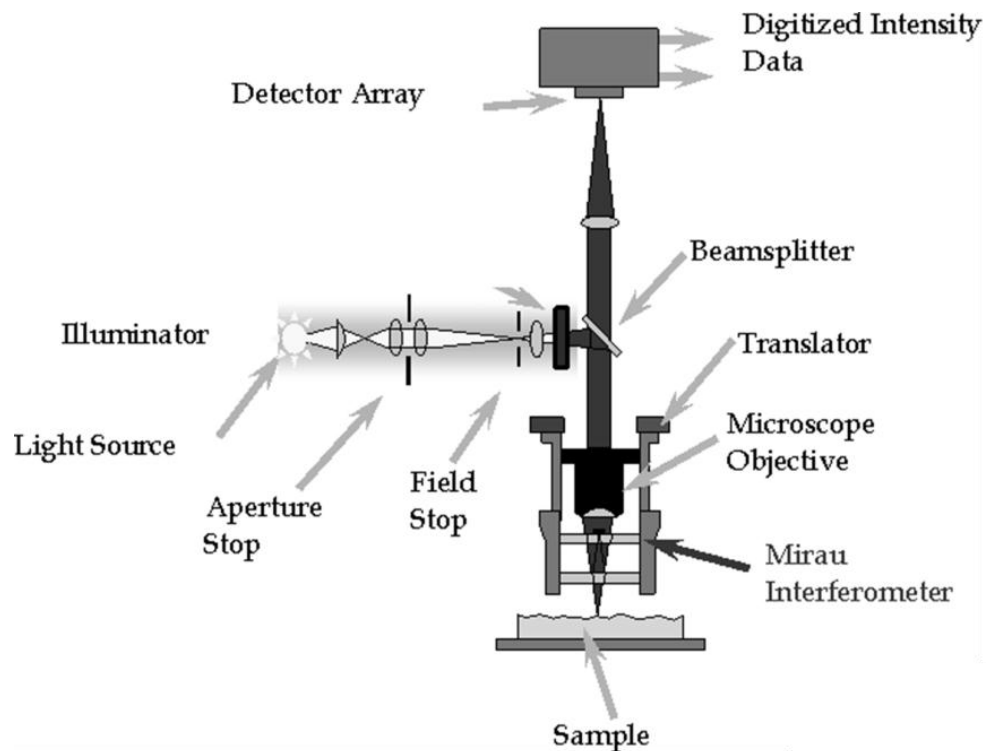


Figure 3.4 : Schematic setup of the Wyko NT1100 system for optical profiling [90]

In both techniques white light reflected from a reference mirror combines with light reflected from the sample to produce interference fringes, where the best-contrast fringe

occurs at best focus. For the PSI mode when the measurement is taken, the reference surface linearly moves a known amount to phase shift between sample and reference beams. But for the VSI mode, the white-light source is filtered by a neutral density filter, which preserves the short coherence length of the white light, and the system measures the degree of fringe modulation, or coherence, instead of the phase of the interference fringes. For this work the VSI mode was used to measure the step heights of the as-deposited SnO<sub>2</sub>:Sb layers.

### **3.4.3 Surface morphology**

#### **3.4.3.1 Transmission Electron Microscopy (TEM)**

Transmission electron microscopy is an important tool for studying fundamental properties of materials due to its very high spatial resolution [92]. The operating beam voltages of TEMs are between 100 and 400 kV. As the name implies, the sample needs to be very thin in the order of microns, so as to be transparent to the incident electron beam. For the TEM operation the sample is supported on a small copper grid about 3mm in diameter, which is inserted to the holder positioned at the centre of the column. The optical set up of a TEM mainly contains: objective, intermediate, and projector lenses, and a fluorescent screen. The objective lens used for imaging and the other two lenses are used for magnification. The final real image can be viewed or captured on a charge coupled device camera (CCD) imager or on a fluorescent screen. The objective aperture which is positioned just above the objective lens is important for dark field microscopy. In order to reduce scattering to a negligible level the TEM column must operate under high vacuum environment ( $10^{-7}$  Torr).

The cross sectional morphology of the as-deposited, thermal annealed, KrF laser processed and combined processed (thermal and laser processed) SnO<sub>2</sub>:Sb was examined using a Joel 200FX TEM operating at 200 kV. A series of SnO<sub>2</sub>:Sb on Eagle XG glass substrates was post processed by the author and send to Sonsam Ltd, Glebe Laboratories, Ireland for TEM analysis. A Focused Ion Beam (FIB) technique was used

to prepare the functionalised and as-deposited SnO<sub>2</sub>:Sb samples for TEM analysis. The trench technique [93] was used to thinning the area of interest to a small rectangular ‘slab’ of material, and to prepare for FIB microscope milling. Further sample preparation details can be found in [94] .

#### **3.4.3.2. Scanning Electron Microscopy (SEM)**

SEMs are versatile instruments to examine the cross section and the surface of materials, because they combine high spatial resolution with depth of field in the scanning image. Also, in comparison to TEM, SEM requires minimal sample preparation. Figure 3.5 shows the fundamental components of the SEM. The electron gun forms a source of electrons which are passed through one or more electron lenses and towards the anode to form an image of the electron source in the plane of the specimen, with a diameter of few tens of nanometres. As a result of the primary electron beam movement at the surface of the specimen, secondary electrons are produced and are detected by an electron collector. The collected signal is enhanced through an amplifier and the resultant image passes to the display for viewing.

A Joel JSM 840A scanning electron microscope was used by the author to inspect the surface of the inkjet printed and post laser processed ATO layers. Before being imaged, a small section of the area of interest was attached to a cylinder stub using Carbon sticky pads. Then by using an Edwards sputter coater, approximately 20 nm of gold was deposited to minimize the charge build up.

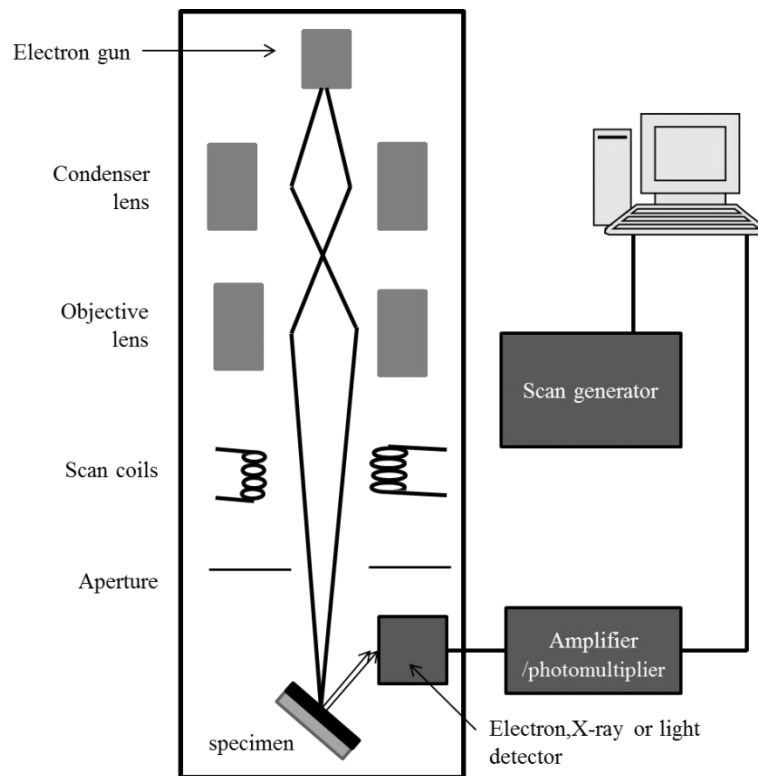


Figure 3.5 : The reduced form of Scanning Electron Microscope.

#### 3.4.4 X-ray diffraction (XRD)

X-ray diffraction is a widely used characterisation technique to identify the crystalline phases and to measure structural properties of materials. Consider an incident beam of x-rays interacting with a crystalline sample as shown in figure 3.6. X-rays are scattered coherently by the periodic array of atoms in the material, giving rise to constructive interference at certain angles of reflection. Diffraction occurs as the wavelength of the incident x-rays is of a similar magnitude to the lattice spacing within the material. The interference of the diffracted x-rays can be described by Bragg's Law.

$$\lambda = 2 d_{hkl} \sin \theta \quad \text{Eq 3.1}$$

Where  $\lambda$  is the wavelength of the X-rays,  $d_{hkl}$  is the distance between two adjacent planes of miller indices ( $hkl$ ) and  $\theta$  is the angle between incident beam and the crystal surface.

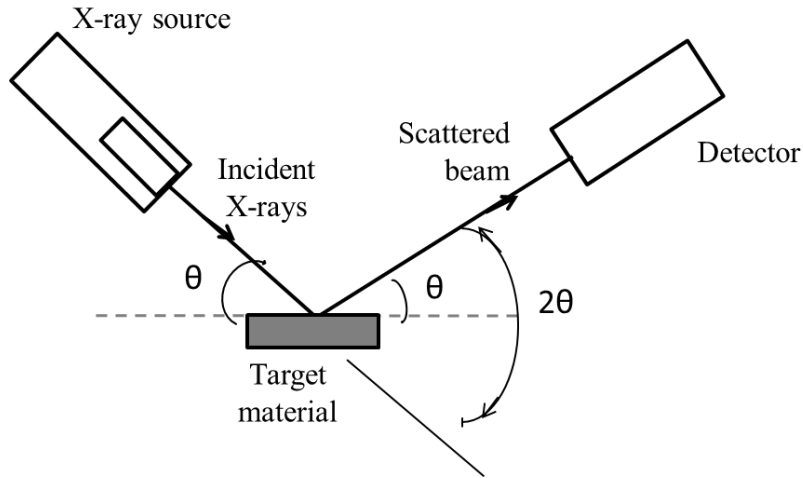


Figure 3.6 : Schematic of X-ray diffractometer

The solutions of the Bragg equation are widely used to determine the lattice constants an epitaxial growth material. This may also use to quantitatively determine the deviation of crystalline quality from the ideal lattice of an epitaxial growth material.

X-ray diffraction scans of as-deposited, thermal annealed and laser processed  $\text{SnO}_2:\text{Sb}$  were collected at NTU using a Philips PANalytical X'Pert Pro system with monochromated  $\text{Cu-K}_{\alpha 1}$  radiation source,  $\lambda = 1.54056 \text{ \AA}$ . The XRD system operates at 45KeV and 40mA:and for  $\text{SnO}_2:\text{Sb}$  the diffraction intensity was examined over and angular range of  $2\theta = 20^\circ - 80^\circ$  with the step size of 0.016

The measured width of the diffraction peaks was used to estimate the particle size of the as-deposited and post processed  $\text{SnO}_2:\text{Sb}$  using the Scherrer formula (Equation 3.2).

$$D = \frac{0.89 \lambda}{\beta \cos\theta} \quad \text{Eq 3.2}$$

Where,

$D$  is the particle diameter,  $\lambda$  is the Wavelength of the incident x-ray radiation,  $\beta$  is the Full width at half maximum height of the peak and  $2\theta$  is the diffraction angle.

When calculating crystallite sizes, the crystals are assumed to be free from microstrains and defects. Therefore the broadening is assumed to depend only on the crystallite size and diffractometer characteristics. For all the measurements the same diffractometer was used and due to the nanocrystallite nature of the SnO<sub>2</sub>:Sb, broadening due to crystallite size is also assumed to be significantly larger than the instrumental broadening.

### 3.4.5 X-ray Photoelectron Spectrometry (XPS)

XPS, also known as Electron Spectroscopy for Chemical Analysis (ESCA) is a vacuum based analytical technique, which gives useful information such as composition and chemical state of the materials [95, 96]. A photoelectron spectroscopy system is mainly equipped with a source of monochromatic X-rays and a hemispherical electron energy analyser. The X-rays are produced at the anode of the monochromator X-ray source by bombardment of electrons created at the filament. Once these X-ray photons irradiate the sample, the photoelectrons are ejected. This process can be expressed as [97],

$$BE = h\nu - KE - \phi \quad \text{Eq 3.3}$$

Where,  $BE$  is the binding energy of the electron in atoms,  $h\nu$  is the photon energy of X-ray source,  $KE$  is the kinetic energy of the emitted electron and  $\phi$  is the spectrometer work function.

The hemispherical energy analyser is used to determine the energy of the photoelectrons and it gives a spectrum with a series of photoelectron peaks. These photoelectron peaks are characteristic to each element of the material and therefore this technique can be used to determine the composition of the material surface. XPS is surface sensitive; the intensity of the emitted photoelectrons with no energy loss is the only concern. The emitted photoelectrons from below the uppermost surface with some loss of energy contribute to the background of the spectrum and the photoelectrons emitted deep within the material lose their energy to inelastic collisions and are not emitted from the surface.

For this research work XPS analysis was carried out at Brunel University, UK. To study the extent of segregation of Antimony with respect to the different post processing techniques of the spin coated SnO<sub>2</sub>:Sb samples, the author KrF laser processed and thermal annealed the 12x spun layers of ATO and sent them to Brunel University.

The samples were examined by using VG Escalab 210 photoelectron spectrometer. The X-ray source was a polychromatic AlK $\alpha$  source (1486.6 eV). The X-ray gun was operated using 10 kV accelerating voltage and 20 mA electron bombardment current. The area corresponds to the data acquisition was a circular area of ~2mm in diameter. The pass energy for survey scans were 100 eV with step size of 1 eV. The component specification high resolution scans were conducted with pass energy of 10 eV with step size of 0.05 eV.

### **3.4.6 Sheet resistance**

#### **3.4.6.1 Four Point Probe**

The sheet resistance is defined as the resistance between the opposing edges of a square of a sheet to be measured [92]. For a square cross sectional area of a film through which the measuring current is flowing, the sheet resistance ( $R_s$ ) is given by,

$$R_s = \rho/t \tag{Eq 3.4}$$

Where  $t$  – Film thickness and  $\rho$  - electrical resistivity.

For this project a four point probe system has been used to measure the sheet resistance of as-deposited, thermal annealed and laser processed SnO<sub>2</sub>:Sb layers. The four point probe system consists of a linear four point probe, a voltmeter and a current source. A Times Electronics 1021 DC Current Source was used apply the current during measurements. Using this source the applied current range can be varied from micro-

amps level to 100 mA. A Signatone four point probe station with SP44045TS probe head was used to measure the samples. The four point probe tips were made out of Tungsten carbide and the spacing between the tips ( $d$ ) was 1mm and a 45 g pressure was applied to the tips during measurements. A schematic of the four point probe is shown in figure 3.7.

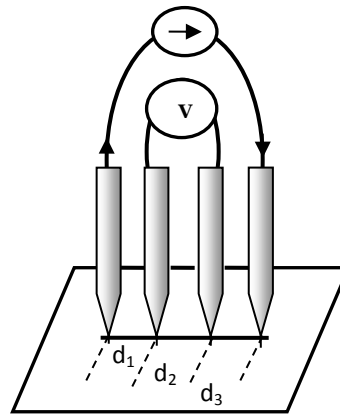


Figure 3.7 : Schematic drawing of the linear four point probe

When the probes are placed on the film of semi- infinite volume, the resistivity is given by,

$$\rho = \frac{V}{I} \frac{2\pi}{\frac{1}{d_1} + \frac{1}{d_2} - \frac{1}{(d_1+d_2)} - \frac{1}{(d_2+d_3)}} \quad Eq3.5$$

Where  $V$  is the measured voltage and the  $I$  is the current from the current source

For an equidistance probe spacing,

$$d_1 = d_2 = d_3 = d$$

Then

$$\rho = \frac{V}{I} \frac{2\pi}{1/d} = \frac{V}{I} (2\pi d) \quad \text{Eq 3.6}$$

For an infinite thin film on an insulating material the Eq 3.6 can be expressed as;

$$\rho = \frac{V}{I} \frac{\pi t}{\ln 2} \quad \text{Eq 3.7}$$

### 3.4.6.2 Van der Pauw technique

The Van der Pauw technique is widely used in the semiconductor industry to determine the resistivity of a uniform sample. For this research work this technique has been used to measure the resistivity of as-deposited, and post processed SnO<sub>2</sub>:Sb samples for Hall effect measurements. The geometry of the Van der Pauw measurement is shown in figure 3.8.

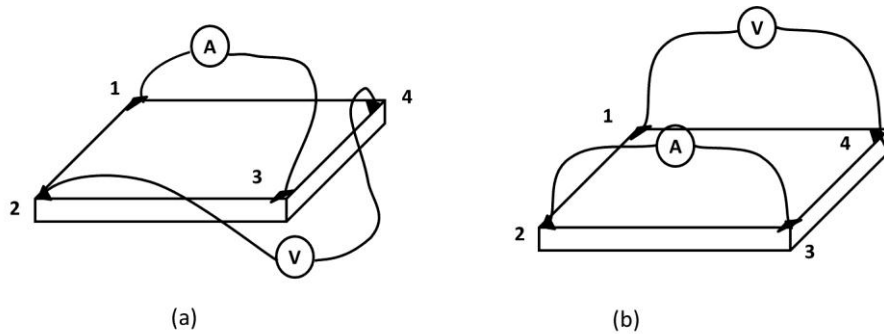


Figure 3.8 : Geometry of the Van der Pauw technique for measurement of sheet resistivity

There are two characteristic resistances  $R_A$  and  $R_B$  associated with the Van der Pauw technique that are calculated by means of the following equations;

$$R_A = V_{43}/I_{12} \quad \text{and} \quad R_B = V_{14}/I_{23}$$

$R_A$  and  $R_B$  relate to the sheet resistivity,  $R_s$  through the Van der Pauw equation by: [98]

$$\exp\left(-\pi \frac{R_A}{R_s}\right) + \exp\left(-\pi \frac{R_B}{R_s}\right) = 1 \quad \text{Eq 3.8}$$

By solving Eq 3.8, and using Eq 3.2 the bulk sheet resistivity can be obtained.

### 3.4.7 Hall Effect

The Hall Effect was first discovered by Edwin H. Hall in 1879 [99] when he found a measurable transverse voltage across a current carrying sample in an applied magnetic field. From that point onwards this technique has been widely used to determine the polarity of charge carriers and to study the carrier transport in metals and semiconductors.

The basic physical principle used in Hall Effect measurement is the application of the Lorentz force. Consider a thin bar of semiconductor (thickness =  $d$ ) with four ohmic contacts placed in a magnetic field,  $B_x$  as shown in figure 3.9.

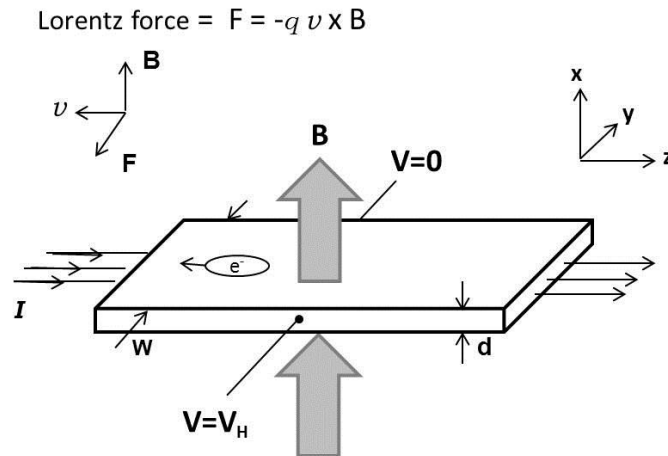


Figure 3.9 : The standard geometry for the Hall Effect

When electrons move perpendicular to an applied magnetic field,  $B_x$ , they experience a Lorentz force normal to both  $B_x$  and  $I_z$  and move in response to this force and the force

affected by internal electric field. This results in the movement of charge and the generation of the Hall voltage,  $V_H$ :

$$V_H = \left(\frac{1}{nq}\right) \frac{I_x B_x}{d} \quad \text{Eq 3.9}$$

Where  $n$  is Bulk charge carrier density and  $q$  is the elementary charge.

Using Eq 3.7, the Hall coefficient,  $R_H$  is defined as,

$$R_H = \frac{1}{nq} \quad \text{Eq 3.10}$$

When the majority carriers are electrons, the Hall coefficient is negative and for majority hole carriers the sign of the coefficient is positive.

When the thickness of the layer is not known, the sheet carrier density ( $n_s = n d$ ) is used and

$$n_s = \frac{I B}{q V_H} \quad \text{Eq 3.11}$$

The resistivity of the thin bar of material can be expressed as,

$$\rho = \frac{1}{\mu n q} = R_s d \quad \text{Eq 3.12}$$

where  $\mu$  is the Carrier mobility

Therefore,

$$\mu = \frac{1}{q n_s R_s} \quad \text{Eq 3.13}$$

For this work, twelve layer spin coated SnO<sub>2</sub>:Sb films on glass substrates were cut into 10x10 mm size and post processed (KrF laser processing, thermal anneal) for Hall effect measurements. The Hall coefficients were evaluated by the Van der Pauw technique using an Ecopia Hall measurement system (HMS-3000) with a custom-built cryogenic cooling system at Oxford University, UK. By measuring  $V_H$  and by set or knowing  $I, B$  values, the carrier density and carrier mobility of the material was calculated for different post processing conditions.

## **4. Post processing of Inkjet printed and Dip Coated SnO<sub>2</sub>:Sb**

### **4.1 Introduction**

The electrical and optical properties of the transparent electrodes not only depends on the chemical composition but also on the method used for layer deposition. Among the deposition techniques, printed electronics techniques such as Inkjet printing have received much interest for large scale, low cost flexible manufacturing.

This chapter discusses the use of dip coating and inkjet printing techniques which have been used to investigate the deposition of SnO<sub>2</sub>:Sb for potential use in device structures. The electrical, optical and structural techniques that have been used to characterise the layers are also discussed.

### **4.2 Dip coated SnO<sub>2</sub>:Sb on glass substrate**

In the dip coating technique, the substrate is inserted into a SnO<sub>2</sub>:Sb solution (ink) and is withdrawn in a controlled manner to form the layer. This is followed by gravitational draining and solvent evaporation accompanied by the post processing [100]. This technique requires potentially less equipment and process time compared to the other conventional thin film deposition processes; thus it is a good candidate to deposit thin films for initial experimental evaluation.

The purpose of the investigation was to evaluate the K&W ink and materials, with the intention to then move onto inkjet printed versions. For this research work the SnO<sub>2</sub>:Sb samples were received from Keeling & Walker Ltd (K&W) and Printed Electronics Ltd (PEL). Throughout this work the aqueous dispersions of SnO<sub>2</sub>:Sb were formed by the Keeling & Walker Ltd and the precise method of SnO<sub>2</sub>:Sb preparation was proprietary to them. The SnO<sub>2</sub>:Sb aqueous dispersion contains 15% SnO<sub>2</sub>:Sb solids and had a small amount of surfactant added to aid wetting and hydroxyethyl cellulose to increase

viscosity. The initial dip coated SnO<sub>2</sub>:Sb batch from Keeling & Walker Ltd contained 6 samples. These films were deposited onto 50 x 50 mm<sup>2</sup> Eagle 2000 glass substrates, and each sample was dip coated with SnO<sub>2</sub>:Sb across an area of 5cm x 4cm on one side of the substrate. The batch from Printed Electronics Ltd contained 11 samples coated onto 25x 25 mm<sup>2</sup> Eagle 2000 glass substrates. The SnO<sub>2</sub>:Sb ink used for these PEL films were also based on the Keeling & Walker aqueous dispersion, but were formulated by Sun Chemicals, UK for inkjet printing work. Further to deposition the samples were oven dried to remove the ink residuals. A summary of the samples used for this study is shown in Table 4.1.

K & W	KWATO1	Thermal annealed at 700 <sup>0</sup> C ~1 hr
	KWATO2	Oven Dried 100 <sup>0</sup> C ~1hr
	KWATO3	
	KWATO4	
	KWATO5	
	KWATO6	
PEL	PEATO1-1	Oven dried 200 <sup>0</sup> C ~1 hr
	PEATO1-2	
	PEATO1-3	
	PEATO1-4	
	PEATO1-5	
	PEATO2-1	Oven Dried 100 <sup>0</sup> C ~1hr
	PEATO2-2	
	PEATO2-3	
	PEATO3-1	
	PEATO3-2	
	PEATO3-3	

Table 4.1 : Summary of the Dip coated SnO<sub>2</sub>:Sb samples from K&W Ltd and PEL.

**4.2.1 Electrical and optical characterisation of as-deposited SnO<sub>2</sub>:Sb**

The as-deposited SnO<sub>2</sub>:Sb films were optically and electrically characterised by the author at NTU. In all cases, the sheet resistance of the SnO<sub>2</sub>:Sb thin film was measured using four point probes. For each sample four areas were measured across the film and the average sheet resistance was recorded. The oven dried at 100<sup>o</sup>C samples from K&W Ltd showed an average sheet resistance of 1.0 MΩ/sq (± 20%) while the sample thermal annealed at 700<sup>o</sup>C showed 0.36 KΩ/sq (±18%). the sheet resistance measurements across the samples shows some variation. This was mainly due to the deposition technique used and the resultant thickness variation across the sample. Figure 4.1 shows the average sheet resistance variation of as-deposited dip coated ATO samples. The average sheet resistance of the PEL samples oven dried at 200<sup>o</sup>C was 1.4 MΩ/sq (± 11%) and the samples oven dried at 100<sup>o</sup>C were approximately 3.5 MΩ/sq (± 15%). The variations between the two sets were mainly due to the oven temperatures used. The films which are oven dried at higher temperatures produce the most conductive films.

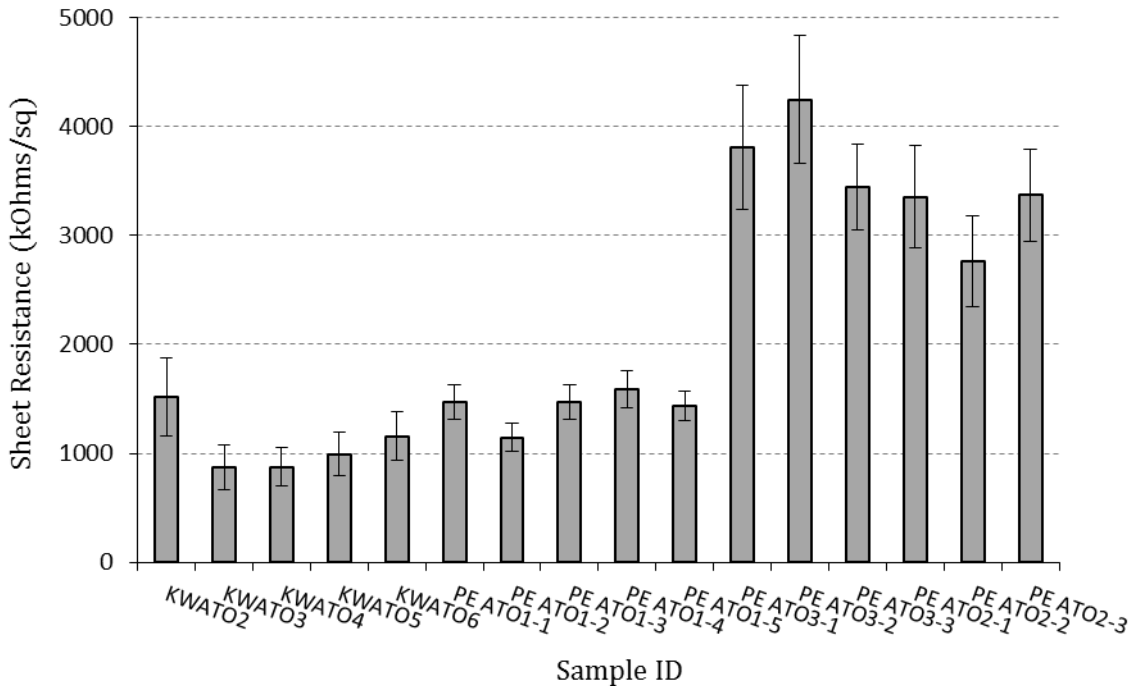


Figure 4.1 : Sheet resistance variation of the as-deposited dip coated SnO<sub>2</sub>:Sb.

Film thickness of the as-deposited dip coated SnO<sub>2</sub>:Sb samples was measured using a Dektak 6M Stylus Profilometer. In order to facilitate this edge measurement, five areas of the SnO<sub>2</sub>:Sb sample KWATO3 were KrF laser ablated using the excimer laser system at high fluences, typically 100 mJ/cm<sup>2</sup>, 10-15 pulses. The ablated area was inspected using the Wyko NT110 Optical Profilometer in order to identify the edge regions to use for thickness measurement. Figure 4.2 shows a typical ablated area of the film. The step height of an ablated area was measured and the average value was considered. Figure 4.2(b) illustrates the step profile of an SnO<sub>2</sub>:Sb film using a stylus profilometer. The average thickness of a dip coated SnO<sub>2</sub>:Sb was around 950 nm ( $\pm 5\%$ )

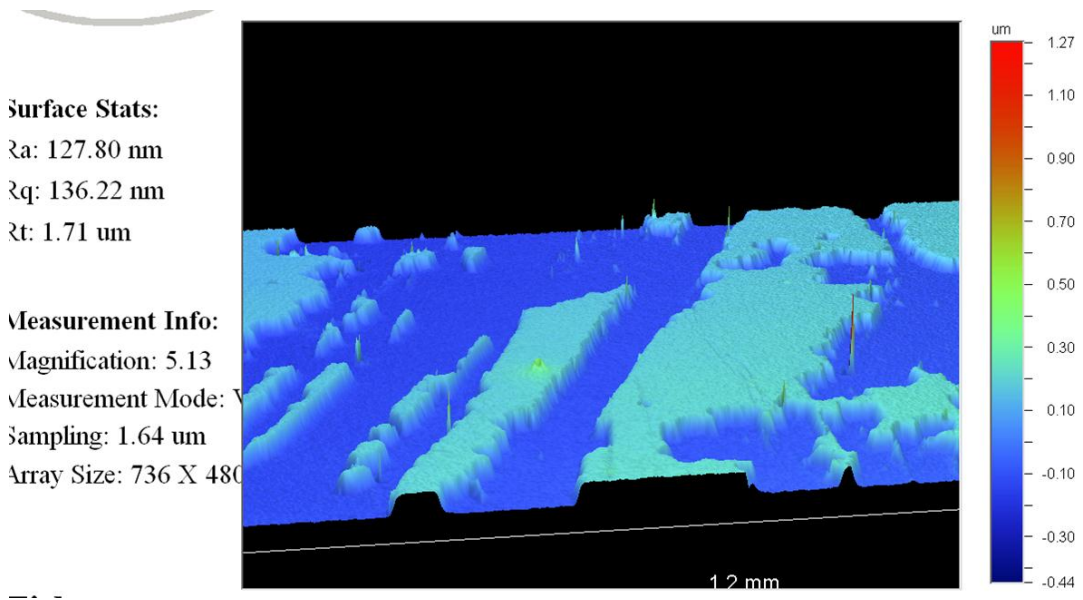


Figure 4.2(a) : KrF laser ablated area of dip coated SnO<sub>2</sub>:Sb film

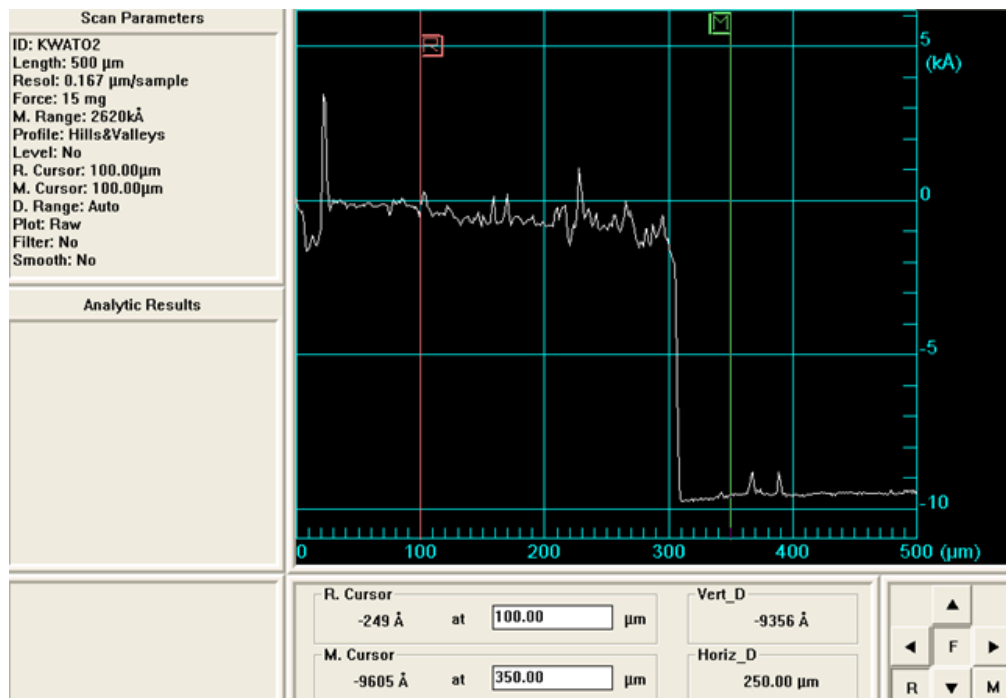


Figure 4.2(b) : Step profile of the ablated area of the dip coated SnO<sub>2</sub>:Sb -K& W

#### 4.2.2 Excimer laser processing of Dip coated SnO<sub>2</sub>:Sb

Previous work by the display research group, Nottingham Trent University [49, 101] has demonstrated that Excimer laser processing is a post processing technique that has potential to produce functionalised SnO<sub>2</sub>:Sb layers. As an initial evaluation for this research project, the dip coated samples were processed using the 248 nm excimer laser system described in section 3.3.1. The laser parameters varied were laser fluence and number of pulses, with the samples laser processed in air at atmospheric pressure. A variable attenuator was used to change the laser fluence. Due to the limited number of dip coated SnO<sub>2</sub>:Sb samples, KWATO2 and KWATO6 were used for the laser processing experiment and both samples were laser processed with the same conditions for comparison. The position of the laser processed area on the samples was varied to address the expected fluctuations due to the thickness/sheet resistance variations across the samples. The processing areas were marked on the rear glass side of the sample and labelled with the processing fluence. Then by varying the number of irradiated laser

pulses, the samples were laser processed and the sheet resistance of the processed area was subsequently measured using the four point probes.

Figure 4.3 shows the change in sheet resistance of the dip coated SnO<sub>2</sub>:Sb samples due to the laser processing. The as-deposited sheet resistance of the samples are denoted by a zero number of pulses.

For all three laser fluences tested, a reduction of sheet resistance was observed with increase of number of laser pulses. The greatest reduction in sheet resistance occurred within the first two laser pulses. The variation of the sheet resistance with respect to the increase of laser fluence was difficult to explain due to variation of the initial sheet resistances within the processing areas. When the laser fluence was at 70 mJ.cm<sup>-2</sup> the films were typically ablated at the higher number of pulses tested (> 10).

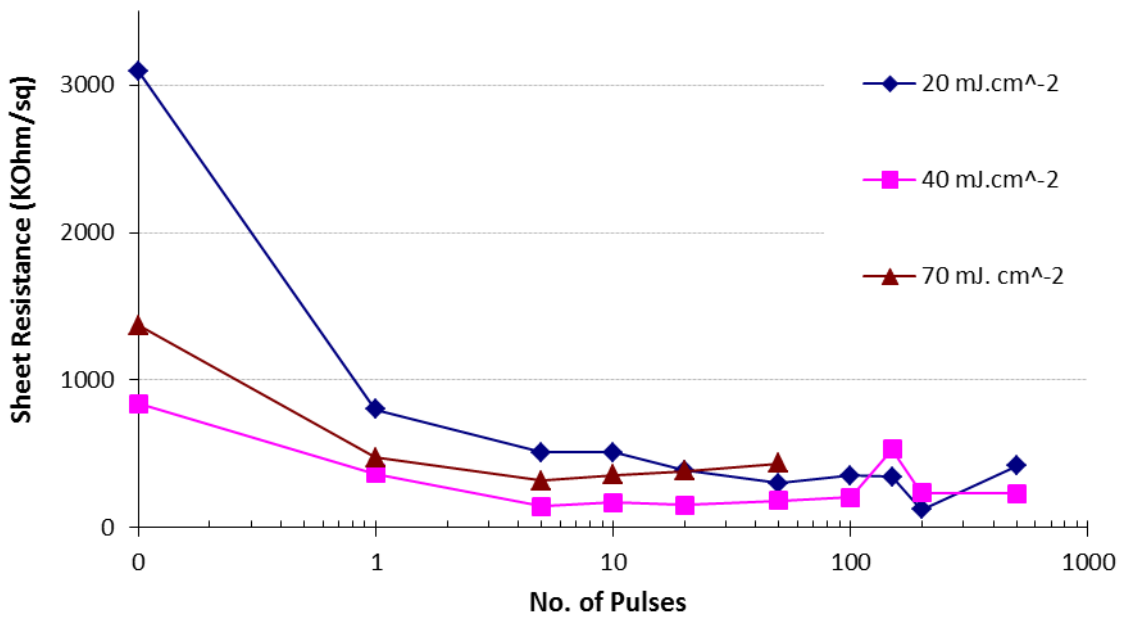


Figure 4.3 : The variation in sheet resistance pre and post laser processing as a function of number of pulses and laser fluence.

The resultant films were further analysed for transmission and microstructure. The crystallinity of the as-deposited and laser processed SnO<sub>2</sub>:Sb films were investigated

using X-ray diffraction using the PANalytical X'Pert PRO diffraction system with CuK $\alpha$ 1 source (wavelength = 1.54056 Å). For the XRD analysis, a dip coated SnO<sub>2</sub>:Sb sample was KrF laser processed with 10, 100, and 1000 pulses at 100 mJ.cm<sup>-2</sup>. The resultant XRD patterns of the as-deposited and KrF laser processed SnO<sub>2</sub>:Sb are shown in figure 4.4, indicating that the films are of polycrystalline nature. The broad main diffraction peaks are attributed to the (110), (101), and (211) peaks of SnO<sub>2</sub> (SnO<sub>2</sub>:Sb ICSD PDF file 01-088-2348) at 26°, 33°, and 51° and corresponds to the tetragonal cassiterite structure. Qualitatively, it can be observed that with the increase of number of laser pulses, the diffraction peaks become sharper. By using the Equation 3.2, the Scherrer equation, the corresponding crystallite size of the as deposited and laser processed material can be estimated.

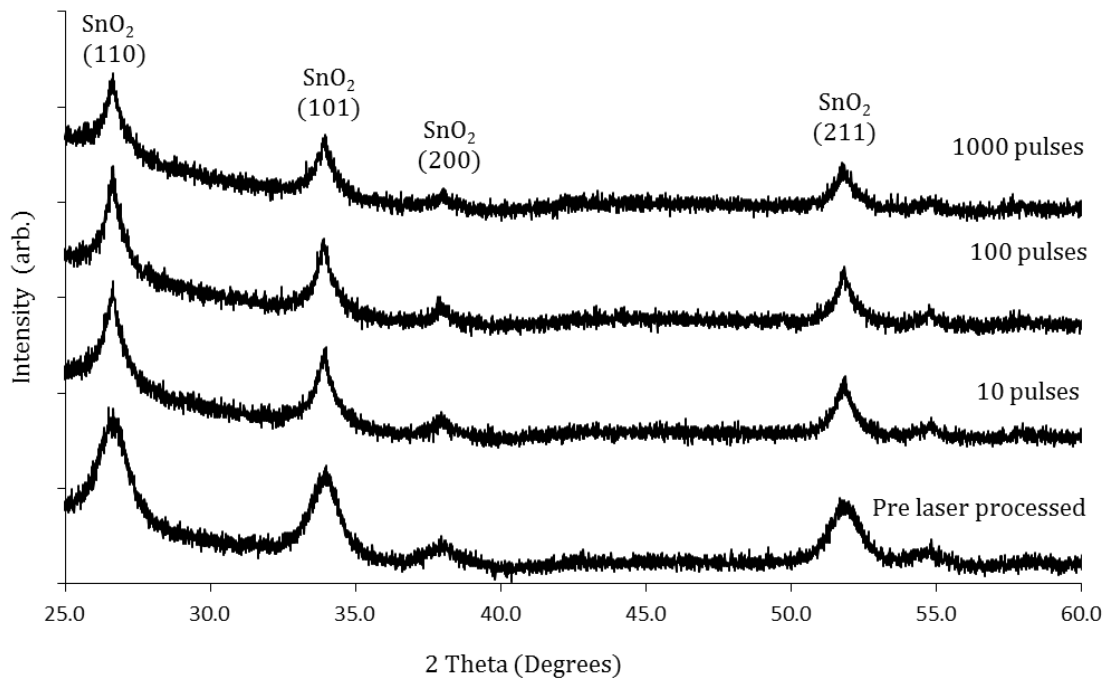


Figure 4.4 : XRD of as-deposited and laser processed dip coated SnO<sub>2</sub>:Sb

Table 4.2 lists the crystallite size (nm) as estimated by the Scherrer equation, with the data from the (110) and (101) diffraction peaks being used in the calculation. It is observed from these results that there is a significant change in the estimated crystalline size as a result of the KrF laser processing, but this change is not clearly correlated to

number of laser pulses, and is more likely to be indicative of an initial change due to the effect of the first few pulses.

Preparation	Orientation	2 Theta (2θ)	FWHM	Grain Size (nm)
As- deposited	110	26.6	1.01	8
	101	33.9	1.10	7
KrF laser processed 10 pulses	110	26.6	0.6	14
	101	33.9	0.5	17
KrF laser processed 100 pulses	110	26.6	0.49	16
	101	33.9	0.64	13
KrF laser processed 1000 pulses	110	26.6	0.55	15
	101	33.9	0.57	15

Table 4.2 : Crystalline size (nm) of SnO<sub>2</sub>:Sb calculated using Scherrer equation.

The Filmetrics spectrometer was used to measure the transmission spectra of the as deposited and laser processed dip coated SnO<sub>2</sub>:Sb samples. Figure 4.5 (a) & (b) show the transmission spectra for dip coated SnO<sub>2</sub>:Sb samples laser processed at 20 mJ.cm<sup>-2</sup> and 40 mJ.cm<sup>-2</sup> respectively. With the exception of the area laser processed at 40 mJ.cm<sup>-2</sup> with 1000 pulses, the transmission at 550 nm of the as-deposited, and laser processed films was > 85%. The transmission of the laser processed at 40 mJ.cm<sup>-2</sup> with 1000 pulses was reduced to 79%. This is consistent with an observed discolouration of the films when processing with higher number of pulses.

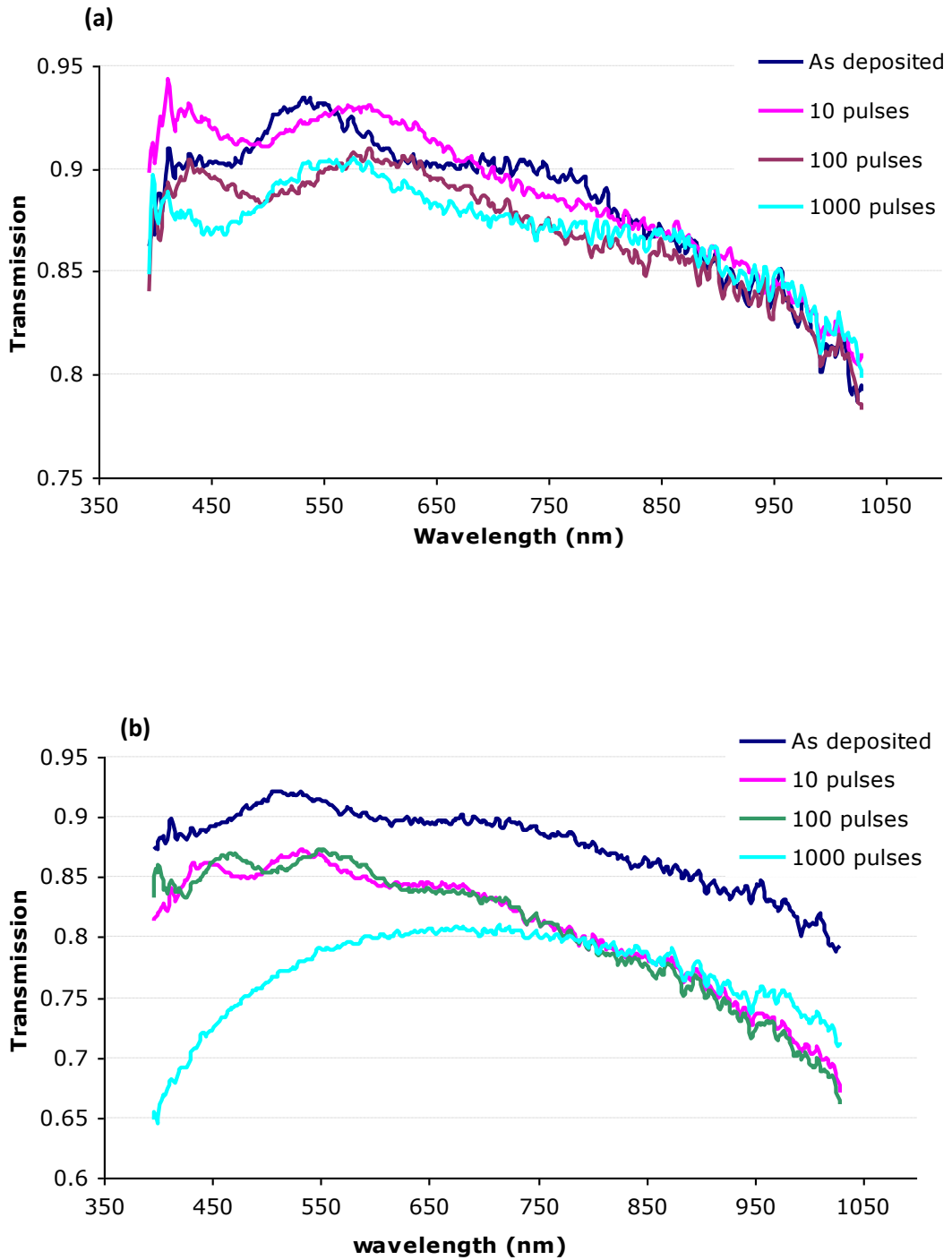


Figure 4.5 : Transmission spectra for dip coated SnO<sub>2</sub>:Sb on glass substrate laser processed with (a) 20 mJ.cm<sup>-2</sup> (b) 40 mJ.cm<sup>-2</sup>.

### 4.3 Inkjet printing of SnO<sub>2</sub>:Sb

Following the initial processing and characterisation of dip coated SnO<sub>2</sub>:Sb samples; the dip coated ink was then formulated to give stable jetting with good wetting characteristics. The ink formulation work was carried out by Sun Chemicals, UK and the samples were inkjet printed at PEL, UK. The author undertook training on the printing equipment with PEL and carried out the sample printing work.

The initial investigation was based around a batch of 40 SnO<sub>2</sub>:Sb samples inkjet printed onto Eagle 2000 glass substrates (25x 25 mm<sup>2</sup>) and photo paper substrates. Sun chemical SnO<sub>2</sub>:Sb ink formulation, U5604 was used to inkjet print these samples. Table 4.3 shows a summary of the sample details. Before inkjet printing, the glass substrates were cleaned and corona treated for ~2 s at 24.5 kV, 20 W. A Xaar 126 drop on demand piezoelectric printer head, with nozzle pitch of 137 μm was used to inkjet print the SnO<sub>2</sub>:Sb samples. The typical firing frequency of these nozzles is 5.2 kHz. All the samples were inkjet printed using micro step of 120 μ and the printing speed was set to 100 mm/s. The droplet height (distance between nozzles to substrate) was set to 1 mm. unless otherwise stated all the inkjet printed samples were printed at room temperature. Figure 4.6 shows examples of inkjet printed SnO<sub>2</sub>:Sb films on glass and photo paper substrates.

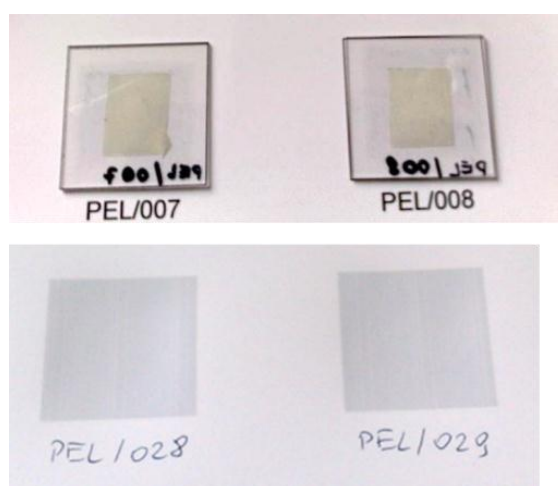


Figure 4.6 : Inkjet printed (3 passes) SnO<sub>2</sub>:Sb onto Eagle XG glass substrate (top) and photo paper (bottom)

Batch A	<b>3 passes on glass substrate</b> Oven dried: ~130 <sup>0</sup> C . ~ 15 min	PEL/001 to PEL/010
Batch B	<b>6 passes on glass substrate</b> Oven dried: ~130 <sup>0</sup> C . ~ 15 min	PEL/011 to PEL/020
Batch C	<b>3 passes on photo paper</b> Oven dried: ~130 <sup>0</sup> C . ~ 15 min	PEL/021 to PEL/030
Batch D	<b>6 passes on photo paper</b> Oven dried: ~130 <sup>0</sup> C . ~ 15 min	PEL/031 to PEL/040

Table 4.3 : Summary of the inkjet printed SnO<sub>2</sub>:Sb samples.

The initial sheet resistance of the inkjet printed SnO<sub>2</sub>:Sb samples were measured using four point probes and the results were shown in figure 4.7. The As-deposited sheet resistance of Batch A were in the range of 4.8 MΩ/sq (± 10%) and Batch B was around 3.6 MΩ/sq (± 5%). In Batch B, some of the inkjet printed layers (PEL/015 – PEL/020) showed no measurable conductivity. These samples also exhibited poor surface quality of the films, due to the `coffee ring` effect which is further discussed in section 4.3.3. The samples which were printed onto photo paper (batch C and Batch D) also showed no measurable conductivity.

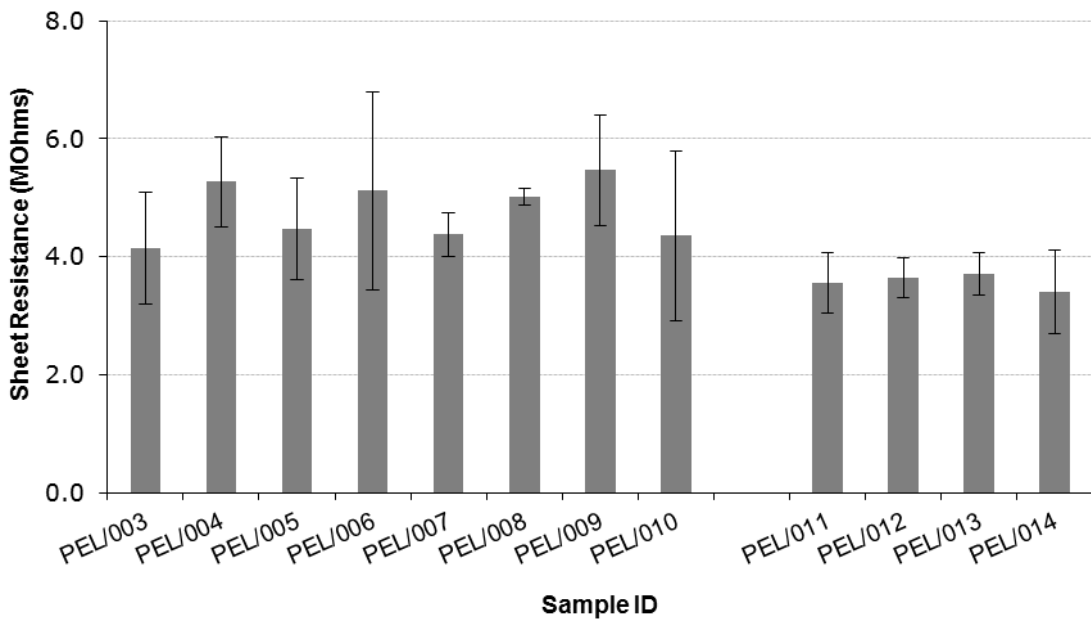


Figure 4.7 : Initial sheet resistance of inkjet printed SnO<sub>2</sub>:Sb on glass substrates.

### 4.3.1 Excimer laser processing of inkjet printed SnO<sub>2</sub>:Sb

The inkjet printed samples were processed using the KrF laser emitting at 248 nm, as described previously. Conductive samples (PEL/004, PEL/008 and PEL/009) from batch A were used for the laser processing experiment. By varying the laser fluence and the number of laser pulses, three areas were processed, with the sheet resistance measured before and after laser processing.

Figure 4.8 shows the observed change in sheet resistance of inkjet printed SnO<sub>2</sub>:Sb due to laser processing (the pre-processed sheet resistances are denoted by zero number of pulses). The results demonstrated that all the samples show a significant reduction in sheet resistance following the first 1 to 2 pulses. There is then a degradation effect at higher pulse numbers, with all the samples showing an increase in sheet resistance at > 10 pulses. For all the laser fluences tested, the minimum sheet resistance measured was between 2 and 8 laser pulses. It was also observed that there was a pin hole effect across the inkjet printed layers, which would affect the minimum sheet resistance. Also, probably linked to these defects, the samples suffered ablation/surface damage following processing at the higher number of pulses.

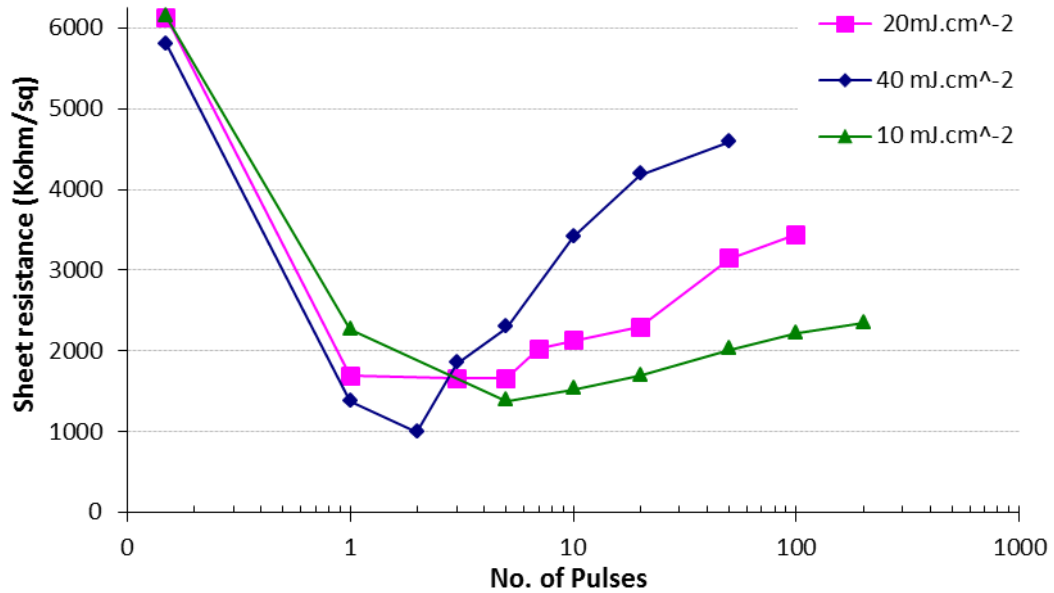


Figure 4.8 : The variation in sheet resistance of inkjet printed SnO<sub>2</sub>:Sb as a function of number of laser pulses and laser fluence.

### 4.3.2 Thermal annealing and laser processing of Inkjet printed SnO<sub>2</sub>:Sb

The premise of the research into laser processing is to examine the effect of low temperature treatments in combination with direct write and solution processing for low cost deposition. Thermal annealing of the solution processed SnO<sub>2</sub>:Sb can produce highly conductive layers with sheet resistance of 300 Ω/sq when processing at 700<sup>0</sup>C , which is far from ideal when considering alternative, flexible, low cost substrates. However, to approach the required values of conductivity required for a particular application, it will be necessary to evaluate the maximum temperature that can be applied vs the conductivity achieved. To add to the processing options, the combination of thermal and laser processing has been investigated for the research presented here. Using the samples printed at PEL, samples from batch B were thermal annealed in air at 500<sup>0</sup>C for 1hr. Before thermal anneal these samples showed no measurable conductivity. Further to the thermal annealing the sheet resistance was measured as 30.6 kΩ/sq (±6.5).

Further to thermal annealing, samples were laser processed with the KrF laser emitting at 248 nm. The laser parameters varied for this experiment were laser fluence and number of laser pulses. Figure 4.9 shows the resultant change in sheet resistance of thermal annealed SnO<sub>2</sub>:Sb samples due to the subsequent laser processing (a zero number of pulses represents the post thermal annealed sheet resistance of the processed area).

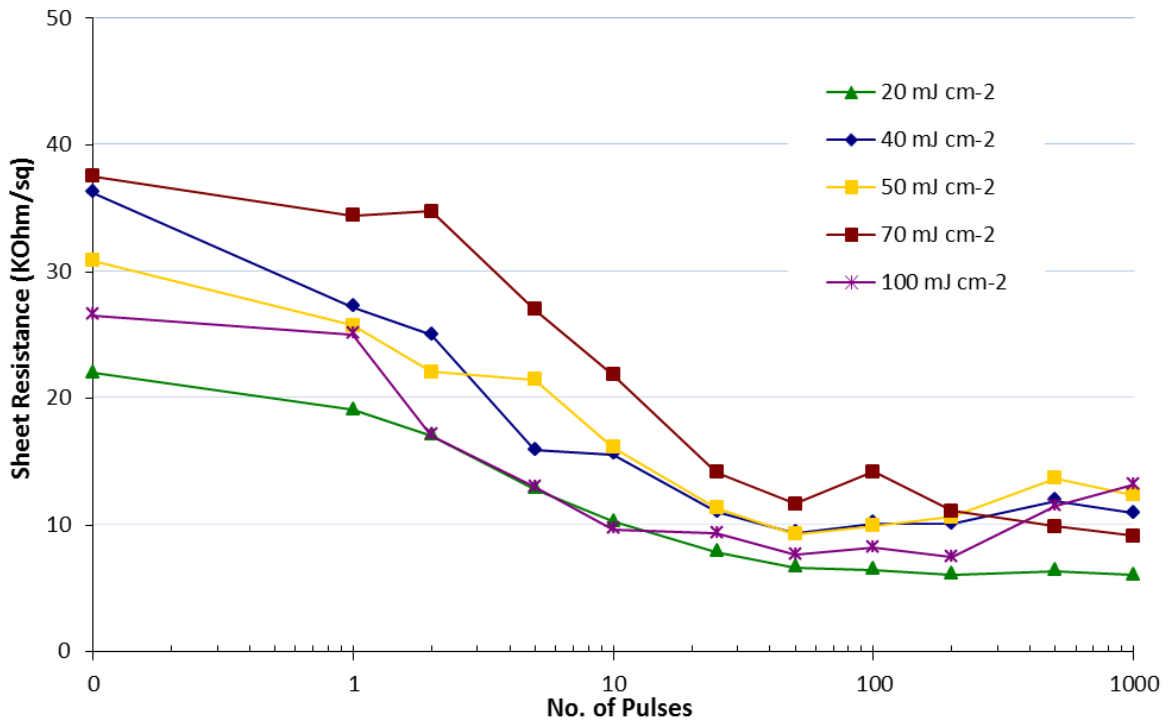


Figure 4.9 : The variation of sheet resistance post laser processing as a function of number of laser pulses and laser fluence for thermal annealed SnO<sub>2</sub>:Sb.

The results demonstrate some reduction of sheet resistance with respect to the number of laser pulses used. However, it is clear that these results have not demonstrated a greater reduction within first few laser pulses as with the oven dried samples (figure 4.8). This may suggest that during this process the ink residuals were removed with the thermal annealing while the excimer laser processing helps to reduce the grain scatterings and hence the subsequent reduction of sheet resistance.

### **4.3.3 Coffee ring effect**

All the samples which are inkjet printed onto the glass substrate exhibited some degree of the coffee ring effect, or coffee staining effect, which is a build-up of particulates at the edges of the drying drop, due to capillary flow induced by the differential evaporation dynamic flows across the droplet. This problem has been intensively studied during the last decade, especially in relation to the use of functional inks [102-104]. Deegan et al [105] described the coffee stain effect as a result of uneven evaporation of liquid over a droplet's liquid air interface, since the edge of the droplet is the preferred location for the evaporation. Perelaer et al [106] studied in-flight evaporation of ink solvents by varying the printing height which also leads to control the droplet diameter. Other authors including Soltman et al [103] also investigated the substrate temperature beneath the layer, drop spacing, and drop frequency and these were leads to reversing or enhancement of the coffee ring effect.

Therefore, for this research, some investigation was undertaken to eliminate or minimise the coffee stain effect on inkjet printed SnO<sub>2</sub>:Sb samples on glass substrates. These tests were conducted with a fresh set of SnO<sub>2</sub>:Sb ink. SnO<sub>2</sub>:Sb ink, U6404 which was formulated by Sun chemicals Ltd and subsequently inkjet printed. However, this new set of ink showed significant difference in the flow characteristics as compared to the previous samples and rapidly wetted the substrate rather than forming the image required, hence, some effort was also required to address this.

#### **4.3.3.1 Damming structures**

In order to control the rapid wetting on the substrate, a physical damming structure technique was investigated. In this technique the outer border of the required image is initially defined via inkjet printing of an organic ink. The 'dam' structure is then filled with the ink to print the required image. Further to deposition of the required image, the outer border can either be left or removed via a thermal process. This technique has advantages in the production of multi-layered electronic structures. For the SnO<sub>2</sub>:Sb

samples studied, the 2 mm border was used to produce a dam perimeter for the SnO<sub>2</sub>:Sb sample area which was initially inkjet printed using three colour UV curable ink. During the UV ink printing the temperature of the ink was held at 55<sup>0</sup>C using the associated water controlling system. After the printing, the border was UV cured for few minutes. Then, by varying the number of inkjet passes, SnO<sub>2</sub>:Sb samples were inkjet printed on to these structures and oven dried at 100<sup>0</sup>C for 15 mins. Figure 4.10 shows the SnO<sub>2</sub>:Sb ink filling to the structures with respect to the different number of passes.

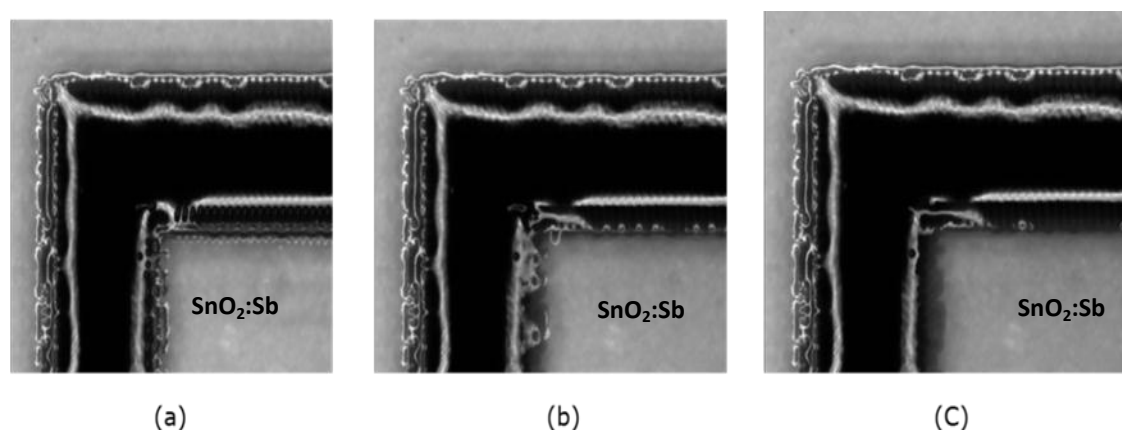


Figure 4.10 : SnO<sub>2</sub>:Sb layers building up with in the UV wall for (a) 1 inkjet pass (b) 3 inkjet passes and (c) 6 inkjet passes

Following the oven drying process at 100<sup>0</sup>C for 15 mins all the inkjet printed samples with 3 and 6 passes showed the coffee stain effect. Therefore this technique was useful in localising the spread of the ink following printing, but was still subject to the coffee staining effect.

#### 4.3.3.2 Drying conditions

Previous work by Morii et al [107, 108] showed that the drying process of inkjet printed droplets is crucial for making good uniform thin films due to the droplet size. Inkjet printed droplets have higher surface to volume ratio compared to their micro sized counterparts and exhibit higher evaporation rate. The drying process is mainly related to

the vapour pressure of the solvent, which is related to the evaporation rate. Therefore it is very important to optimise the drying conditions to obtain uniform inkjet printed layers.

Different drying conditions (drying temperature and environment) were studied for the inkjet printed SnO<sub>2</sub>:Sb layers, with the aim to produce uniform, coffee stain free, layers. Initially, a set of four SnO<sub>2</sub>:Sb samples was inkjet printed with a 2 x 2 array of 1.5cm x 1.5 cm printed areas. (Unless otherwise mentioned, all these samples were wet on wet printed and no drying was carried out between layers). Following the deposition, two of these samples were oven dried at different temperatures to study the drying effect. Figure 4.11 shows the inkjet printed layers which are dried at 120<sup>0</sup>C and 80<sup>0</sup>C for 1 hr to remove the ink residuals.

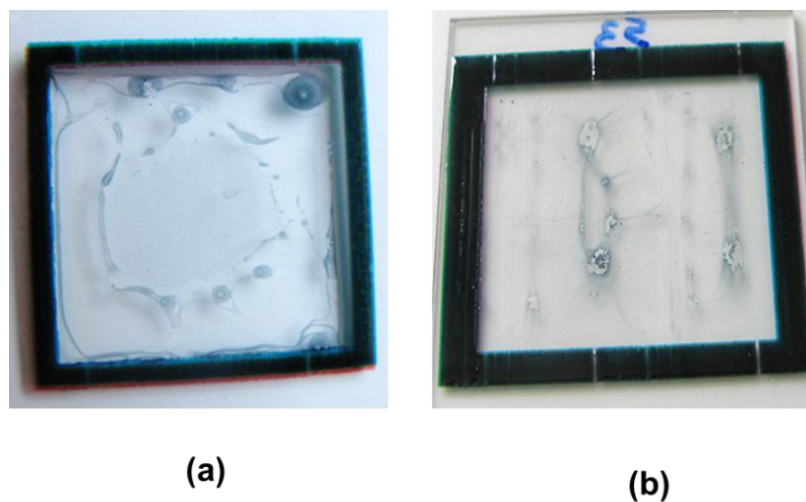


Figure 4.11: Inkjet printed SnO<sub>2</sub>:Sb: Oven dried at different temperatures (a) 120<sup>0</sup>C (b) 80<sup>0</sup>C

Samples which are oven dried at 120<sup>0</sup>C showed a more significant occurrence of the coffee stain effect and some degree of the Marangoni effect; in this effect the ink has segregated to the edge and the centre of the inkjet printed area. This phenomenon was not seen in the sample which is oven dried at 80<sup>0</sup>C but the coffee stains were still present.

The other two samples were oven dried in vacuum and air respectively to understand the drying environment effect on droplet evaporation. Both samples have been dried at 80<sup>0</sup>C for ~1 hr. Figure 4.12 shows the inkjet printed SnO<sub>2</sub>:Sb layers which are dried in air and vacuum. The sample that has been vacuum dried at 80<sup>0</sup>C shows a more uniform layer than the air dried sample, but both samples show the Marangoni effect, particularly with the air dried sample.

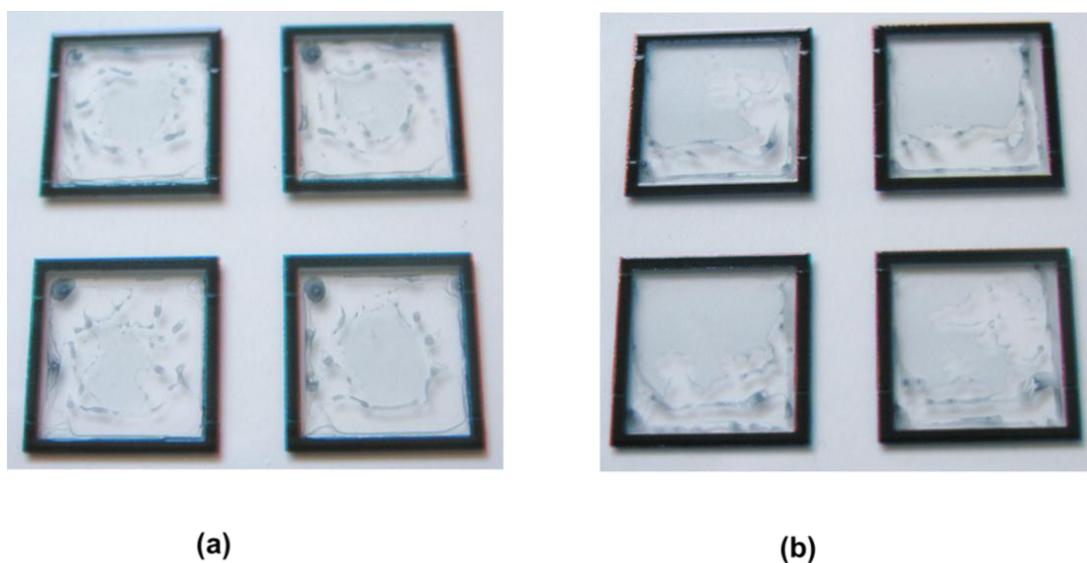


Figure 4.12 : Inkjet printed SnO<sub>2</sub>:Sb: oven dried at 80<sup>0</sup>C for 1 hr (a) in air (b) in vacuum

Following these results, a few more samples were inkjet printed onto soda lime glass substrates to understand the substrate dependency to the coffee stain and Marangoni effect. The samples which are deposited onto soda lime substrate without surface modification shows no considerable Marangoni effect, but the coffee stains are present. Therefore the Marangoni effect could be explained as a localised problem associated with that specific glass batch.

#### 4.4 Summary and Discussion

Via collaboration, SnO<sub>2</sub>:Sb ink was formulated and thin films were deposited onto glass substrates using a dip coating technique. The average thickness of the dip coated layers was around 950 nm and the as-deposited sheet resistance was in the MΩ range. Further to excimer laser processing, a reduction of sheet resistance was obtained for all the laser fluences and number of laser pulses investigated, and XRD analysis indicated an increase in crystallite size for excimer laser processed layers.

Further to the dip coating work, the SnO<sub>2</sub>:Sb ink was inkjet printed onto glass and photo paper substrates. The as-deposited inkjet printed films showed higher sheet resistance compared to the dip coated films. Even though inkjet printing is capable of producing droplets with a consistent volume [109] in well define patterns, the application of ink solutions strongly depends on ink formulation, choice of printer equipment, substrate used and the rate of solvent evaporation versus marangoni-flow. During this study the printer settings, substrates and the drying conditions were studied to inkjet print SnO<sub>2</sub>:Sb onto glass substrate with minimal coffee stain effect and marangoni flow. However the study was not concluded and it was not possible to deposit consistent inkjet printed SnO<sub>2</sub>:Sb layers with good uniformity and minimal coffee staining effect. Also during this work some difficulties were encountered in terms of formulating new batches of SnO<sub>2</sub>:Sb ink which were consistent with previous batches, and which would hence allow for further comparative experimentation.

Considering the difficulties encountered with the use of inkjet printing as a mechanism to produce experimental samples, the decision was made to move to the use of spin coating in order to more thoroughly investigate the effect of post deposition processing. Spin coating is an inexpensive, reliable and conformal technique to deposit solution based inks onto planar substrates. This technique typically does not require specialised ink formulation to produce uniform and repeatable coatings. For the next stage of the research, therefore, aqueous dispersions of SnO<sub>2</sub>:Sb were prepared by K&W as a basic ink to spin-coat SnO<sub>2</sub>:Sb samples. The ink was formulated by diluting the colloidal dispersion in water to drop the solids to 10 to 15 % and by adding a small amount of wetting agent to aid substrate wetting. This ink shows very low viscosity of 1 to 2 cP,

but produces uniform and reliable thin films which were used for the remainder of the project.

Chapter 5 presents the details of functionalization and characterisation of spin coated SnO<sub>2</sub>:Sb films.

## **5. Post processing of spin coated SnO<sub>2</sub>:Sb**

### **5.1 Introduction**

Direct write techniques such as inkjet printing have attracted attention as promising material deposition techniques to deposit solution based materials onto various substrates due to the efficient material usage, cost efficient process and precise high resolution patterning capability [8, 85]. However, there is always the associated challenge to develop nanoparticulate inks with good wetting and jetting properties to deposit materials.

As explained in Chapter 4, during the FAB3D project several batches of SnO<sub>2</sub>:Sb dispersions were prepared by Keeling and Walker Ltd, with the ink formulated by Sun Chemicals for inkjet printing trials. This nanoparticulate SnO<sub>2</sub>:Sb ink had very low viscosity for inkjet printing. Therefore this problem has been investigated by the project collaborators by adding viscosity modifiers such as polymer additives and gums without detriment to conductivity or transparency. In most of the trials the addition of such modifiers was effective at increasing the viscosity, but was incompatible with the SnO<sub>2</sub>:Sb dispersion, leading to haze in the resultant coatings. Therefore as a solution, a low viscosity compatible sol-gel based deposition technique was investigated to deposit the SnO<sub>2</sub>:Sb ink on to glass substrates.

The spin coating technique is a well-documented method to apply nanoparticulate SnO<sub>2</sub>:Sb ink onto flat substrates [37, 110, 111]. This technique allows fast and simple production of highly uniform films of controllable and reproducible thickness extending over large surface areas depending on the size of the spin coater. Hence, the spin coating technique has been used as a deposition technique to deposit the SnO<sub>2</sub>:Sb ink onto glass substrates for this project. This has provided a consistent source of samples to allow for a more systematic study of the effect of post deposition processing parameters.

This chapter explains the post processing techniques used to optimise the electrical and optical properties of spin coated SnO<sub>2</sub>:Sb. This includes thickness optimisation of the as-deposited SnO<sub>2</sub>:Sb, post deposition excimer laser processing, thermal annealing and the combined processing of SnO<sub>2</sub>:Sb.

## **5.2 Thickness optimisation of as- deposit SnO<sub>2</sub>:Sb layers**

Different thickness SnO<sub>2</sub>:Sb samples were prepared by varying the number of spin coated layers to optimise the electrical and optical characteristics. The initial batch consisted of 20 spin coated SnO<sub>2</sub>:Sb samples with four of each different thickness SnO<sub>2</sub>:Sb films on 5x5 cm<sup>2</sup>, Eagle XG glass substrates. The number of SnO<sub>2</sub>:Sb layers were varied between four and fourteen. Unless otherwise mentioned, the higher number of layers were built up by repeating the application of ink and spinning, following an air dry between the successive layers. Further to deposition, the samples were oven dried at 100<sup>o</sup>C to remove ink residuals. The sheet resistance of each sample was then measured using four point probes and the optical transmission was characterised. Crystallisation of the as-deposited layers was investigated using XRD.

### **5.2.1 Sheet Resistance**

Figure 5.1 shows the sheet resistance variation of the as-deposited films with respect to the number of spin layers. For this study 4, 6, 8, 10 and 12 layer SnO<sub>2</sub>:Sb films were considered.

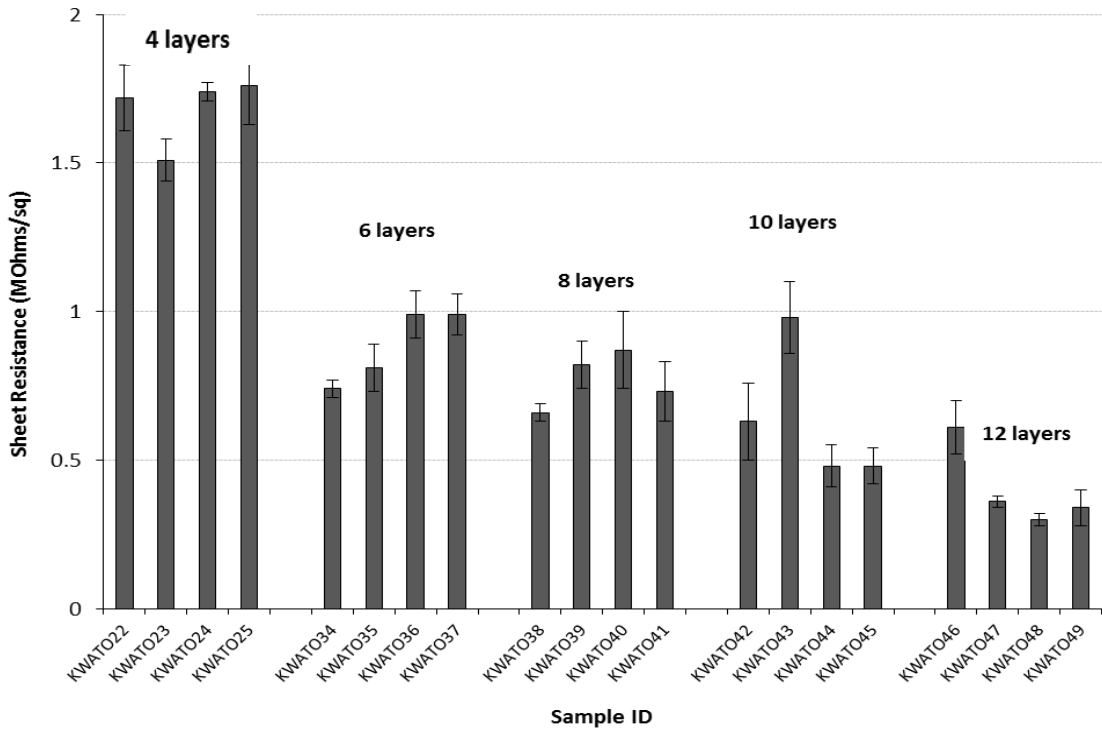


Figure 5.1 : Sheet resistance variation between batches of different thickness SnO<sub>2</sub>:Sb

A significant variation in sheet resistance has been measured between different thickness SnO<sub>2</sub>:Sb batches. By varying the number of layers, the average sheet resistance can be varied between 1.7 MΩ/sq and 0.4 MΩ/sq. Also, some variation in sheet resistance was observed within the same set. This was  $< \pm 15\%$  of the average value. Furthermore, a visual inspection of the spin coated samples gives some evidence of a slightly darker area the middle compared to the outer area which may be because of some thickness variations across the sample. Figure 5.2 shows photographs of different thickness spin coated SnO<sub>2</sub>:Sb layers

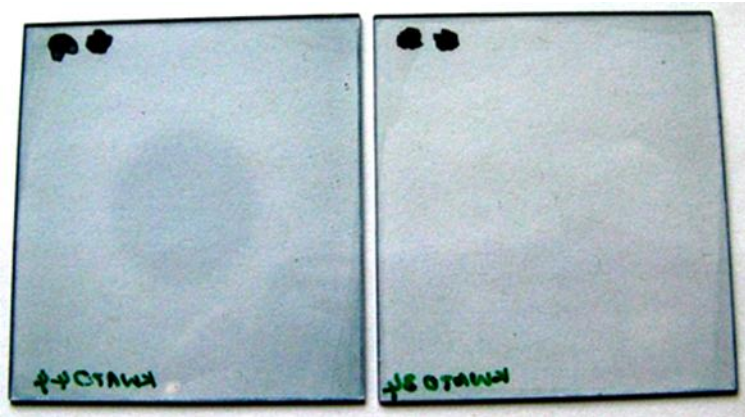


Figure 5.2: Spin coated SnO<sub>2</sub>:Sb layers on Eagle XG glass substrate : left-12 spun layers right- 6 spun layers.

### 5.2.2 Film thickness

Film thicknesses of the as-deposited SnO<sub>2</sub>:Sb layers on Eagle XG glass substrate were measured using Dektak 6M Stylus Profilometer. Initially five samples have been selected by taking one sample from each set of different layers number for the measurement. Prior to measurement, a 5x5 mm<sup>2</sup> area was laser ablated on each sample to make a suitable physical edge for the thickness measurement. The KrF excimer laser was used to ablate the SnO<sub>2</sub>:Sb layer. Typically 15 to 20 laser pulses were used at 100 mJ/cm<sup>2</sup> to produce a suitable edge. Figure 5.3 shows the measured average thickness of SnO<sub>2</sub>:Sb layers with respect to the number of spun layers. For each set, at least three measurements were taken and the average value was recorded as the film thickness. These measured film thicknesses were in good agreement with the thicknesses obtained during TEM analysis which is discussed in chapter 6.

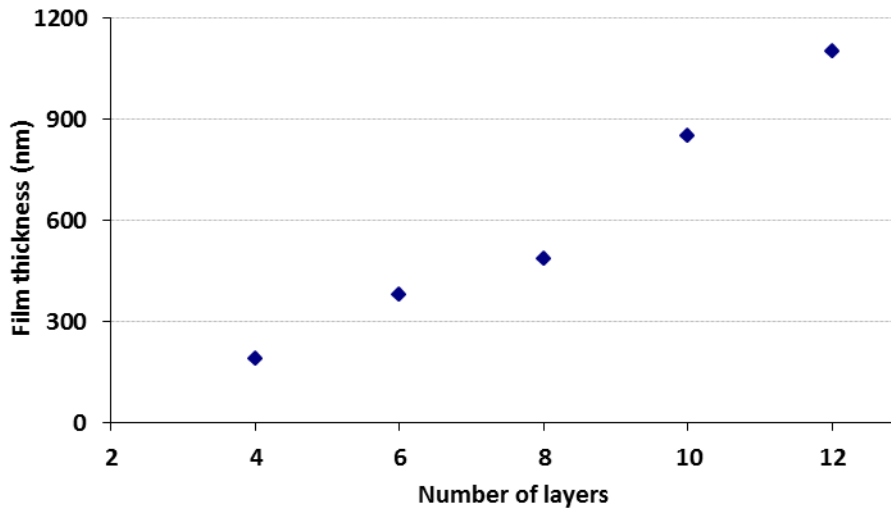


Figure 5.3 : Measured film thickness of as- deposited SnO<sub>2</sub>:Sb vs number of spun layers

### 5.2.3 Transmission

Optical transmission measurements in the visible range of the as-deposited layers are illustrated in figure 5.4. The transparency of the as-deposited layers steadily decreases as the film thickness increases. The low thickness films show better transparency across the full measured range with the highest transmission of 95% at 550 nm. When the film thickness increases from 0.3 μm to 1.1 μm, the transmission at 550 nm was decreased from 95% to 87%. In the near infra-red region (IR) the absorption is intense for thicker layers, since the free electrons contribute to the absorption of the IR radiation. (During the measurements the substrate effect was removed and only SnO<sub>2</sub>:Sb transmission was considered, as explained in section 3.4.1).

Figure 5.5 shows the combined sheet resistance and optical transmission at 550 nm variation of as-deposited SnO<sub>2</sub>:Sb layers with respect to the film thicknesses. It shows that with respect to the increase film thickness, the sheet resistance and optical transmission are both decreased.

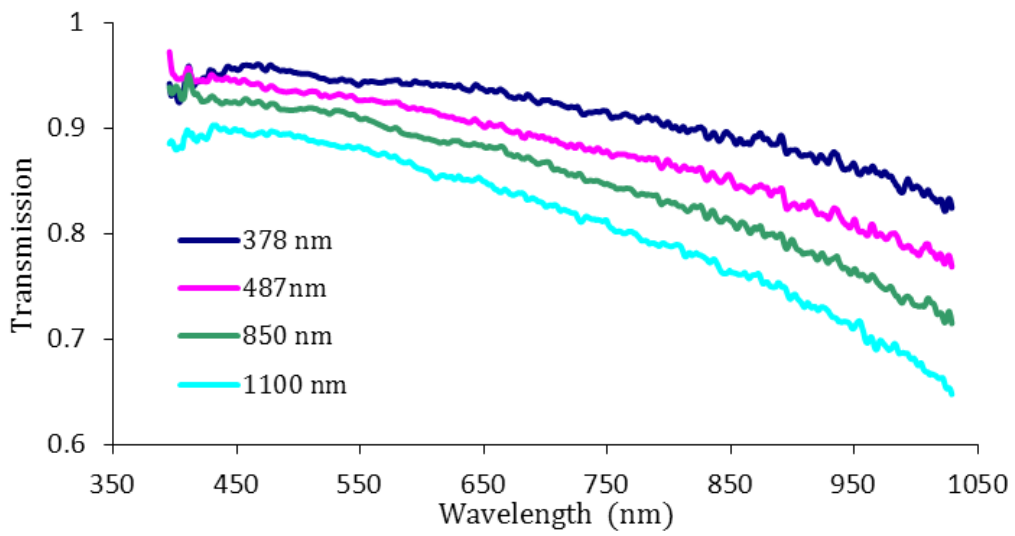


Figure 5.4 : Transmission variation with respect to the film thickness of the as-deposited SnO<sub>2</sub>:Sb

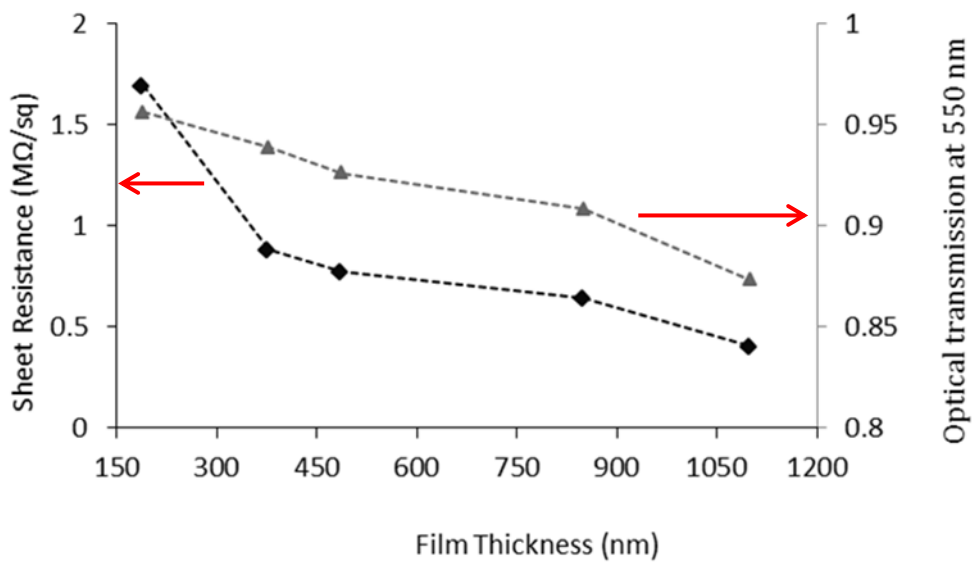


Figure 5.5 : Sheet resistance and optical transmission at 550 nm variation with respect to film thickness of as-deposited SnO<sub>2</sub>:Sb

With an average sheet resistance of 400 kΩ/sq and the optical transmission in the visible region of 87%, the 12 layer as-deposited SnO<sub>2</sub>:Sb films with a thickness of 1100 nm were selected as the optimised thickness to investigate for post processing trials.

### 5.2.4 XRD

The crystallinity and the structural characteristics of the as-deposited SnO<sub>2</sub>:Sb films were characterised by X-ray diffraction. A Philips PANalytical X'Pert Pro system with monochromated CuK $\alpha$ 1 radiation source,  $\lambda = 1.54056 \text{ \AA}$  was used for this characterisation. The diffractograms of the different thickness layers are shown in figure 5.6.

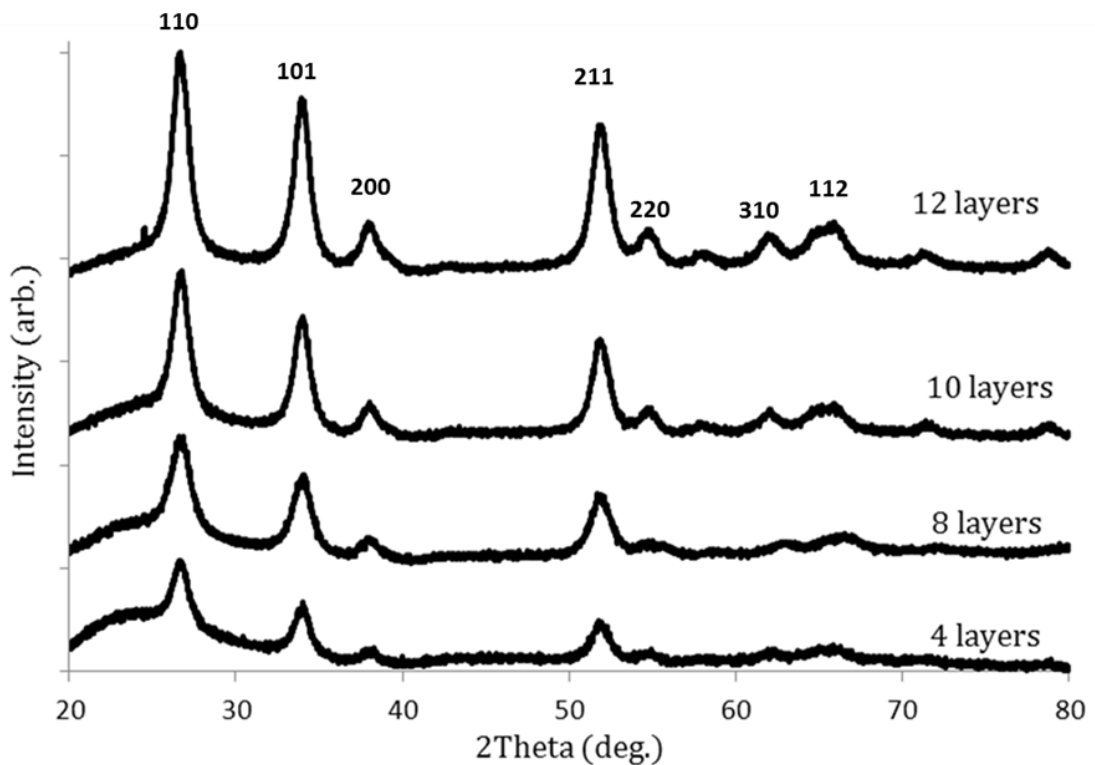


Figure 5.6 : XRD patterns of as-deposited spin coated SnO<sub>2</sub>:Sb layers

The Miller indices,  $hkl$ , corresponding to the XRD peak positions were assigned based on the SnO<sub>2</sub>:Sb, ICSD PDF file 01-088-2348. The results show the presence of diffraction peaks corresponding to the (110), (101), (200), and (211) planes of SnO<sub>2</sub> at 26°, 33°, 37°, 51° respectively. These diffraction peaks are predominantly attributed to the tetragonal cassiterite structure. The intensity of the XRD peaks increases with the increase number of ATO layers: i.e. layer thickness. Some peak broadening was also

observed as sample thickness increases. No evidence of peak position shift was observed due to number of SnO<sub>2</sub>:Sb layers. The SnO<sub>2</sub> (310) and (301) phases are more prominent with the higher number of SnO<sub>2</sub>:Sb layers.

The crystalline sizes of as-deposited layers were calculated by using the Scherrer formula (Equation 3.2). Table 5.1 summaries the Full width at Half Maximum (FWHM) and crystalline sizes corresponding to the SnO<sub>2</sub>:Sb XRD peaks of the as-deposited layers.

Number of spun layers	<i>h k l</i>	2 theta	FWHM	Crystallise size (nm)
4	110	26.6	1.13	7
	101	33.9	1.00	8
	211	51.8	1.10	8
8	110	26.6	1.13	7
	101	33.9	1.00	8
	211	51.9	1.17	7
10	110	26.6	1.08	7
	101	33.9	1.03	8
	211	51.9	1.17	7
12	110	26.7	1.10	7
	101	33.9	1.08	8
	211	51.9	1.10	8

Table 5.1 : Summary of XRD findings- As deposited spin coated SnO<sub>2</sub>:Sb

The XRD peaks corresponding to (110), (101) and (211) were used to calculate the crystalline sizes. There was no crystalline size variation evident for the range of SnO<sub>2</sub>:Sb samples investigated. This suggests that by adding extra layers to increase the film thickness, there is no direct effect on the grain sizes or film crystallinity.

### **5.3 Thermal annealing of the spin coated SnO<sub>2</sub>:Sb**

Thermal annealing is a well-defined post processing technique for crystalline thin films. Throughout this work, Heraeus D-6450 Hanau convection oven was used to thermal annealing at less than 400<sup>0</sup>C .A Carbolite CWF1200 furnace was used for the higher temperature annealing at 700<sup>0</sup>C . Samples with 12-spun layers were used to study the effect of thermal annealing on SnO<sub>2</sub>:Sb layers. Each 5x5 cm<sup>2</sup> sample area was cut into quarters and used for the experimentation. These samples were thermal annealed at 100<sup>0</sup>C , 200<sup>0</sup>C , 300<sup>0</sup>C , 400<sup>0</sup>C and 700<sup>0</sup>C respectively. After thermal annealing, these films were investigated for sheet resistance, transmission and crystallinity.

#### **5.3.1 Sheet resistance**

The sheet resistance variation of the thermal annealed SnO<sub>2</sub>:Sb layers with respect to the annealing temperature is shown in figure 5.7. The sheet resistance dramatically decreases with the increase of annealing temperature. The zero temperature represents the average as-deposited sheet resistance of the all six sample areas used for this experimentation. The as-deposited sheet resistance of these areas was around 700 kΩ/sq and further to thermal annealing at 700<sup>0</sup>C the lowest sheet resistance of 120 Ω/sq was achieved. When thermally annealed at 400<sup>0</sup>C, the sheet resistance was reduced to 1 kΩ/sq.

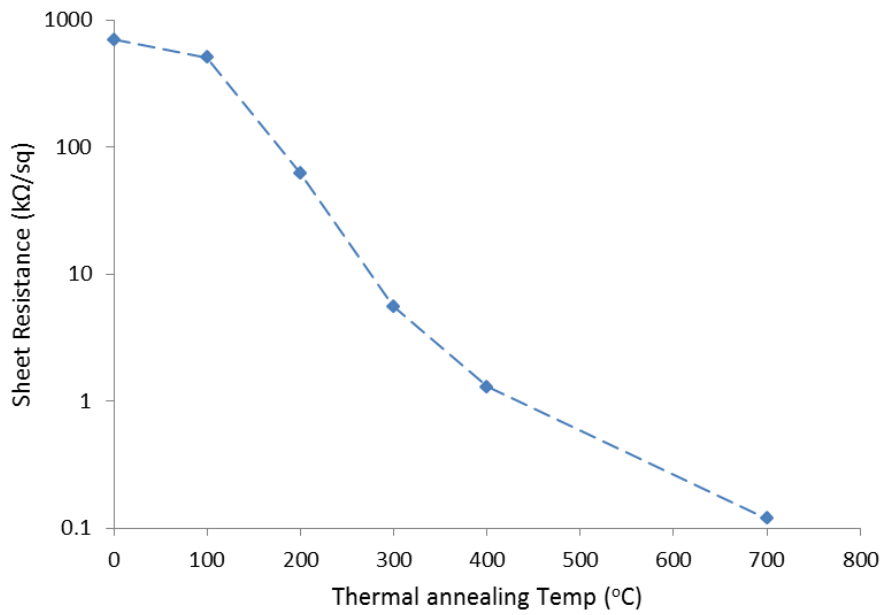


Figure 5.7 : Sheet resistance variation of the spin coated SnO<sub>2</sub>:Sb layers with thermal anneal temperature.

### 5.3.2 Transmission

The transmission spectra of the thermal annealed layers, along with the as-deposited layer are shown in figure 5.8. All the post processed films show lower transparency than the as-deposited film across the spectrum. Films that have been thermal annealed at temperatures 400<sup>0</sup>C or less show a steady reduction of transparency across the spectrum with the increase of thermal annealed temperature. However, the sample which has been thermal annealed at 700<sup>0</sup>C shows higher transparency across the spectrum than the 300<sup>0</sup>C and 400<sup>0</sup>C thermal annealed samples. This may be related to a reduction of film thickness with higher temperature annealing, but it was difficult to confirm this because the films become more resistant to laser ablation following thermal annealing, which makes it difficult to produce an effective edge for measurement. At 550 nm, the transmission for as-deposited, thermal annealed at 100<sup>0</sup>C , 200<sup>0</sup>C , 400<sup>0</sup>C , and 700<sup>0</sup>C were 84%, 82%, 80%, 79% and 82%, respectively.

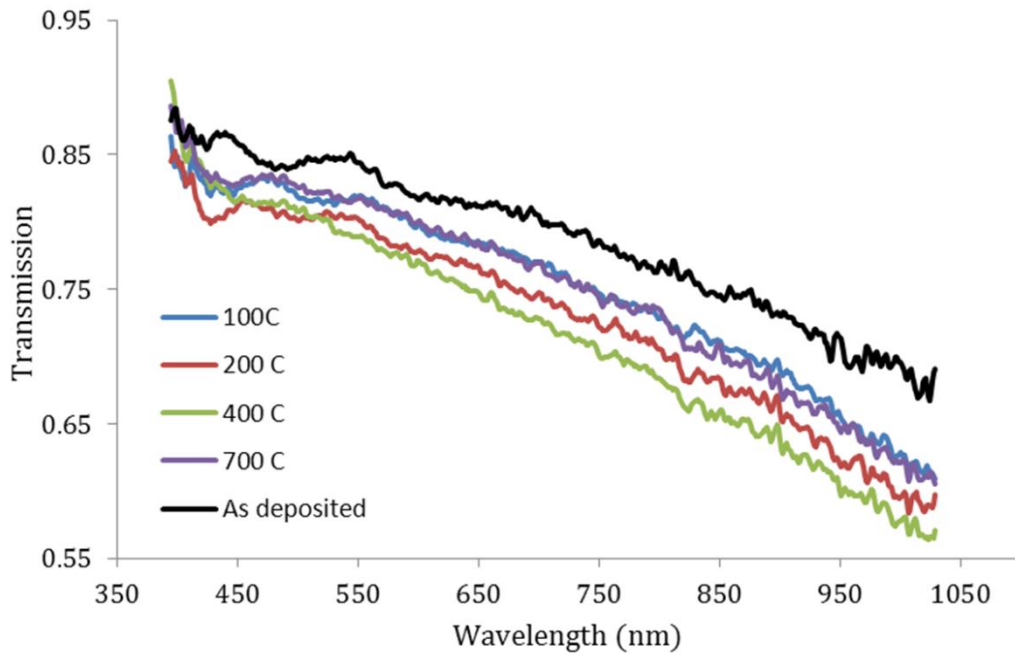


Figure 5.8 : Transmission spectra of the thermal annealed SnO<sub>2</sub>:Sb layers

### 5.3.3 XRD

Further to the sheet resistance and transmission measurements, the crystallisation of thermal annealed films was examined. The resultant XRD patterns of the thermal annealed SnO<sub>2</sub>:Sb layers are shown in figure 5.9.

The results show the presence of (110), (101), (200) and (211) orientation of SnO<sub>2</sub> which produce XRD peaks at 26°, 33°, 37°, 51° respectively. As explained in section 5.2.4, the SnO<sub>2</sub>:Sb PDF file ICSD PDF file 01-088-2348 was used to identify the peaks. Further to thermal annealing at lower temperatures (<400°C), there is no obvious evidence of peak height increase observed. However, some increment was observed for the samples annealed at 700°C. The diffraction peaks in the XRD patterns of thermal annealed SnO<sub>2</sub>:Sb layers were used to calculate the corresponding crystalline sizes by using Scherrer's equation (Equation 3.2).

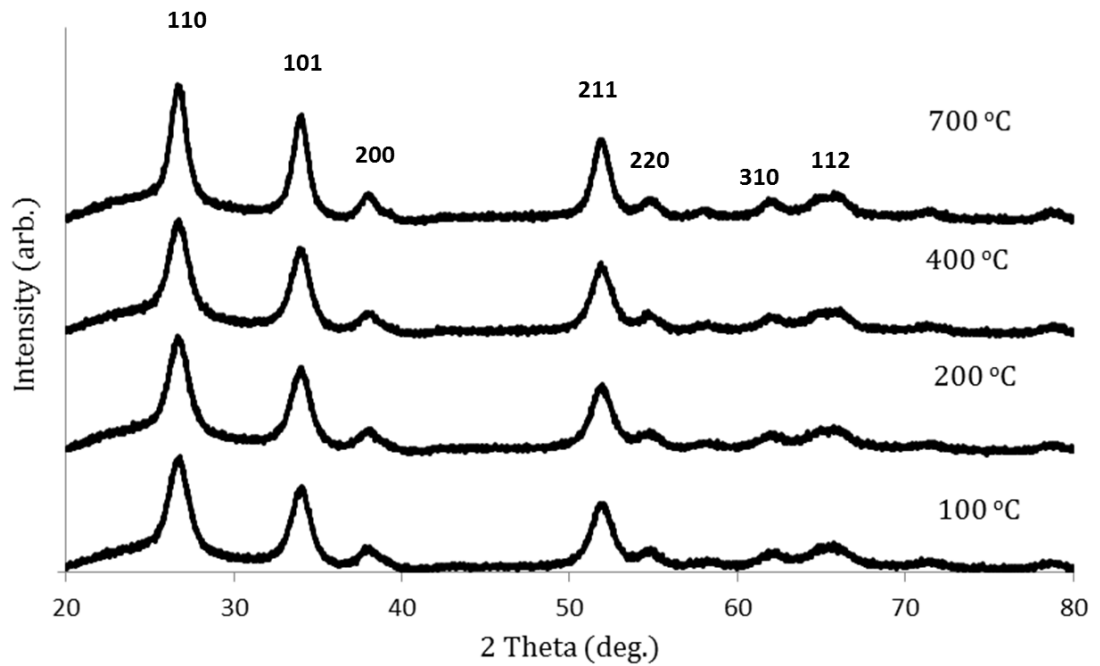


Figure 5.9 : XRD patterns of thermal annealed SnO<sub>2</sub>:Sb layers

Table 5.2 shows the average crystalline size calculations for the three main diffraction peaks of the (110), (101) and (211) planes with the varying thermal annealing temperature. For the thermal anneal temperatures of 100<sup>0</sup>C, 200<sup>0</sup>C and 400<sup>0</sup>C, the average crystalline size did not vary and remains around 6-7 nm similar to the case with the as-deposited layers. Some grain growth was only observed when samples thermal annealed at 700<sup>0</sup>C , where the crystalline size increased to 9 nm.

Thermal annealing temperature °C	<i>h k l</i>	2 theta	FWHM	Crystallise size (nm)
100	110	26.6	1.29	6
	101	33.9	1.27	6
	211	51.9	1.40	6
200	110	26.6	1.11	7
	101	33.9	1.20	7
	211	51.8	1.29	7
400	110	26.6	1.28	6
	101	33.9	1.23	7
	211	51.8	1.33	7
700	110	26.7	0.95	9
	101	33.9	0.96	9
	211	51.8	1.00	9

Table 5.2 : Summary of XRD findings: Spin coated SnO<sub>2</sub>:Sb –Thermal annealed at 100°C , 200°C , 400°C and 700°C .

#### 5.4 Excimer laser processing of spin coated SnO<sub>2</sub>:Sb layers

The in-house Lambda Physik LPX305i excimer laser system was used to laser process the spin coated SnO<sub>2</sub>:Sb layers. By changing the lasing gases this system was used for both KrF laser processing (operating at 248 nm) and ArF laser processing (operating at 193 nm). When operating at 248 nm, a beam homogeniser and a beam attenuator were used to create uniform required beam profile at the sample stage. By varying the beam attenuator, the energy per pulse is controlled to obtain the required energy density at the sample stage. When operating at 193 nm, a set of HOYA plates (fused silica) were used to control the energy density delivered to the sample.

In order to understand the effect of excimer laser processing on spin coated SnO<sub>2</sub>:Sb layers, several samples were laser processed. For both wavelengths used, a 1 cm x 1 cm beam geometry was employed and Eagle XG glass was used as the substrate. The 12-layer spin coated samples were laser processed with both 248 nm, and 193 nm lasers. ( A series of 4-layer samples were also processed with 248 nm laser).

Each SnO<sub>2</sub>:Sb sample was divided in to four areas and processed at four different fluences. Due to the limited number of samples, the higher number of laser pluses were achieved by considering the cumulative number of pulses.

#### **5.4.1 KrF laser processing of different thickness spin coated SnO<sub>2</sub>:Sb**

By varying the number of laser pulses and laser fluences, SnO<sub>2</sub>:Sb layers were KrF laser processed in air at atmospheric conditions. The laser fluence was varied between 20 and 80 mJ/cm<sup>2</sup>, while the number of pulses was varied from 1 to 1000. For all processing conditions the laser repetition rate was kept less than 5 Hz. further to laser processing the films were characterised for sheet resistance, optical transparency, and crystallinity.

##### **5.4.1.1 Sheet resistance**

The sheet resistance of the post laser processed areas were measured using the four point probes. Figures 5.10 and 5.11 shows the sheet resistance variation of post laser processed SnO<sub>2</sub>:Sb layers with respect to the number of laser pulses and laser fluences for 1100 nm and 190 nm film thicknesses respectively.

For both SnO<sub>2</sub>:Sb thicknesses, the sheet resistance of the processed areas were reduced with the increase of laser pulses. The sheet resistance of the films with 1100 nm thickness dramatically reduced with the first ten laser pulses for all the fluences and then continuously decreases, but with little effect due to the subsequent pulses. The initial sheet resistance of these films was around 400 kΩ/sq and further to KrF laser

processing, the lowest sheet resistance of around 15 kΩ/sq was obtained when processing with 60 mJ.cm<sup>-2</sup> and around 1000 pulses.

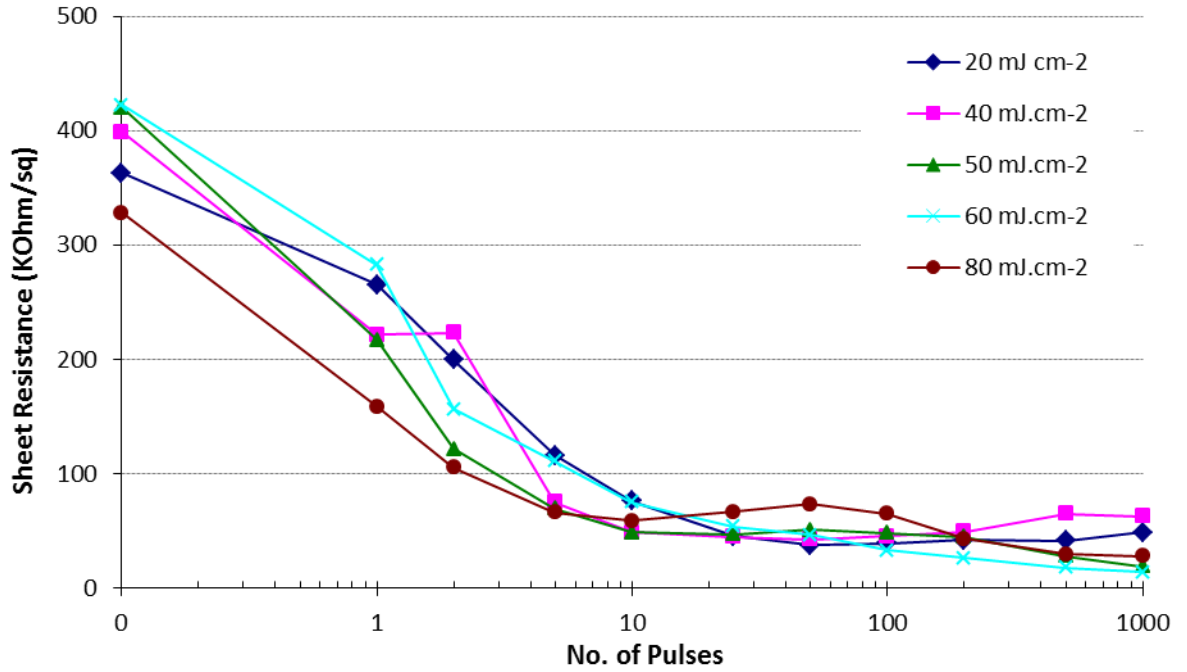


Figure 5.10 : Post KrF laser annealing sheet resistance variation of spin coated 1100 nm thickness SnO<sub>2</sub>:Sb films with respect to number of laser pulses and laser fluence. The zero point represents the as-deposited sheet resistance

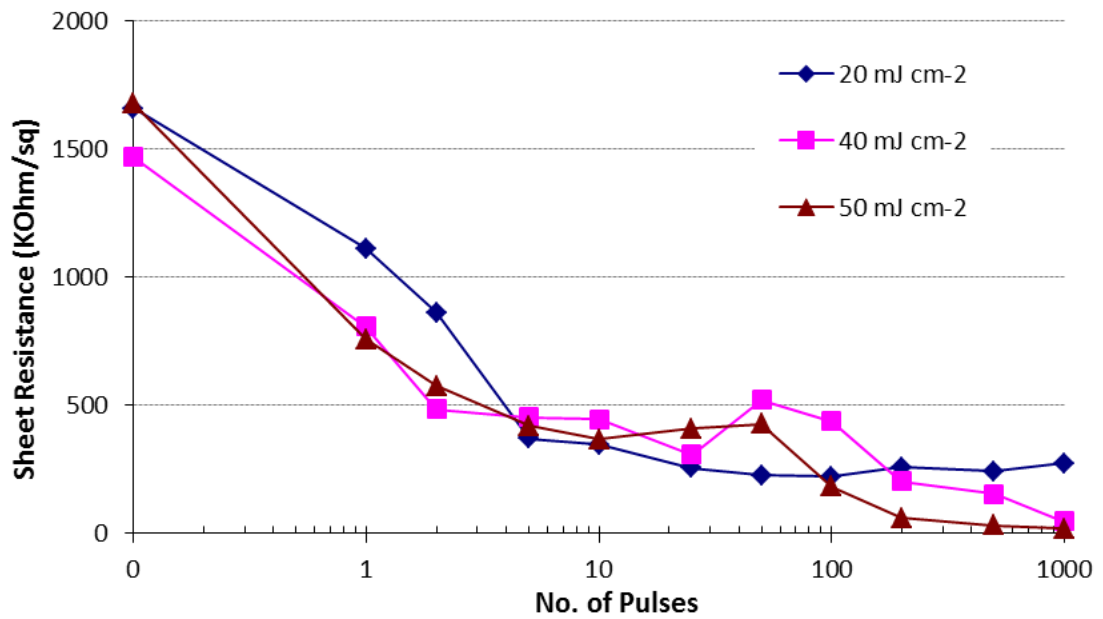


Figure 5.11 : Post KrF laser annealing sheet resistance variation of spin coated 190 nm thickness SnO<sub>2</sub>:Sb films with respect to number of laser pulses and laser fluence.

In figure 5.11, the zero point represents the as-deposited sheet resistance of the SnO<sub>2</sub>:Sb layers. The sheet resistance of these films initially showed greater reduction with the first two laser pulses but after that the reduction had little effect. When processing at higher fluences, the sheet resistance increased to a level not measurable. Some ablation was noted when processing at these higher fluences. The as-deposited sheet resistance of the 190 nm thick films was around 1.5 MΩ/sq and further to KrF laser processing it was reduced to 25 kΩ/sq at 40 mJ.cm<sup>-2</sup> and 1000 pulses.

### 5.4.1.2 Optical transmission

The transmission spectra of the KrF laser processed SnO<sub>2</sub>:Sb films were measured with the Filmetrics optical spectrometer system. Figure 5.12 and 5.13 shows the optical transmission variation of KrF laser processed films with respect to laser fluence and number of laser pulses respectively. For all these measurements the 1100 nm spin coated SnO<sub>2</sub>:Sb films were used.

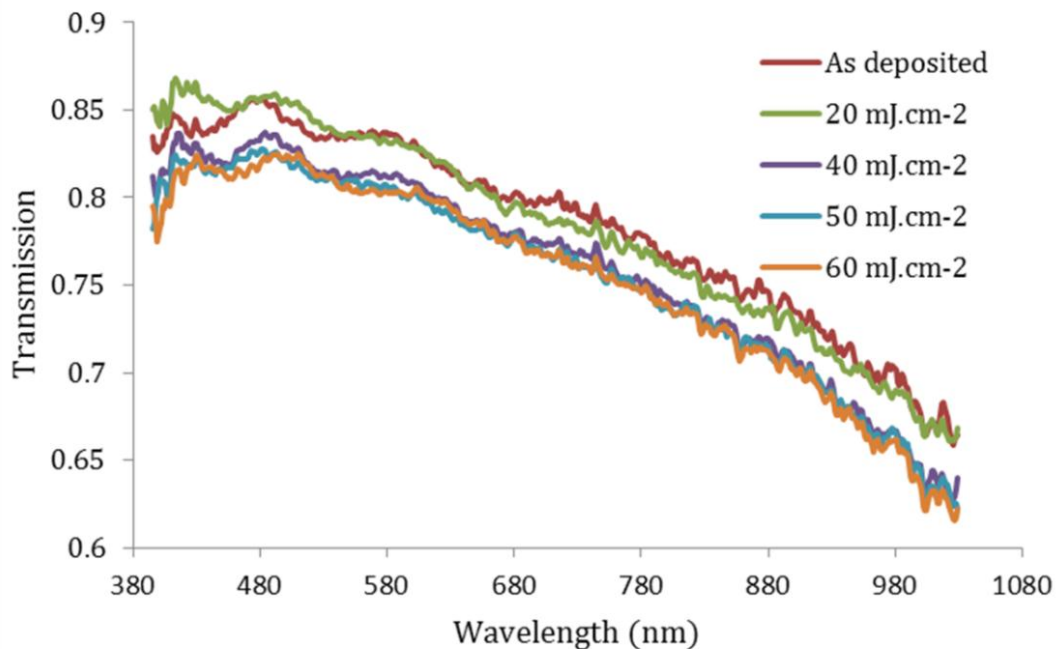


Figure 5.12 : Variation of the transmission of spin coated SnO<sub>2</sub>:Sb films KrF laser processed with 20, 40, 50 and 60 mJ.cm<sup>-2</sup> at 1000 pulses.

With the increase of laser fluence and number of pulses a steady decrease of optical transmission was observed, but in all cases the transmission was above 75% at 550 nm. The reduction of optical transparency in the near infrared region with respect to the increase of laser parameters can be attributed to a shift of the plasma wavelength towards the visible region and indication of an increase of carrier concentration. (This phenomenon is discussed further in chapter 6, in relation to Hall Effect measurement of these films).

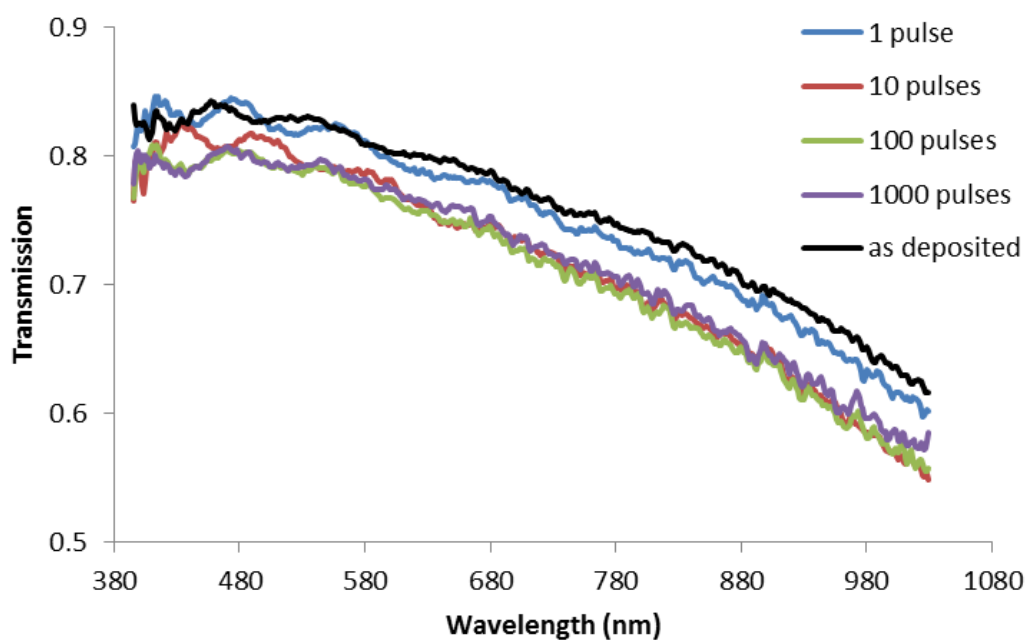


Figure 5.13 : Variation of the transmission of spin coated SnO<sub>2</sub>:Sb films KrF laser processed at 60 mJ.cm<sup>-2</sup> with 1,10,100 and 1000 pulses.

#### 5.4.1.3 XRD

Figure 5.14 shows the X-ray diffraction patterns of KrF laser processed SnO<sub>2</sub>:Sb films. These films were laser processed at 60 mJ.cm<sup>-2</sup>, and the number of pulses were varied between 1- 1000.

The results show the presence of the (110), (101), and (211) reflections of SnO<sub>2</sub> which produce XRD peaks at  $2\theta = 26^\circ$ ,  $33^\circ$ , and  $51^\circ$  respectively. As explained in section 5.2.4

the peaks were identified by using the SnO<sub>2</sub>:Sb PDF file ICSD PDF file 01-088-2348. Further to KrF laser processing no obvious evidence of peak height increase was observed, but indication of peak narrowing was observed at the higher number of pulses. Scherrer's equation (Equation 3.2) was used to calculate the crystalline sizes of the laser processed films. Table 5.3 summarises the findings of the XRD analysis of the laser processed layers.

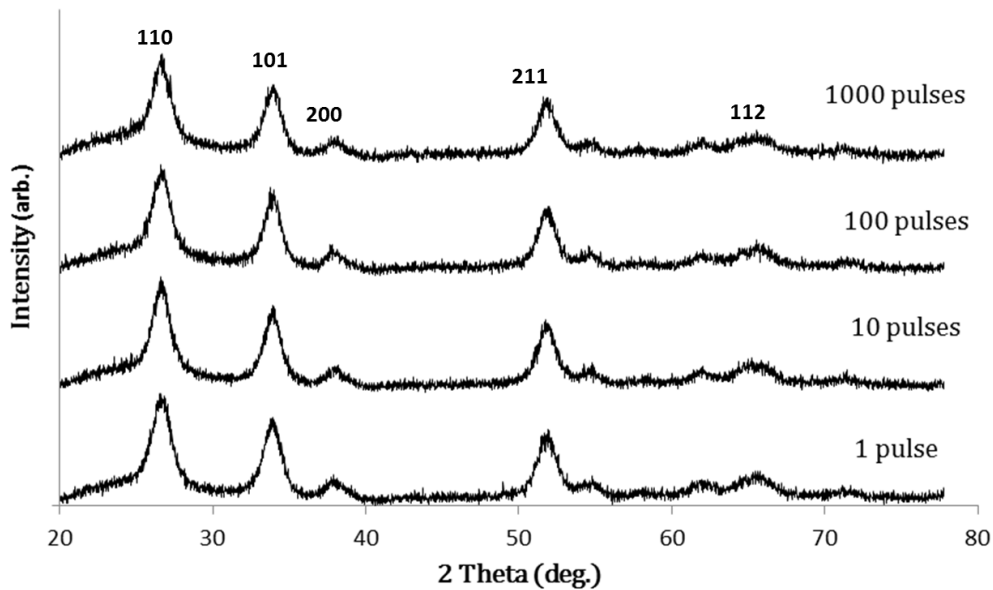


Figure 5.14 : XRD patterns of spin coated SnO<sub>2</sub>:Sb samples KrF laser processed at 60 mJ.cm<sup>-2</sup> with different number of laser pulses.

With respect to the increasing number of laser pulses no significant grain growth was observed when films were laser processed at 60 mJ.cm<sup>-2</sup>. The crystalline sizes as determined by XRD varied between 6 and 8 nm with respect to the number of laser pulses. Therefore, it is reasonable to assume the reduction of sheet resistance observed in section 5.4.1.1 is due to the increase of carrier concentration as grain sizes are not increased. This is also possibly related to the reduction of grain boundary scattering due to removal of inter grain defects or the reduction of barrier heights.

No of laser pulses	<i>h k l</i>	2 theta	FWHM	Crystallise size (nm)
1	110	26.6	1.30	6
	101	33.8	1.20	7
	211	51.8	1.20	7
10	110	26.6	1.20	7
	101	33.9	1.10	7
	211	51.9	1.00	8
100	110	26.6	1.10	7
	101	33.8	1.10	7
	211	51.8	1.20	7
1000	110	26.6	1.10	7
	101	33.9	1.00	8
	211	51.8	1.10	8

Table 5.3 : Summary of XRD findings: Spin coated SnO<sub>2</sub>:Sb –KrF laser processed at 60 J.cm<sup>-2</sup> with 1,10,100 and 1000 pulses

#### 5.4.2 ArF laser processing of spin coated SnO<sub>2</sub>:Sb

One of the advantages of excimer laser processing is the ability to control the irradiation and associated heat penetration depth. This helps to avoid thermal degradation of the substrate, or any underlying interfaces, which is important for devices on flexible substrates where high temperature processes are not suitable. Since the penetration depth is related to the wavelength of the irradiation, it is of interest to examine the effect of different wavelengths. Hence, for this work, the use of 193 nm ArF excimer laser irradiation was also used, which would be expected to have a shallower penetration, due to the higher optical absorption at 193 nm SnO<sub>2</sub>:Sb films (section 6.2.2). Therefore

several SnO<sub>2</sub>:Sb samples on Eagle XG glass substrate have been ArF laser processed by varying the laser fluences and number of laser pulses.

#### 5.4.2.1 Sheet resistance

Figure 5.15 shows the variation in sheet resistance following ArF laser processing of spin coated SnO<sub>2</sub>:Sb with respect to number of laser pulses and laser fluence. The zero point represents the as-deposited sheet resistance.

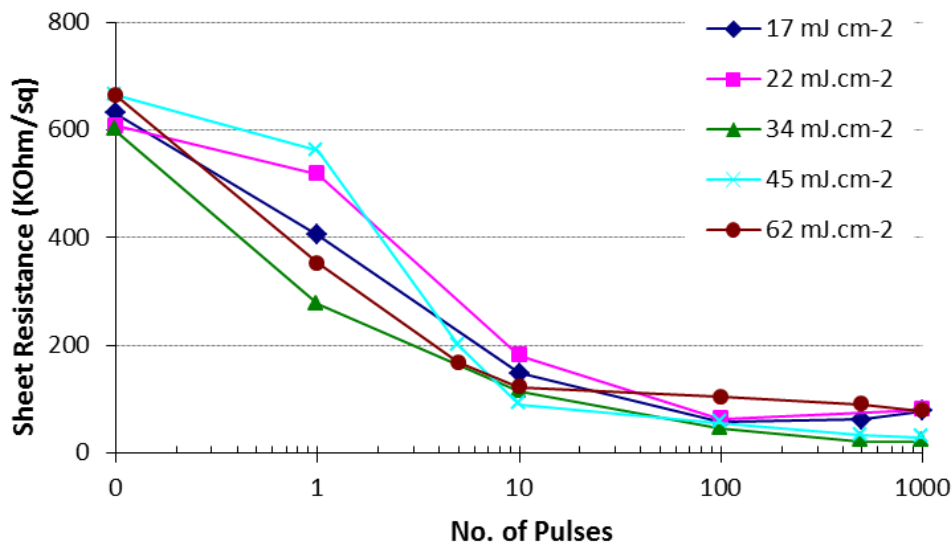


Figure 5. 15 : Post ArF laser annealing sheet resistance variation of spin coated 1100 nm thickness SnO<sub>2</sub>:Sb films with respect to number of laser pulses and laser fluence.

ArF laser processed films exhibit the same tendency in terms of sheet resistance reduction with fluence and number of pulses as the KrF laser processed films, but it is noted that during the first 10 pulses a greater reduction from initial value of sheet resistance was observed. The average as-deposited sheet resistance of these films were around 600 kΩ/sq and further to laser processing sheet resistance was reduced to around 20 kΩ/sq when processed at 34 mJ.cm<sup>-2</sup> and 1000 pulses.

## 5.5 Combined processing-Thermal annealing followed laser processing of SnO<sub>2</sub>:Sb

The objective of this research work is to investigate lower temperature processes to functionalise SnO<sub>2</sub>:Sb layers. Excimer laser processing has been demonstrated to be an effective technique to reduce the sheet resistance of SnO<sub>2</sub>:Sb layers, but the reduction due to laser processing is not sufficient to use these films as transparent electrodes. Therefore, lower temperature thermal annealing combined with excimer laser processing was also studied. Sandu et al [84] used a similar technique where they initially oven dried dip coated SnO<sub>2</sub>:Sb layers at 200<sup>0</sup>C for nearly 5 hrs before excimer laser processing. For the work presented here, different thickness SnO<sub>2</sub>:Sb layers were initially thermal annealed before excimer laser processing at the optimum processing conditions identified in section 5.4.

### 5.5.1 Lower temperature thermal annealing of different thickness SnO<sub>2</sub>:Sb

For this experiment, four samples from different thickness SnO<sub>2</sub>:Sb batches were used and each sample was cut into four sections to be thermal annealed at different temperatures. Table 5.4 shows the summary of the samples used for this part of the work.

Film thickness (nm) \ Annealing Temp <sup>0</sup> C	378	487	850	1100
100	Sa1-1	Sa2-1	Sa3-1	Sa4-1
200	Sa1-2	Sa2-2	Sa3-2	Sa4-2
300	Sa1-3	Sa2-3	Sa3-3	Sa4-3
400	Sa1-4	Sa2-4	Sa3-4	Sa4-4

Table 5.4 : Summary of the samples used for the thermal annealing of SnO<sub>2</sub>:Sb

Initially, the Heraeus D-6450 Hanau conventional oven was used to thermal anneal the films at the temperatures indicated in table 5.4 for 1hr. Then the sheet resistance of the resultant films were measured.

Post thermal annealing sheet resistances were measured using four point probes. The sheet resistance variations of different thickness samples with respect to the thermal annealing temperatures are shown in Table 5.5. Further to thermal annealing, all films showed a reduction in sheet resistance compared to their as-deposited sheet resistances. For the same thickness films, the sheet resistance fell dramatically with increasing thermal annealing temperature. For all thicknesses the lowest sheet resistance occurred with the highest thermal annealed temperature. Hence, the lowest sheet resistance of 1.3 KΩ/sq was obtained with the 1100 nm thickness SnO<sub>2</sub>:Sb when thermal annealed at 400°C for ~1hr.

Film thickness (nm) \ Annealing Temp (°C)	378	487	850	1100
100	1438	1413	1088	506
200	404	261	214	63
300	118	47	28	56
400	3.8	2.3	1.6	1.3

Table 5.5 : Sheet resistance (KΩ/sq) of thermal annealed SnO<sub>2</sub>:Sb films with respect to annealing temperature and the film thickness .

**5.5.1 Excimer laser processing of the thermal annealed different thickness SnO<sub>2</sub>:Sb**

Further to thermal annealing, the different thickness SnO<sub>2</sub>:Sb layers were KrF laser processed at 60 mJ/cm<sup>2</sup>, with 1000 laser pulses and subsequently characterised for sheet resistance, with the results as tabulated Table 5.6.

		Film Thickness			
		378 nm	487 nm	850nm	1100 nm
Thermal annealed temperature (°C)	100°C	1438	1412	1087	506
		23.5	22.4	18.5	19.2
200°C	200°C	404	261	213	62
		13.8	12.1	12.6	10.3
300°C	300°C	117	46	28	5.6
		9.5	6.9	4.9	1.9
400°C	400°C	3.8	2.3	1.6	1.3
		1.7	1.13	0.84	0.79

Thermal annealed sheet resistance (kΩ)
Combined processed sheet resistance (kΩ)

Table 5.6 : Variation of combined processed and thermal annealed sheet resistances (kΩ/sq) of SnO<sub>2</sub>:Sb layers with respect to the thermal annealing temperature and film thicknesses.

As shown in Table 5.6, irrespective of film thickness, all the thermal annealed samples show a reduction of sheet resistance further to laser processing at 60mJ.cm<sup>-2</sup> with 1000 pulses. The post laser processing sheet resistance was dramatically reduced for the films which are initially thermal annealed at 100<sup>0</sup>C and then laser processed. The films thermal annealed at 400<sup>0</sup>C also show some reduction of sheet resistance further to laser

processing. Figure 5.16 shows the sheet resistance variation of different thicknesses SnO<sub>2</sub>:Sb layers when thermal annealed at 400<sup>0</sup>C and also when subjected to the combined processing. These results clearly show that for all the thicknesses laser processing further reduced the sheet resistance of the films. Chapter 6 further discusses the mechanisms responsible for improvement of the conductivity of these films, but it is reasonable to assume that initial lower temperature thermal annealing helps to reduce the ink residuals within the films and further laser processing affects the grain boundaries and scattering which helps to reduce the film sheet resistance.

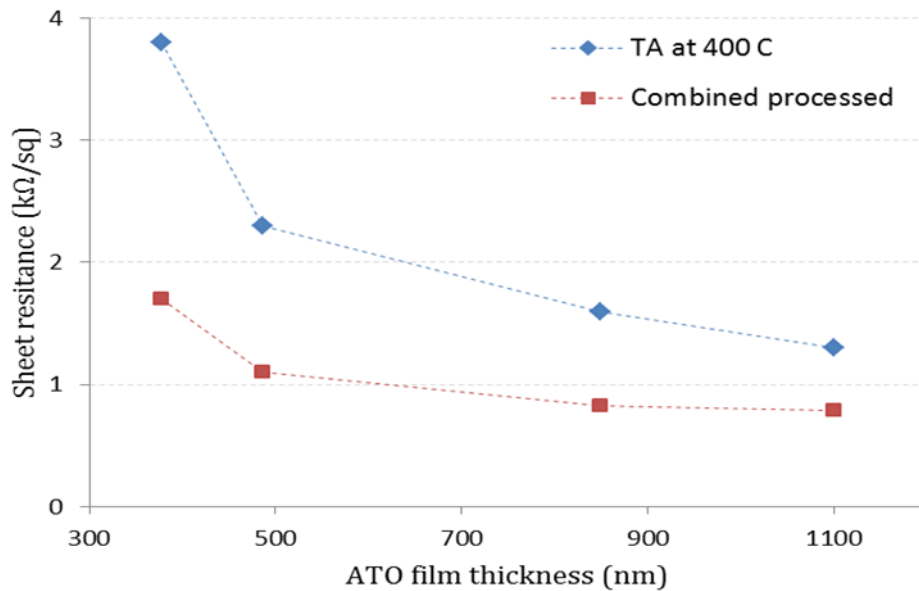


Figure 5.16 : Variation of the sheet resistance with SnO<sub>2</sub>:Sb film thickness for thermal annealed at 400<sup>0</sup>C films and combined processed films.

As shown in the figure 5.16 this combined processing technique can be used to obtain sheet resistances <1 kΩ/sq for 1100 nm and 850 nm thickness spin coated SnO<sub>2</sub>:Sb films which is of the order required for use as transparent electrodes in ACEL devices. Hence films processed using these conditions have been used for ACEL device feasibility testing as presented in chapter 7.

## 5.6 Discussion:

This chapter presented the results from a study of the electrical, optical, and structural properties of spin coated SnO<sub>2</sub>:Sb films on Eagle XG glass substrates. The first part of the chapter discussed the thickness optimisation of as-deposited SnO<sub>2</sub>:Sb films. Subsequently, these films were post processed using three different techniques: (a) Thermal annealing (b) Excimer laser processing (c) Combined processing: lower temperature thermal annealing followed by excimer laser processing. The second half of the chapter detailed the electrical, optical and structural properties of post processed SnO<sub>2</sub>:Sb layers.

During this study the films were thermal annealed at temperatures in the range of 100 to 700°C for 1 hr resulting in the sheet resistance of the films being dramatically reduced. When films were thermal annealed at 700°C, the greatest reduction of sheet resistance was obtained with the sheet resistance being reduced to 120 Ω/sq while the transmission remained at over 80% (at 550 nm).

When films were excimer laser processed with 248 nm and 193 nm irradiation, a corresponding reduction of sheet resistance was observed with the increase of laser parameters (fluence and or number of pulses). It has been found that low laser fluences combined with higher number of laser pulses gives better results without deteriorating the optical transparency. Further to KrF laser processing, the sheet resistance of the spin coated films was reduced to 20 kΩ/sq and the optical transmission remained >75% at 550 nm.

Combined thermal and laser processing of SnO<sub>2</sub>:Sb offers the potential to use solution processed SnO<sub>2</sub>:Sb layers for low temperature, low cost transparent electrode applications. Thermal annealing followed by KrF laser processing reduces the sheet resistance of SnO<sub>2</sub>:Sb to the region of 1 kΩ/sq, which is suitable for use in ACEL devices – as was subsequently demonstrated by the test device fabrication reported in chapter 7.

XRD studies shows no significant grain growth following either excimer laser processing or lower temperature thermal annealing, but samples that were thermal annealed at 700<sup>0</sup>C exhibited evidence of grain sizes being increased to 9 nm from the as-deposited value of 6 nm.

The underlying mechanisms for these changes in properties as a function of processing treatment are considered in chapter 6.

## **6. Analysis & conduction mechanism of spin coated SnO<sub>2</sub>:Sb**

### **6.1 Introduction**

In this research work three different post processing techniques were investigated to functionalise the spin coated SnO<sub>2</sub>:Sb layers: thermal annealing, excimer laser processing and combined processing (lower temperature thermal annealing followed by excimer laser processing). Following the initial period of investigation to determine the post processing conditions to anneal spin coated SnO<sub>2</sub>:Sb films (chapter 5), the following processing conditions were selected as optimum for each method to anneal the films to achieve the best combination of electrical conductivity and optical transmission in the visible region.

1. Thermal annealing at 700<sup>0</sup>C for 1 hr
2. KrF Excimer laser processing at 60 mJ/cm<sup>2</sup> with 1000 pulses
3. Combined processing: Thermal annealing at 400<sup>0</sup>C for 1 hr, then KrF laser processing at 60 mJ/cm<sup>2</sup> with 1000 pulses

Several batches of samples were prepared with the above processing conditions and characterised in terms of their electrical, optical, chemical and structural properties to investigate the conduction mechanisms and the reduction of sheet resistance with respect to the processing conditions.

## 6.2 Analysis of spin coated SnO<sub>2</sub>:Sb films

### 6.2.1 Electrical properties

The electrical properties of the as-deposited, KrF laser processed and thermal annealed SnO<sub>2</sub>:Sb samples were studied by the use of Hall Effect and four point probe measurements. The Hall Effect measurements of the SnO<sub>2</sub>:Sb films were carried out to determine the Hall mobility and carrier concentration contribution to the reduction of sheet resistance of the post processed films. For these measurements the author prepared the SnO<sub>2</sub>:Sb samples for measurement by collaborators at Warwick University and the University of Oxford. In both cases the Van der Pauw technique was used. Dr. Tim Veal at the University of Warwick and Dr. Vladimir Kuznetsov at Oxford University are acknowledged for their assistance in undertaking these measurements.

Twelve layer spin coated SnO<sub>2</sub>:Sb samples with the film thickness of 1100 nm from K&W were used for the measurements. Initially, the spin coated SnO<sub>2</sub>:Sb samples were cut into 1 cm<sup>2</sup> areas, which were subsequently used for excimer laser processing and thermal annealing trials at different laser conditions and different temperatures. The post processing details and the sheet resistance measurements further to post processing at NTU are summarised in Table 6.1.

All the Hall Effect measurements were obtained at room temperature and no contact points were made prior to the measurements. The measured Hall mobility and carrier concentrations for different post processing techniques are shown in figure 6.1(a) and 6.1 (b) respectively.

Sample ID	Post processing technique	Sheet resistance (KΩ/sq)
KWATO56-1	As deposited ATO	415.5
KWATO56-2	Thermal annealed at 700 <sup>0</sup> C	0.102
KWATO56-3	Laser processed ( 60 mJ/cm <sup>2</sup> , 10 pulses)	78.6
KWATO56-4	Laser processed ( 20 mJ/cm <sup>2</sup> , 10 pulses)	136
KWATO56-5	Laser processed ( 60 mJ/cm <sup>2</sup> , 1000 pulses)	30
KWATO56-6	Laser processed ( 20 mJ/cm <sup>2</sup> , 1000 pulses)	92.6
KWATO56-8	Thermal annealed at 400 <sup>0</sup> C & laser processed (60 mJ/cm <sup>2</sup> 1000 pulses)	0.9

Table 6.1 : Summary of the spin coated SnO<sub>2</sub>:Sb films used for Hall Effect measurement. The sheet resistance was measured using four point probes.

For the thermal annealed samples, the carrier concentration and carrier mobility increases with the annealing temperature. When films are annealed at 700<sup>0</sup>C the measured carrier concentration and carrier mobility is increased to 2.8 x 10<sup>20</sup> cm<sup>-3</sup> and 2.3 cm<sup>2</sup> V<sup>-1</sup> s<sup>-1</sup> respectively from their as-deposited values of 1.8 x 10<sup>17</sup> cm<sup>-3</sup> and 1.77 cm<sup>2</sup> V<sup>-1</sup> s<sup>-1</sup>. Similar results were reported by Huang et al [57] when thermal annealing RF reactive magnetron sputtered SnO<sub>2</sub>:Sb films in Nitrogen and Oxygen environments. They reported mobility of 1.7 and 4 cm<sup>2</sup> V<sup>-1</sup> s<sup>-1</sup> and carrier concentration around 1.5 x 10<sup>20</sup> cm<sup>-3</sup> and 2.5 x 10<sup>20</sup> cm<sup>-3</sup> for their films when thermal annealed at 200<sup>0</sup>C and 400<sup>0</sup>C respectively. The enhancement of the carrier mobility can be described as a result of decrease in carrier scattering, which can be attributed to the reduction in grain boundaries, and thus the mobility is enhanced. Hence the reduction of sheet resistance was observed with increasing annealing temperature.

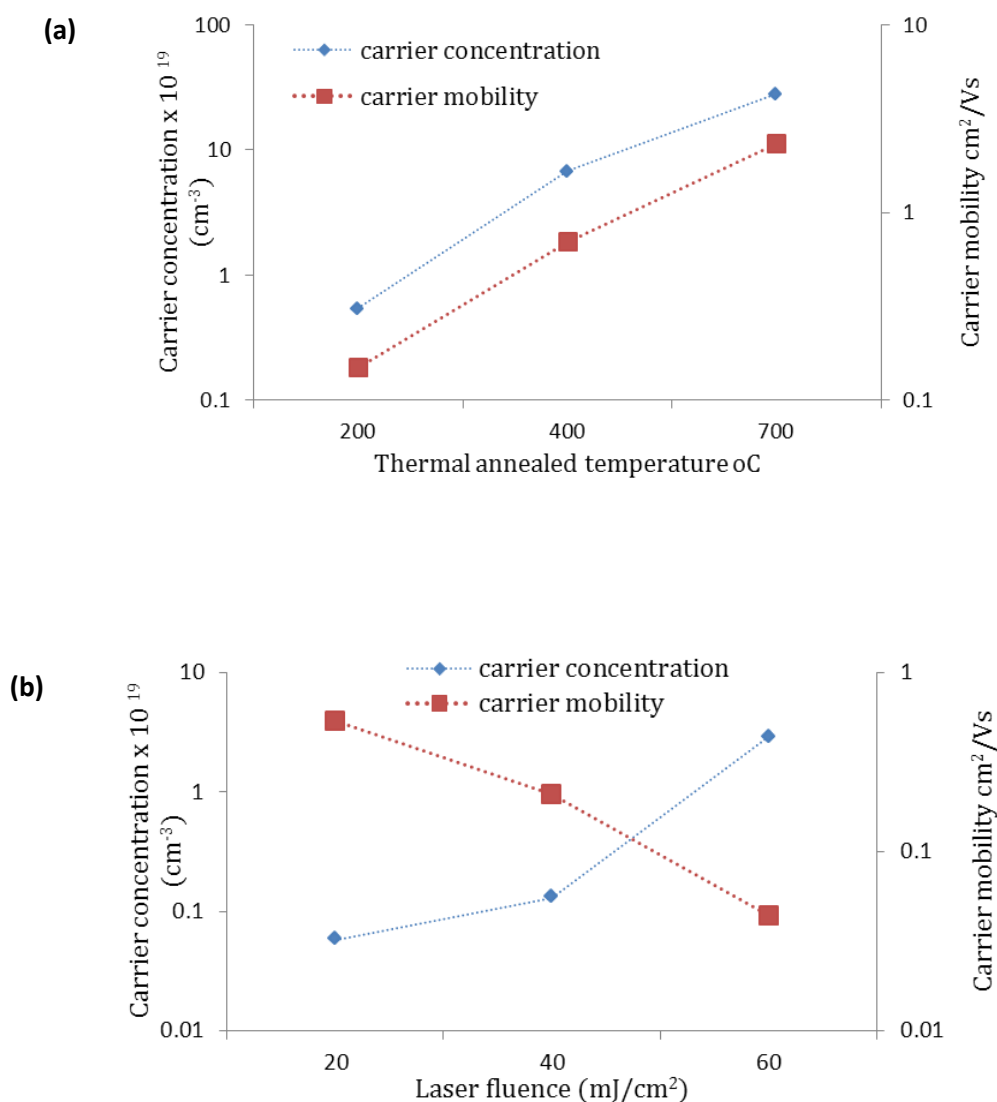


Figure 6.1 : Carrier mobility and carrier concentration variation of spin coated SnO<sub>2</sub>:Sb films as a function of (a) thermal annealed temperature (b) excimer laser fluence

A different trend is observed for the laser processed films. As shown in figure 6.1 (b), when spin coated SnO<sub>2</sub>:Sb films were excimer laser processed at different fluencies, the carrier concentration improved with the laser fluence while the carrier mobility decreases. Specifically, when films were laser processed at 60 mJ.cm<sup>-2</sup> at 1000 pulses, the carrier concentration improved to 2.9 x 10<sup>19</sup> cm<sup>-3</sup> from the as-deposited value of 1.8 x 10<sup>17</sup> cm<sup>-3</sup>, while the Hall mobility was reduced to 0.04 cm<sup>2</sup> V<sup>-1</sup> s<sup>-1</sup> from it's as-deposited value of 1.17 cm<sup>2</sup> V<sup>-1</sup> s<sup>-1</sup>.

### 6.2.2 Optical properties

In order to study the optical properties in the UV-visible range, a batch of SnO<sub>2</sub>:Sb samples were deposited onto fused silica substrates. Figure 6.2 shows the resultant transmission and reflection spectra of as-deposited, thermal annealed and laser processed SnO<sub>2</sub>:Sb layers for different processing conditions. These measurements were taken using a PerkinElmer Lambda 650 spectrometer at Brunel University, UK. Dr. Paul Harris at Brunel University was acknowledged for his assistance.

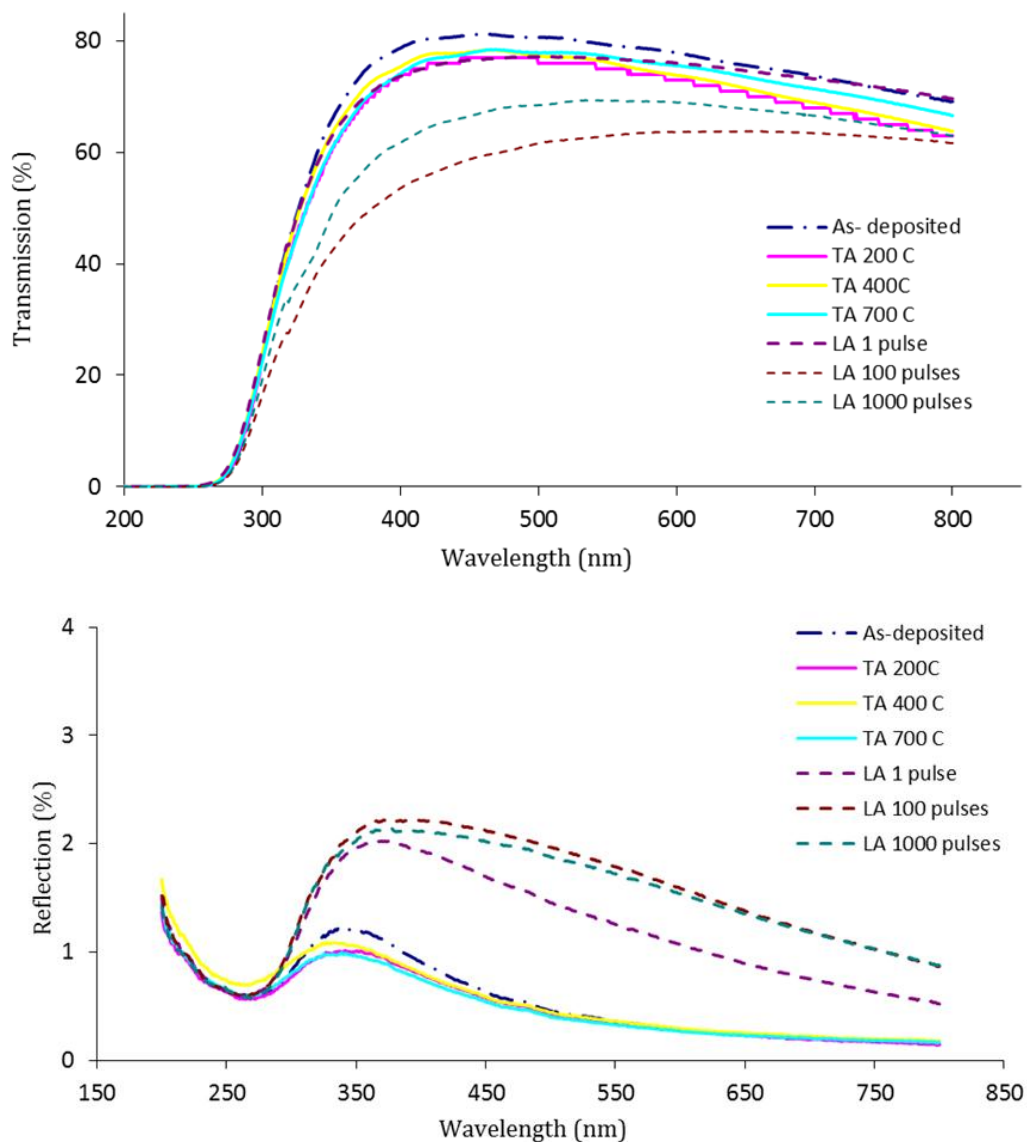


Figure 6.2 : Transmission (above) and Reflection spectra (bellow) of: As-deposited, thermal annealed (TA), and Excimer laser processed (LA) at 60 mJ.cm<sup>-2</sup>, SnO<sub>2</sub>:Sb

As shown in figure 6.2, the as-deposition transmission at 550 nm was around 80% while further to post processing some reduction of transmission was observed (the thickness of all the deposited films was around 1.1 μm). In general, the thermal annealed films show a higher transmission in the visible region compared to the laser processed films. When the films were laser processed with the higher number of pulses, a more pronounced reduction of transmission is observed. This may be due to enhanced absorption or impurity scattering mechanisms. A blue shift was not observed for post processed films compared to as-deposited layers, suggesting these films were not degenerately doped with these processing conditions. These findings are in agreement with the Hall Effect measurement results which show the highest carrier concentration of 10<sup>20</sup>cm<sup>-3</sup> for thermal annealed films at 700<sup>0</sup>C .

The reflection measurements show that the visible region reflections of as-deposited and thermal annealed films are almost similar. In contrast, the excimer laser processed layers show a higher reflection in the visible region compared to the other films.

The transmission spectra in figure 6.2 was used to obtain the variation in absorption coefficient (α) with respect to the wavelength of as-deposited SnO<sub>2</sub>:Sb by using Equation 2.4. Figure 6.3 shows the variation in absorption coefficient with respect to the wavelength of as-deposited SnO<sub>2</sub>:Sb.

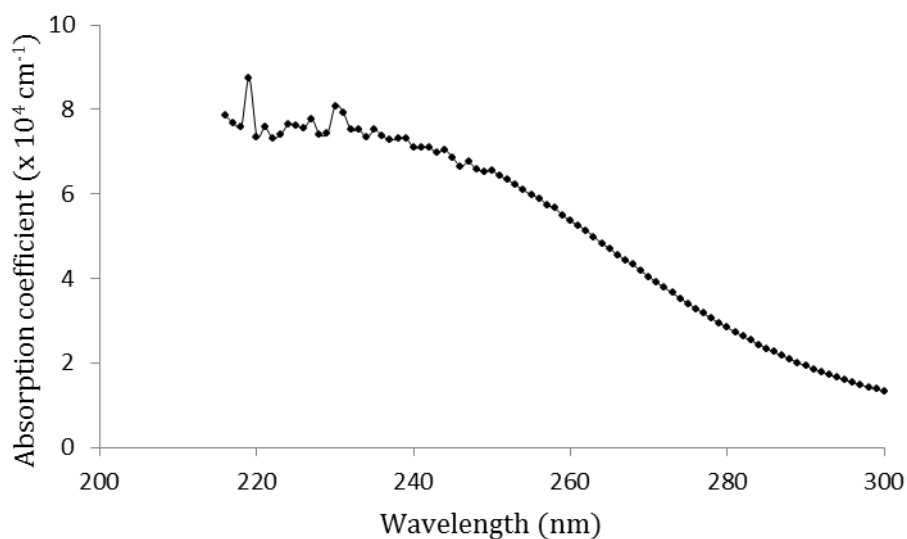


Figure 6.3 : Variation of absorption coefficient (α) with wavelength of as-deposited SnO<sub>2</sub>:Sb

According to the figure 6.3, the optical absorption of the as-deposited SnO<sub>2</sub>:Sb films at 248 nm is  $6.6 \times 10^4 \text{ cm}^{-1}$ . This is in agreement with the values reported by Sandu et al [84] for the dip coated SnO<sub>2</sub>:Sb films, where they reported optical absorption,  $\alpha = 1.5 \times 10^5 \text{ cm}^{-1}$  at 193 nm and  $\alpha = 0.7 \times 10^5 \text{ cm}^{-1}$  at 248 nm.

The fundamental absorption corresponds to electron excitation from the valence band to the conduction band and can be used to examine the nature and value of the optical band gap. The optical band gap of the as-deposited, thermal annealed and laser processed films were retrieved from the transmission spectra as explained in section 2.1.3.1. Figure 6.4 and 6.5 convey the direct optical band gap extraction of SnO<sub>2</sub>:Sb, for different thermal annealed and laser processed conditions respectively.

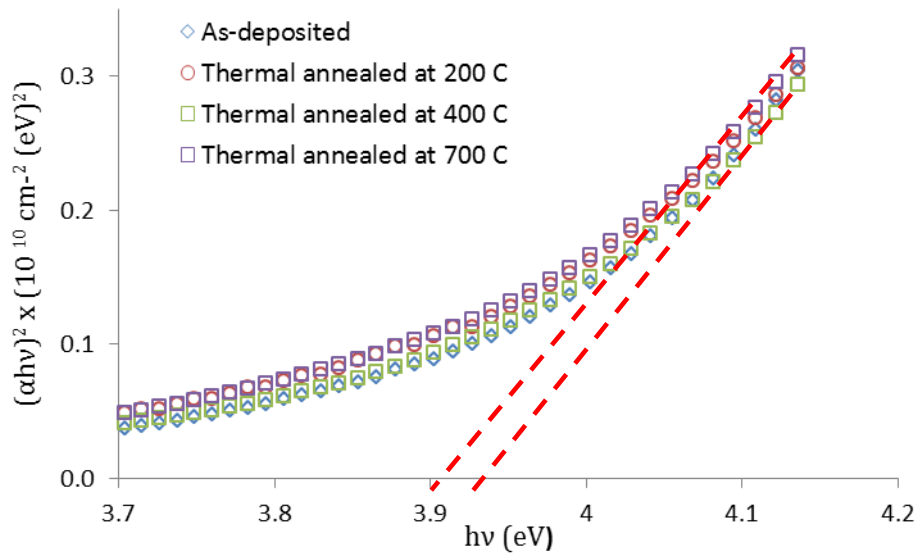


Figure 6.4 : Representative absorption curves of thermal annealed SnO<sub>2</sub>:Sb for optical band gap extraction.

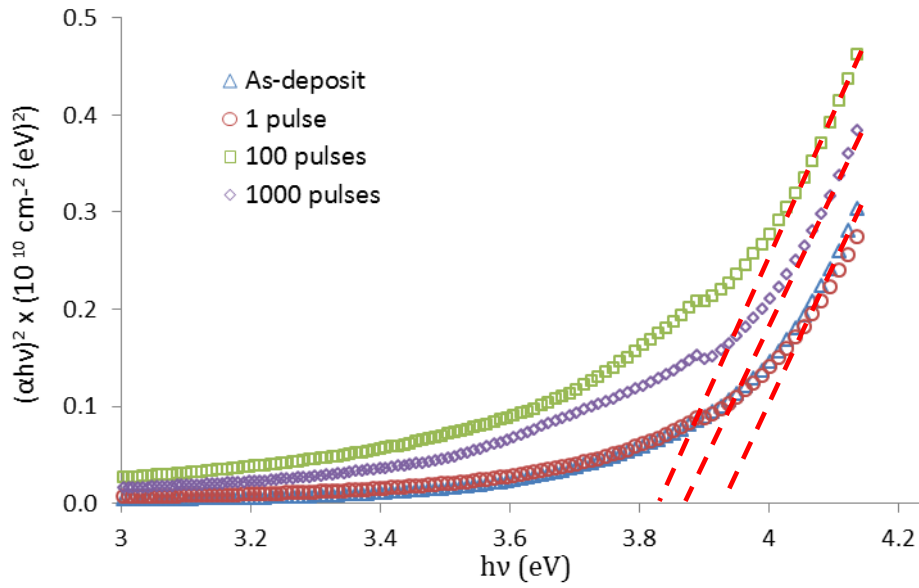


Figure 6.5 : Representative absorption curves of laser processed at 60mJ/cm<sup>2</sup> SnO<sub>2</sub>:Sb for optical band gap extraction

The optical band gap was extrapolated from  $(\alpha h\nu)^2$  vs the photon energy,  $h\nu$  curve for three different thermal annealing temperatures: 200<sup>0</sup>C , 400<sup>0</sup>C and 700<sup>0</sup>C . For thermal annealed films the optical band gap was around 3.9 eV. Even though the carrier concentration was increased with the increase of thermal annealing temperature, a prominent band gap expansion was not observed due to the Burstein-Moss shift. Therefore it is difficult to conclude that due to thermal annealing the optical band gap has been modified. Terrier et al [112] also reported similar results for their low temperature deposited sol-gel dip coated SnO<sub>2</sub>:Sb films. They reported optical band gap of around 3.85 eV for their films for different film thicknesses and doping concentrations. The extracted optical band gap values here correspond to the values given in literature by other authors, [34, 74, 113] where the optical band gap varies between 3.4 and 4.2 eV depending on deposition technique and other processing parameters.

Figure 6.5 shows the optical band gap variation for excimer laser processed SnO<sub>2</sub>:Sb films with respect to the number of irradiated laser pulses. As the number of pulses increases, the results indicate that the optical band gap of the SnO<sub>2</sub>:Sb films reduces and then expands. When the number of irradiated laser pulses was increased up to 1000, the

optical band gap starts to expand due to an increase of carrier concentration, as explained in section 6.1 and also due to the reduction of grain boundary scattering. A similar variation was observed with the sheet resistance variation with respect to the number of laser pulses of the spin coated SnO<sub>2</sub>:Sb films, as around 100 pulses the sheet resistance was slightly increased and then started to reduce to its minimum value (chapter 5).

### 6.2.3 Structure and morphology

The XRD patterns of the as- deposited and post processed SnO<sub>2</sub>:Sb films along with the crystallite sizes as determined by Scherrer equation was discussed in Chapter 5. Relating to the crystallite sizes, the lattice parameters and the cell volumes of as-deposited and optimum post processed SnO<sub>2</sub>:Sb samples are discussed here. As explained in chapter 5, XRD characterisation of SnO<sub>2</sub>:Sb suggested that the films are polycrystalline and retain the tetragonal rutile structure. Thus the lattice parameters, lattice distortion ratio and the cell volume can be derived as follows:

The planer spacing for Tetragonal structure can written as,

$$\frac{1}{d^2} = \frac{h^2 + k^2}{a^2} + \frac{l^2}{c^2} \quad \text{Eq 6.1}$$

Where  $d$  is the-inter planer spacing, (h,k,l) are the spacing between lattice plans (Miller indices) and  $a$  and  $c$  are the lattice parameters.

Therefore relating to the Braggs law, equation 6.1 can re-written as,

$$\sin^2 \theta = \frac{\lambda^2}{4a^2} (h^2 + k^2) + \frac{\lambda^2}{4c^2} (l^2) \quad \text{Eq 6.2}$$

By using lattice parameters, the cell volume,  $V$  can be calculated as [114] ,

$$V = a^2 c \quad \text{Eq 6.3}$$

Table 6.2 lists the calculated lattice parameters and cell volumes for as-deposited and optimum post processed SnO<sub>2</sub>:Sb films. The calculated values are compared with the standard pattern values of SnO<sub>2</sub>:Sb (ICSD card No. 01-088-2348). The lattice constants and the cell volumes were determined from the (110) and (101) planes. It is observed from the results in Table 6.2 that the calculated cell parameters are in agreement with standard tetragonal SnO<sub>2</sub>:Sb pattern values. However the slight variation between calculated as-deposited SnO<sub>2</sub>:Sb cell parameters and the standard cell parameters are mainly related to the variations in the doping concentrations of the as-deposited and standard samples.

The variation in the cell parameters with respect to the sample preparation is related to the amount of partial replacement of Sn<sup>4+</sup> ions in the SnO<sub>2</sub> lattice by Sb<sup>5+</sup> and Sb<sup>3+</sup> ions. When Sb is incorporated to the SnO<sub>2</sub> lattice to replace the Sn<sup>4+</sup> ions in the form of Sb<sup>3+</sup>, the cell parameters tends to expand. This is due to the fact that the ionic radius of Sn<sup>4+</sup> (0.71 Å) is smaller than ionic radius of Sb<sup>3+</sup> (0.76 Å). However, as the result of replacement of Sn<sup>4+</sup> ions in the SnO<sub>2</sub> lattice by the Sb<sup>5+</sup> ions, the cell parameters will shrink, since Sb<sup>5+</sup> has a comparably smaller ionic radius (0.62 Å) to Sn<sup>4+</sup> ions [69].

Preparation	2θ	hkl	a / Å	c / Å	Average a / Å	Average c / Å	V / Å <sup>3</sup>
ICSD card	-		4.7373	3.1816	-	-	71.40
As-deposited ATO	26.70	110	4.717		4.7285	3.1793	71.08
	33.98	101		3.178			
	38.00	200	4.732				
	51.91	211		3.121			
	54.78	220	4.736				
	61.99	310	4.729				
	65.82	301		3.239			

Oven annealed at 700 <sup>o</sup> C for 1hour	26.71	110	4.716		4.7300	3.1790	71.12
	33.97	101		3.181			
	38.03	200	4.737				
	51.89	211		3.177			
	54.76	220	4.737				
	61.99	310	4.730				
KrF Laser processed (60 mJ/cm <sup>2</sup> , 1000 pulses)	26.71	110	4.716		4.7215	3.1735	70.75
	33.96	101		3.182			
	38.04	200	4.727				
	51.91	211		3.165			

Table 6.2 : Cell parameters of as-deposited and post processed SnO<sub>2</sub>:Sb

According to the data presented in Table 6.2, the thermally annealed sample shows an expansion of its cell volume compared to the as-deposited sample, while the laser processed samples exhibit some shrinkage to the cell volume. This suggests that the majority of the Sn<sup>4+</sup> ions in the thermally annealed sample have been replaced by Sb<sup>3+</sup> ions, while the majority of the Sn<sup>4+</sup> ions in the excimer laser processed samples have been replaced more dominantly by the Sb<sup>5+</sup> ions.

Zhang et al [69] reported similar cell parameters variation of their SnO<sub>2</sub>:Sb films deposited by spray pyrolysis method. When the Sb/Sn at.% varied from 0 to 2.5%, they reported variation of lattice parameters of *a* from 4.737 to 4.764 Å and *c* from 3.187 to 3.192 Å respectively, but for the results presented here, there is indication of a different mechanism of Sb incorporation for the two different post deposition processing methods.

The microstructure of the thin film samples of the optimum post processed SnO<sub>2</sub>:Sb were examined using a Joel 200FX TEM operating at 200kV. The TEM analysis was performed at Sonsam Ltd, Glebe Laborries, Ireland. The author post processed a set of

SnO<sub>2</sub>:Sb samples from K&W Ltd and sent for TEM characterisation. The detailed TEM results of the as-deposited, thermal annealed and laser processed layers are explained here. All the SnO<sub>2</sub>:Sb samples were deposited on Eagle XG glass substrates, with 10 and 12 layer deposited SnO<sub>2</sub>:Sb samples used for this part of the investigation.

### 6.2.3.1. As- deposited SnO<sub>2</sub>:Sb

Figure 6.6 shows the TEM cross section of the as- deposited SnO<sub>2</sub>:Sb layer. The image shows a banded morphology which is often typical of spin coated and dip coated samples [83]. The as-deposited layer consists of 10 layers and the layer thickness is around 850 nm.

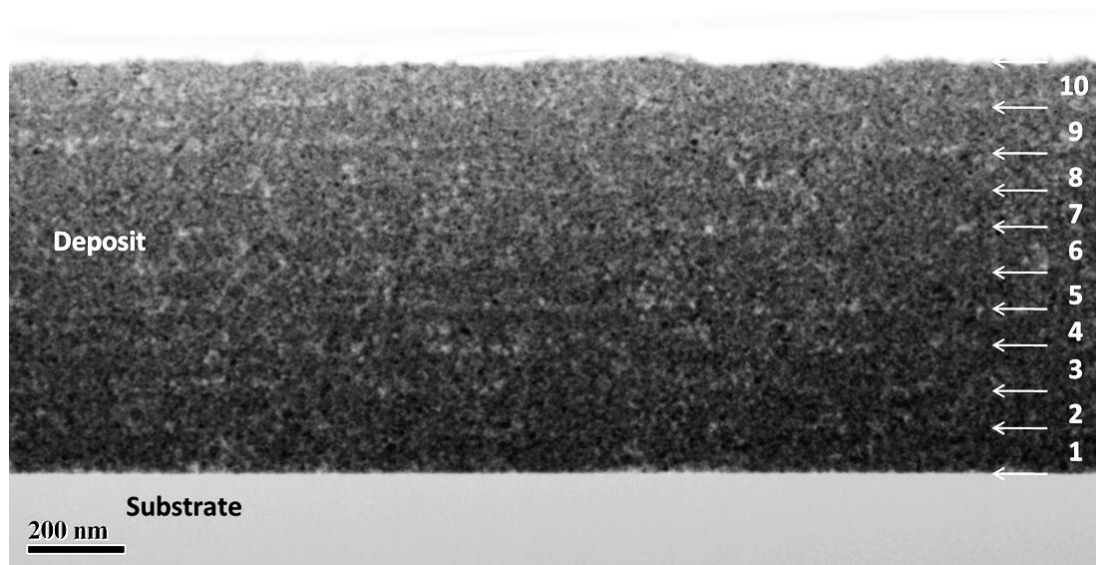


Figure 6.6 : TEM cross section of a 10 layers SnO<sub>2</sub>:Sb coating on glass substrate.

The morphology reveals that each layer of the multilayer coating was composed of fine grains and each individual layer consists of a thin, relatively dense interface lying on top of a more porous material. The average grain size observed varies between 3 and 7 nm. Figure 6.7 shows the corresponding electron diffraction pattern of the as-deposited SnO<sub>2</sub>:Sb films. It shows that there is no evidence of the presence of Sb<sub>2</sub>O<sub>3</sub> in the sample (with the absence of the (020) ring spacing at 0.6375 nm for Sb<sub>2</sub>O<sub>3</sub>). The measured and

standard d-spacing of SnO<sub>2</sub> lattice (PDF file No: 21-1250) are summarised in Table 6.3. The measured values are consistent with the standard values and only some weak reflections correspond to (111), (210), (310),(310) which were difficult to distinguish.

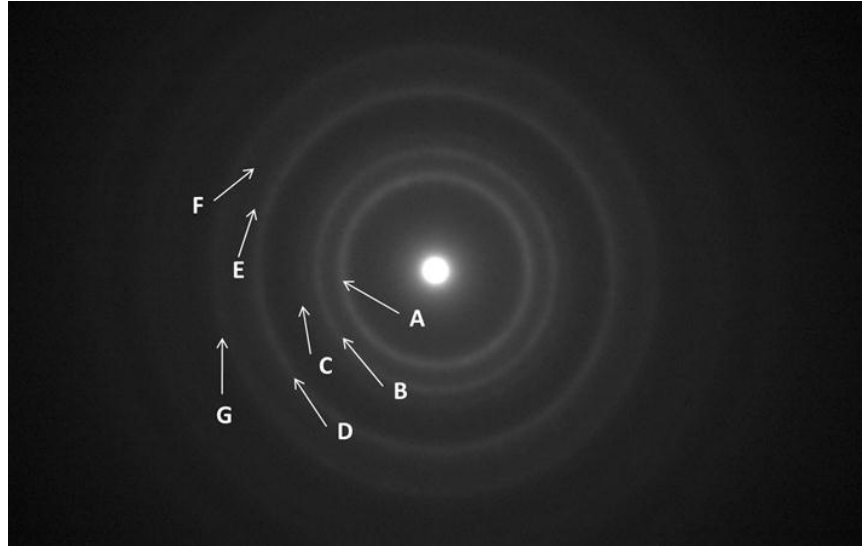


Figure 6.7 : Electron diffraction pattern of the as-deposited SnO<sub>2</sub>:Sb layer – where the rings correspond to lattice spacings of: A= 0.3345 Å, B= 0.2652 Å, C= 0.2365 Å, D= 0.1747 Å, E= 0.1634 Å, F= 0.1544 Å and G= 0.1418 Å.

<i>hkl</i>	d- spacing (nm)	
	Standard (PDF file No: 21- 1250)	TEM analysis
110	3.3510	3.345
101	2.6440	2.652
200	2.369	2.365
111	2.309	-
210	2.120	-
211	1.7565	1.747
220	1.675	1.634
002	1.593	1.544
310	1.498	-
112	1.439	-
301	1.415	1.418

Table 6.3: d-spacing corresponds to standard SnO<sub>2</sub> lattice (PDF file No: 21-1250) and measured from TEM analysis

### 6.2.3.2 Thermally annealed SnO<sub>2</sub>:Sb

Spin coated SnO<sub>2</sub>:Sb sample, thermal annealed at 700<sup>0</sup>C for ~1hr has been characterised by TEM to examine how the thermal annealing temperature affects the film morphology. Figure 6.8 displays the bright field and dark field TEM images of the thermally annealed films.

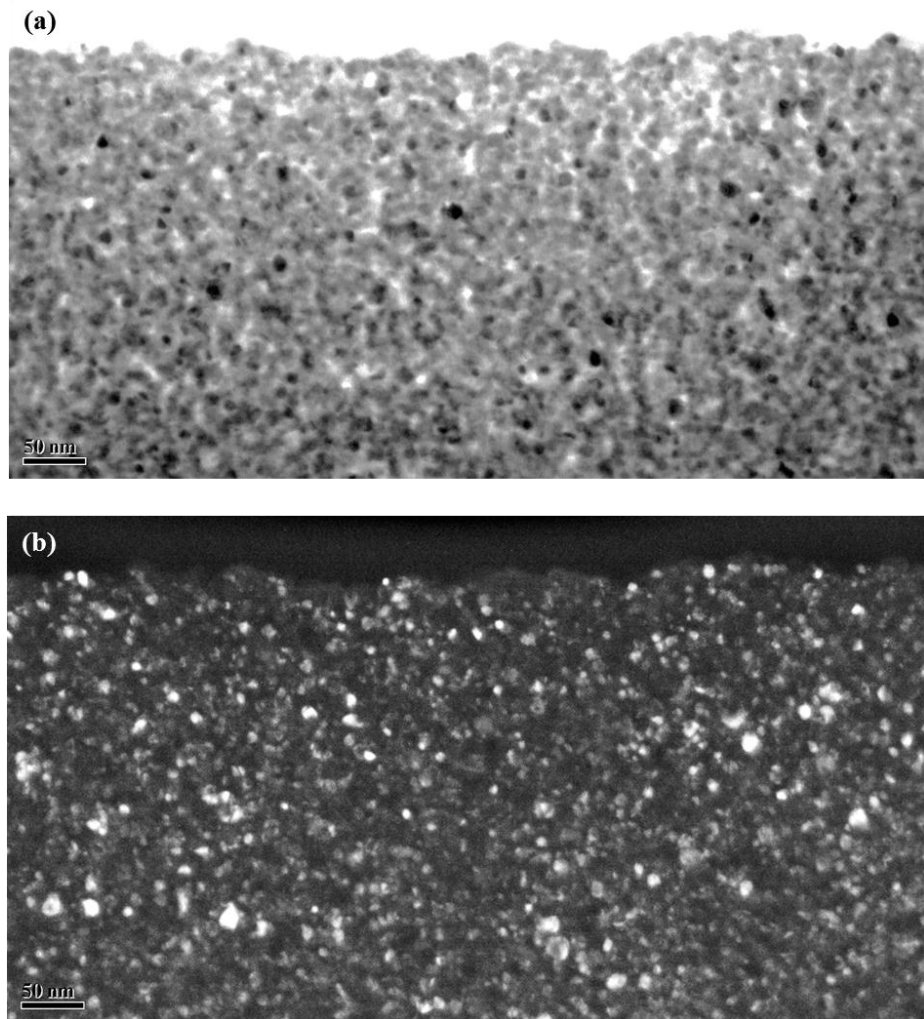


Figure 6.8 : Cross sectional TEM of SnO<sub>2</sub>:Sb thermal annealed at 700<sup>0</sup>C (a) Bright field (b) Dark field

As shown in figure 6.8 the film thermally annealed at 700<sup>0</sup>C has grain size distribution of 6 to 12 nm. Some isolated grains as large as 20 nm were also can be identified. This

film also shows a higher pore content compared to the as-deposit film, indicating that annealing has promoted coarsening of the pores. The electron diffraction patterns confirm the presence of tetragonal SnO<sub>2</sub>:Sb structure in both films. These findings were agreed with the XRD analysis as it shows crystalline size of 9 nm for thermally annealed films at 700°C.

### 6.2.3.3 Excimer laser processed SnO<sub>2</sub>:Sb

Figure 6.9 shows the TEM image of the KrF laser processed SnO<sub>2</sub>:Sb sample. This sample was laser irradiated at 60 mJ.cm<sup>-2</sup> for 1000 pulses.

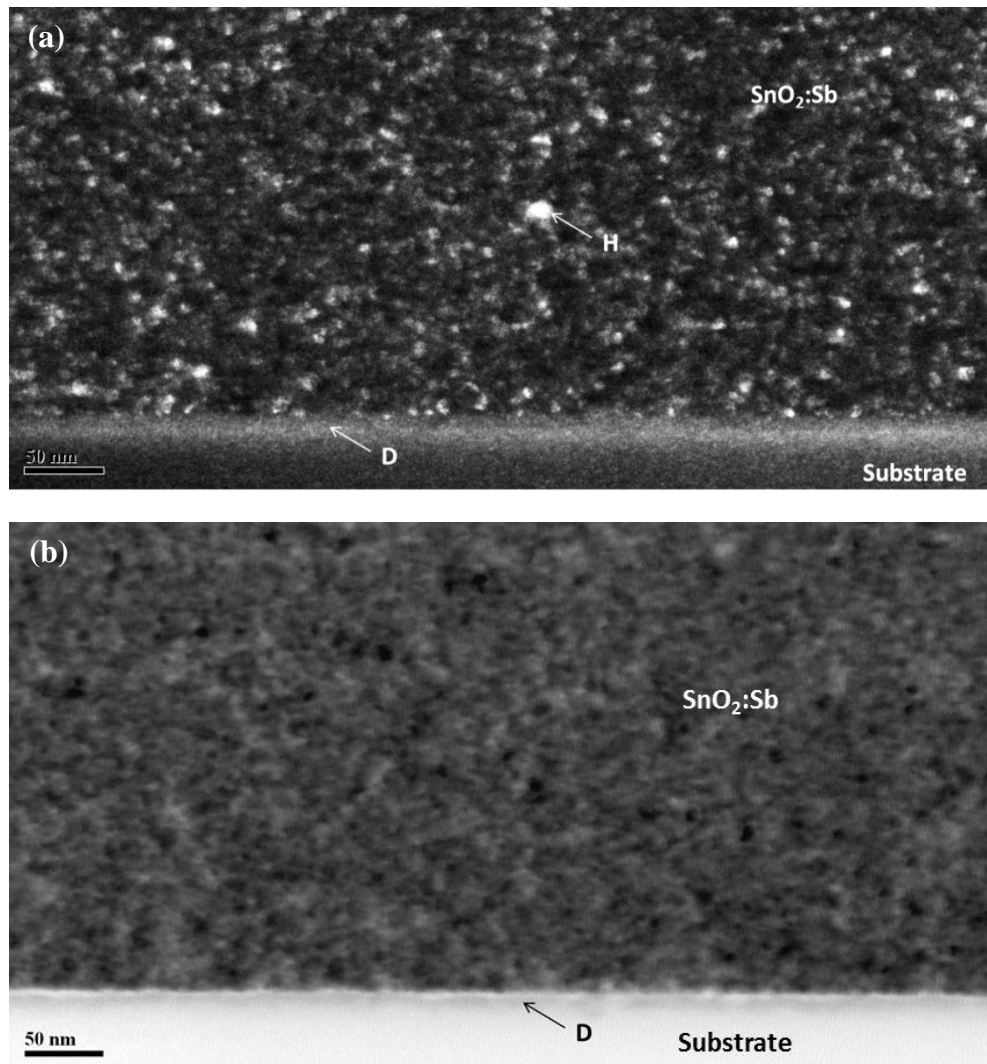


Figure 6.9 : TEM images of the lower surface region of KrF laser processed SnO<sub>2</sub>:Sb at 60 mJ.cm<sup>-2</sup>, 1000 pulses (a) Dark field (b) Bright field

The average grains size of the KrF laser processed films were about 6 to 10 nm. As shown in figure 6.9 (a) some localised grains as larger as 12 nm (marked at H) are also can identified. The porosity of the laser processed films appears to be coarser than the as-deposited films but not as quite as in the thermal annealed at 700<sup>0</sup>C film. When laser processing at higher number of pulses, some vertical cracks or pore formation also observed.

Figure 6.9 (b) shows the lower surface region of the SnO<sub>2</sub>:Sb film which has been KrF laser processed at 60 mJ.cm<sup>-2</sup> in bright field mode. The area marked D gives some indication of increase in absorption contrast at the very upper surface of the glass substrate. This may be indicative of a build-up of Sb or Sn at the lower surface interface.

#### **6.2.4. Chemical composition and oxidation states**

Chemical composition and the oxidation states of the spin coated layers of as-deposited, thermal annealed, laser processed and combined processed SnO<sub>2</sub>:Sb thin films were examined by XPS. Via collaboration, a set of four samples was prepared and sent to Brunel University for XPS analysis. K&W spin coated SnO<sub>2</sub>:Sb samples were used for the experimentation with an average thickness of 1100 nm. The samples were examined in a VG Escacope 210 using a polychromatic AlK $\alpha$  source.

Prior to XPS characterisation, the samples were post processed with the optimum processing conditions at NTU. The sheet resistance and the transmission of the processed layers were also measured. The sample details along with their sheet resistance and transmission measurements are tabulated in Table 6.4.

Sample ID	Preparation	Sheet resistance (kΩ/sq)	Transmission at 550 nm (%)
NTU-1	As-deposited SnO <sub>2</sub> :Sb	282.5	86
NTU-2	Oven annealed at 700 <sup>0</sup> C for 1hour	0.126	82
NTU-3	KrF Laser processed (60 mJ/cm <sup>2</sup> , 1000 pulses)	60.7	79
NTU-4	Oven annealed at 400 <sup>0</sup> C for 1hour and KrF laser processed (at 60 mJ/cm <sup>2</sup> , 1000 pulses)	1.11	81

Table 6.4: Sample details of the XPS analysed spin coated SnO<sub>2</sub>:Sb

The complete XPS survey scan spectra of as-deposited, thermal annealed, laser processed and combined processed SnO<sub>2</sub>:Sb are shown in figure 6.10 to figure 6.13. Peaks corresponding to the C, O, Sn and Sb can be observed in these spectra. Carbon C1s peak is at 284.6 eV while Oxygen O1s peak is at 531.7- 531.9 eV.

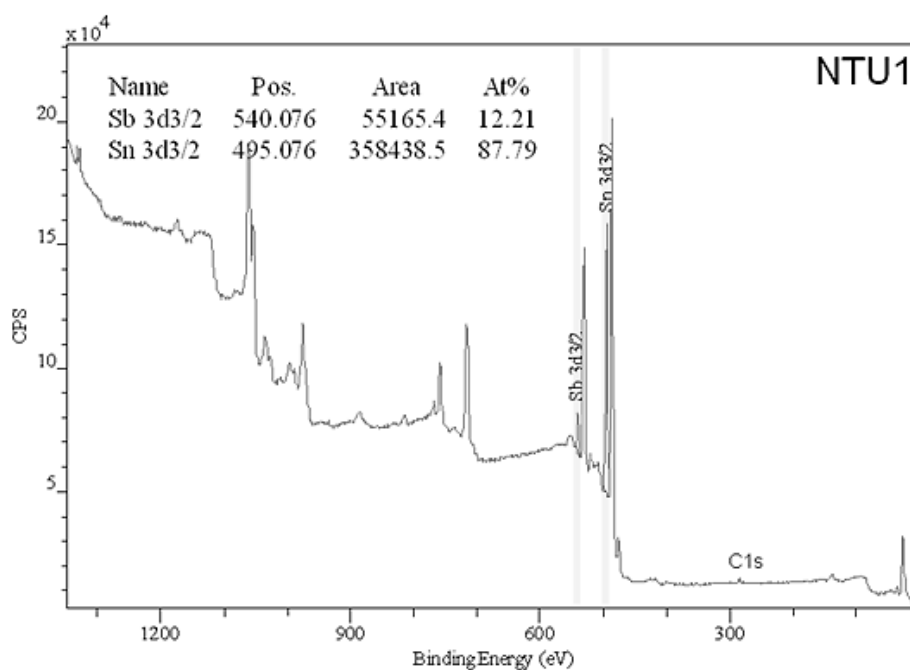


Figure 6.10: Complete XPS spectrum of as-deposited SnO<sub>2</sub>:Sb (NTU-1)

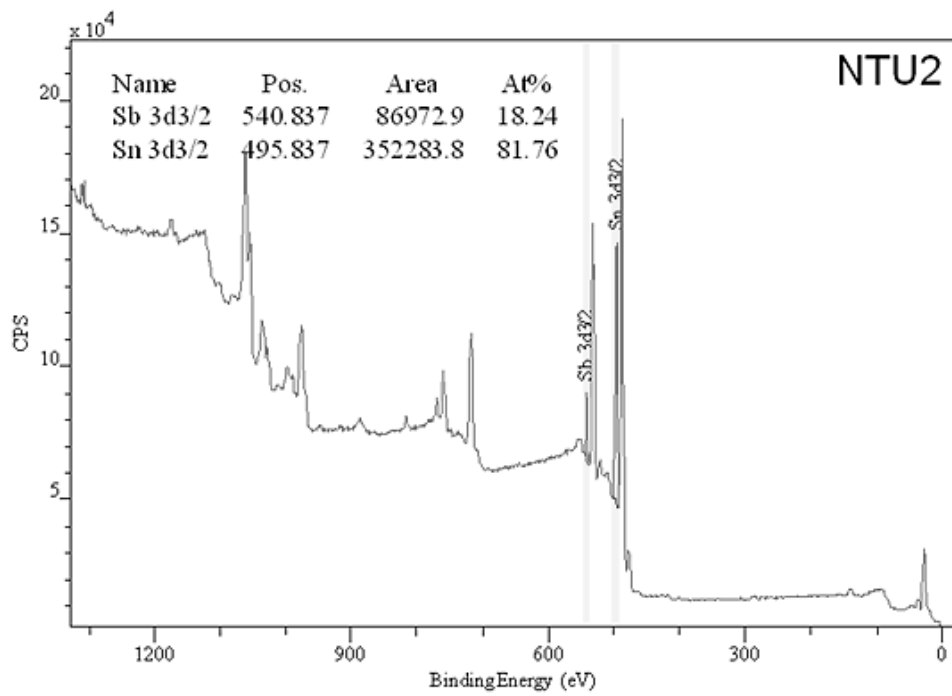


Figure 6.11: Complete XPS spectrum of thermal annealed SnO<sub>2</sub>:Sb at 700°C (NTU-2)

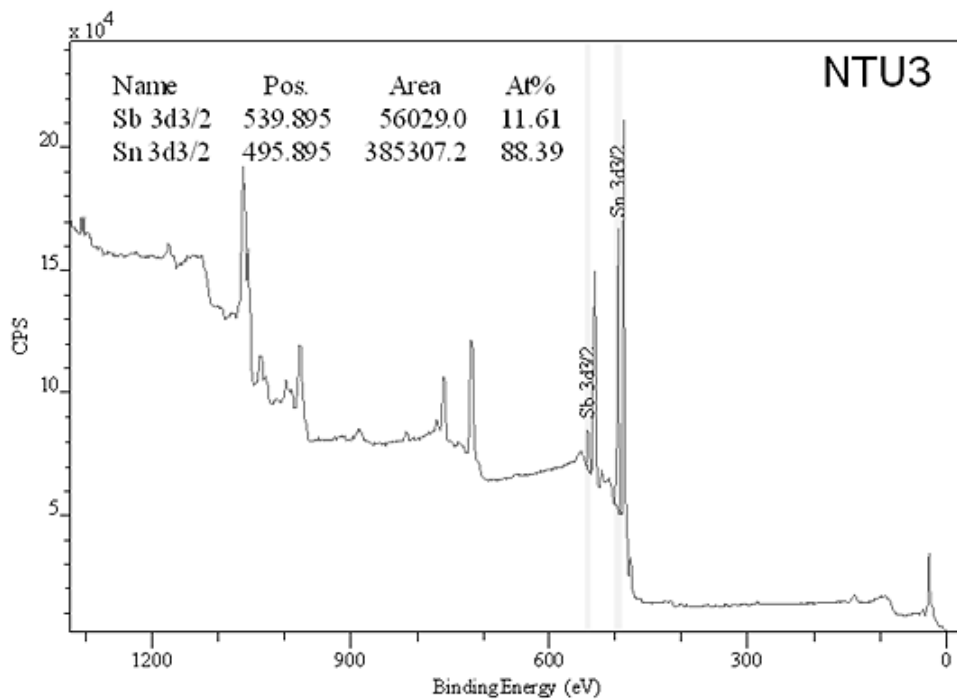


Figure 6.12: Complete XPS spectrum of the excimer laser processed SnO<sub>2</sub>:Sb (NTU-3)

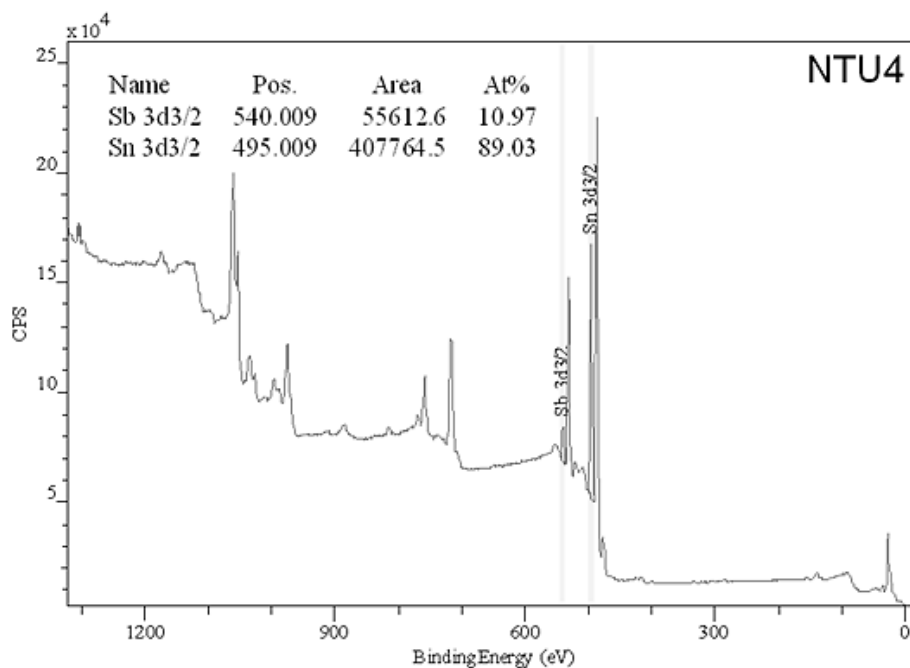


Figure 6.13: Complete XPS spectrum of the combined processed SnO<sub>2</sub>:Sb (NTU-4)

Table 6.5 summaries the percentages of Sb and Sn found in the surface of the samples. These percentages were corrected for the relative sensitivity of the two elements in XPS. The relative peak area of [Sb<sup>3+</sup>] is expressed as peak area of [Sb<sup>3+</sup>] in each sample area with respect to the peak area of [Sb<sup>3+</sup>] found in as-deposited sample. Due to the overlapping of O1s and Sb 3d<sub>5/2</sub> lines, the Sb 3d<sub>3/2</sub> line was used to calculate the percentage of Sb.

Sample ID	Peak area of Sn(%) [495 eV]	Peak area of Sb (%) [540 eV]	Relative peak area [Sb <sup>3+</sup> ]
NTU-1	87.8	12.2	1
NTU-2	81.8	18.2	1.49
NTU-3	88.4	11.6	0.95
NTU-4	89.0	11.0	0.89

Table 6.5: Sample details of the XPS analysed spin coated SnO<sub>2</sub>:Sb . The relative peak area is defined as a ratio of [Sb<sup>3+</sup>] in each sample area and [Sb<sup>3+</sup>] found in as- deposited sample.

Data in Table 6.5 indicates that the post processing method influenced the surface Sb percentage of SnO<sub>2</sub>:Sb samples. The sample thermal annealed at 700<sup>0</sup>C shows a higher percentage of Sb at the surface compared to the as-deposited sample, while the KrF laser processed and combined processed samples show a reduced percentage of Sb in the surface. The increase of the Sb percentage in the thermal annealed sample can potentially be explained as a segregation of Sb to the surface due to the annealing process. In contrast, the laser processed samples appear to show a depletion of the Sb dopant in the near-surface region. These findings may indicate that there has been some migration away from the surface, in which case, the higher electron absorption region observed at the substrate by TEM (figure 6.9) indicate an enriched Sb region at the lower surface. This effect was only observed by TEM for the laser processed samples. Interestingly, Spannhake et al [24] also reported similar depletion of Sb in the SnO<sub>2</sub>:Sb films from the near surface region which relates to thermally activated out-diffusion of the SnO<sub>2</sub>:Sb layers when they were thermal annealed at 1050<sup>0</sup>C or higher temperatures. There is evidently an effect here that is related to the annealing method used, and potentially to the resultant ionic substitution, as indicated by the variation in lattice cell volume by XRD.

### **6.3 Some thoughts on the conduction mechanism of spin coated SnO<sub>2</sub>:Sb**

The proposed conduction mechanism of SnO<sub>2</sub>:Sb has been discussed in the literature [115-118]. Among these reports, Zhang et al [69] suggested that ionized impurity scattering and the neutral impurity scattering are the dominant limitations for spray pyrolysis films, while Stjerna et al [119] suggested that ionized impurity scattering is the strongest, but there is a contribution from grain boundary scattering also for their RF reactive magnetron sputtered films. The author was not aware of published work relating to conduction mechanism analysis of laser processed SnO<sub>2</sub>:Sb and therefore this section will consider the conduction mechanisms of laser processed SnO<sub>2</sub>:Sb by reference to the prior work.

As previously explained in section 2.1.4, the key scattering mechanisms limiting the electrical conduction of a TCO are grain boundary scattering, ionized impurity

scattering and the neutral impurity scattering. However for polycrystalline films such as spin coated SnO<sub>2</sub>:Sb films, the conduction mechanism is governed by the carrier concentration of the films [28]. For carrier concentrations of less than 10<sup>18</sup> cm<sup>-3</sup>, conduction is mainly limited by grain boundaries while between 10<sup>18</sup> and 10<sup>19</sup> cm<sup>-3</sup>, conduction is dominated by grain boundaries and bulk properties. For the films with carrier concentration higher than the 10<sup>19</sup> cm<sup>-3</sup> different conduction factors are possible [120,28].

In general for the polycrystalline films with small crystalline sizes, grain boundary scattering dominates the electronic conduction mechanism. However, for this to be the case, the mean free path has to be of the same order as the crystalline sizes.

The mean free path of the charge carriers has been estimated by using the following relation;

$$l = \left(\frac{h}{2e}\right) \left(\frac{3N}{\pi}\right)^{1/3} \mu \quad \text{Eq 6.4}$$

Where  $l$  is the mean free path and  $N$  and  $\mu$  are the carrier concentration and carrier mobility respectively.

The estimated mean free path for thermal annealed and laser processed films are tabulated in Table 6.6 while the typical mobility and carrier concentration variation for laser processed, thermal annealed and as-deposited spin coated SnO<sub>2</sub>:Sb films are shown in figure 6.11 along with the theoretical ionized impurity curve deduced from Eq 2.18.

Preparation	Carrier mobility (cm <sup>2</sup> V <sup>-1</sup> s <sup>-1</sup> )	Mean free path (nm)
As- deposited	1.77	1.93
Thermal annealed at 200 <sup>0</sup> C	0.15	0.57
Thermal annealed at 400 <sup>0</sup> C	0.7	5.51
Thermal annealed at 700 <sup>0</sup> C	2.32	29.3
KrF laser processed at 20 mJ/cm <sup>2</sup>	0.54	0.86
KrF laser processed at 40 mJ/cm <sup>2</sup>	0.21	0.44
KrF laser processed at 60 mJ/cm <sup>2</sup>	0.04	0.23

Table 6.6 : Estimated carrier mobility and mean free path of spin coated SnO<sub>2</sub>:Sb

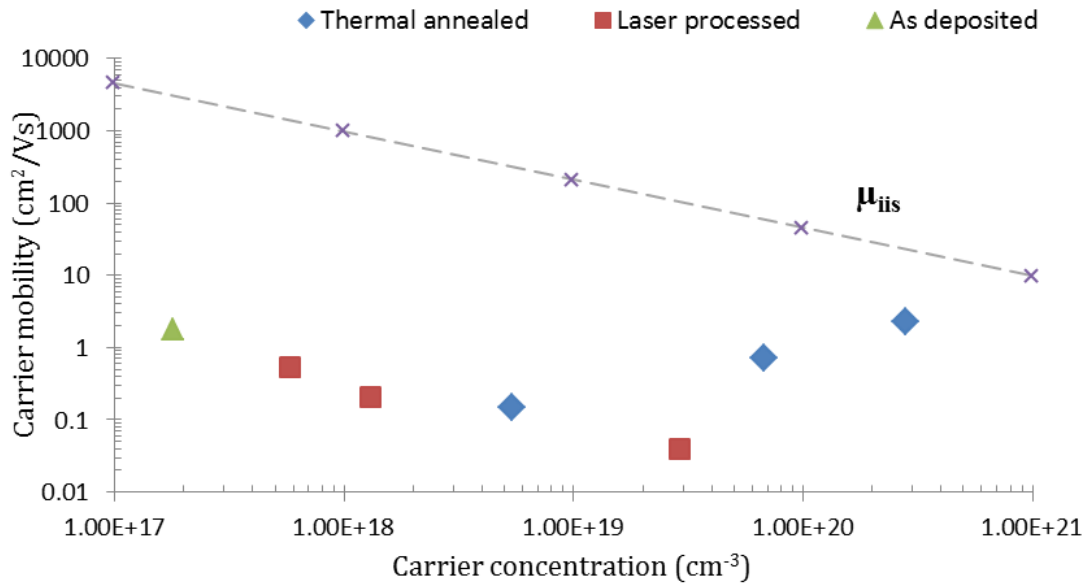


Figure 6.14: Mobility vs. carrier concentration for SnO<sub>2</sub>:Sb films: experimental values for thermal annealed, laser processed and as-deposited films, and theoretical mobility due to ionized impurity scattering-μ<sub>iis</sub> (dashed line)

From the calculated mean free path values it is clear that the conduction of the as-deposited and laser processing films is mainly dominated by grain boundary scattering. Also, when films are thermal annealed at fairly low temperatures ( $< 400^{\circ}\text{C}$ ) the grain boundary scattering dominates the conduction.

However, according to the theoretical mobility-carrier concentration relationship due to ionized impurity scattering, the conduction of films thermal annealed at  $700^{\circ}\text{C}$  films are dominated by both grain boundary scattering and ionized impurity scattering mechanisms, and as the thermal annealing temperature increases, the experimental data tends more towards the mobility due to ionized impurity scattering, as shown in figure 6.14.

## **6.4 Key findings and summary**

This chapter considered the electrical, optical, structural and chemical properties of as-deposited, thermal annealed and excimer laser processed SnO<sub>2</sub>:Sb films deposited by the spin coating technique, using films that were processed using the optimum post processing conditions identified by the work presented in chapter 5.

The key findings relating to as-deposited, thermal annealed and laser processed films are summarized as follows;

### **6.4.1. As-deposited SnO<sub>2</sub>:Sb**

It has been found that the as-deposited SnO<sub>2</sub>:Sb layers have banded morphology with grain size distribution of 3 to 7 nm. These films are polycrystalline and the XRD analysis confirms the (110) phase of SnO<sub>2</sub> is the preferred orientation. The mobility and carrier concentration of the as-deposited 1100 nm thick SnO<sub>2</sub>:Sb films were around  $1.7 \text{ cm}^2 \text{ V}^{-1} \text{ s}^{-1}$  and  $10^{17} \text{ cm}^{-3}$  respectively. The optical band gap of the as-deposited films is around 3.9 eV and as the mean free path of these films are in the same order as crystalline sizes, and therefore grain boundary scattering is considered to dominate the conduction mechanism.

#### 6.4.2. Thermal annealed SnO<sub>2</sub>:Sb

For the spin coated SnO<sub>2</sub>:Sb films thermal annealed at 700<sup>0</sup>C , TEM analysis confirms some grain growth compared to as-deposited layers, with the average grain distribution of these films at around 6 to 12 nm. With respect to the thermal annealing temperature, carrier mobility and carrier concentration are increased and when the films are thermal annealed at 700<sup>0</sup>C , carrier concentrations as high as 10<sup>20</sup> cm<sup>-3</sup> were obtained. This may be attributed to an improvement of crystallinity and growth of crystallite sizes that reduces the density of crystallite boundaries and weakens inter-crystallite boundary scattering [121].

No obvious variation in the optical band gap was obtained with the increase of thermal annealing temperature, but the XPS studies shows higher percentage of Sb in the top surface suggesting some segregation of Sb with the higher thermal annealing temperature. At lower annealing temperatures, the conduction mechanism of these films is considered to be mainly dominated by grain boundary scattering but at the higher temperatures it may be inferred that ionized impurity scattering also prominent.

#### 6.4.3 Excimer laser processed SnO<sub>2</sub>:Sb

It has been found that excimer laser processing consistently reduces the sheet resistance of spin coated SnO<sub>2</sub>:Sb films with increased number of laser pulses and laser fluences. The carrier concentration of these films increases with the increase of laser fluence, and for the optimum processed conditions, carrier concentrations up to 10<sup>19</sup> cm<sup>-3</sup> were obtained. These values are of the same order as the films thermal annealed at 400<sup>0</sup>C . The improvement of carrier concentration with laser fluences can be ascribed to the substitution of Sn<sup>4+</sup> atoms in the SnO<sub>2</sub> lattice by Sb<sup>5+</sup>, resulting in generation of conduction electrons and thus increase the carrier concentration. These findings were supported by the cell volume calculations where laser processed films shows less volume compared to the as-deposited films because of ionic radius of Sn<sup>4+</sup> (0.71 Å) is higher than the Sb<sup>5+</sup> (0.62 Å). However, as the laser fluence and number of laser pulses increases the carrier mobility decreases, which is attributed to the increase in scattering

of carriers. The optical transmission measurement shows some reduction of transmission with a higher number of laser pulses. Although the transmission at 550 nm was always greater than 70% for the all the processing conditions tested.

The optical band gap calculation of these films shows some shrinkage and then some expansion of the band gap with the increasing number of laser pulses. The shrinkage of optical band gap is possible with substitutional of Sb<sup>5+</sup> ions to the SnO<sub>2</sub> lattice. when a dopant with smaller ionic radii substitutes to the lattice the metal ns and oxygen 2p hybridization is weakened and thus the lattice compresses. This weak metal ns and oxygen 2p hybridization associated with strong structural relaxation around the dopant (Sb<sup>5+</sup>) with smaller ionic radius results the smaller optical band gap [32].

TEM analysis confirms the grain sizes of these films were around 6-10 nm. With the higher number of laser pulses some crack formation in the lower surface area is also noted.

It is concluded that the conduction in these films is mainly limited by grain boundary scattering, consistent with the crystalline sizes and the mean free paths being of the same order.

## 7. ACEL device fabrication and Characterisation

### 7.1 Introduction

This chapter explains the fabrication and characterisation techniques used to produce Alternating Current Electroluminescent (ACEL) Display devices. This work was carried out as a part of the FAB3D project in collaboration with Brunel University and Keeling Walker Ltd. SnO<sub>2</sub>:Sb layers were spin coated by Keeling and Walker Ltd and the author post processed the layers with the optimum post processed conditions as explained in chapter 6. The other layer depositions and the device characterisation work were conducted at Brunel University. Dr. Paul Harris at Brunel University is acknowledged for his assistance in ACEL device fabrication and characterisation.

### 7.2 Alternating Current Electroluminescent (ACEL) Display devices

#### 7.2.1. Introduction

Depending on the device architecture and the emission mechanism there are four types of inorganic electroluminescent(EL) devices: AC thin film EL, AC powder EL, DC thin film EL and DC powder EL. In contrast to the luminescence principle of light emitting diodes, where electron-hole recombination occurs at  $p-n$  junctions, DC and ACEL devices rely on high field injection and acceleration of electrons to induce luminescence. The powder EL and thin film EL devices are technologically very different to each other because the powder devices have thicker EL layers (of the order of tens of micrometres) containing particles of phosphor powders while the thin film EL devices have thinner EL layers (of the order of hundreds of nanometers) which are polycrystalline phosphor thin films [122]. The powder EL devices rely on injection from microstructure defects and typically operate at lower device electrical field strengths as compared to thin film EL devices, where tunnel injection occurs from trapping states at the thin film interface with surrounding insulating layers. This makes a considerable difference to the brightness-voltage curves of both displays where the

thin film EL devices shows a sharp threshold behaviour when the electrons are injected by tunnelling into the phosphor layer [22], while the powder EL devices show a gradual increase in brightness with increasing voltage. Therefore the thin film EL displays are a good candidate for matrix addressing in display devices. In contrast, one of the key benefits of powder ACEL devices is the fact that they can be fabricated using screen printing techniques and can use flexible substrates. However, they do suffer from shorter lifetimes than thin film EL devices [123], but due to the lower cost and large area capability, powder ACEL devices have been used in large area advertising and novel flexible applications, such as ambient lighting devices [124, 125]

The powder EL devices are also have the drawback of shorter lifetime and are usually used as backlight for liquid crystal displays in watches and similar devices, and for displays where shorter lifetime is acceptable

### **7.2.2. Device structure and operation of ACEL**

The basic concept of the ACEL device is an EL layer, consisting of powder ZnS, which is dispersed in a dielectric material and sandwiched between two electrodes (with one electrode being transparent). The typical structure of an AC powder EL device is shown in figure 7.1. The particle size of the phosphor powder is usually in the order of 5 to 20  $\mu\text{m}$  and the thickness of the EL layer is around 50 to 100  $\mu\text{m}$ . The dielectric material can be an organic material with relatively high dielectric constant or glass with a low melting point. Typically, ITO is used as the transparent electrode and glass or flexible plastic used as the substrate. An insulating layer is used to protect the EL device against dielectric breakdowns and often  $\text{BaTiO}_3$  powder dispersed in another dielectric material is used as insulating layer.

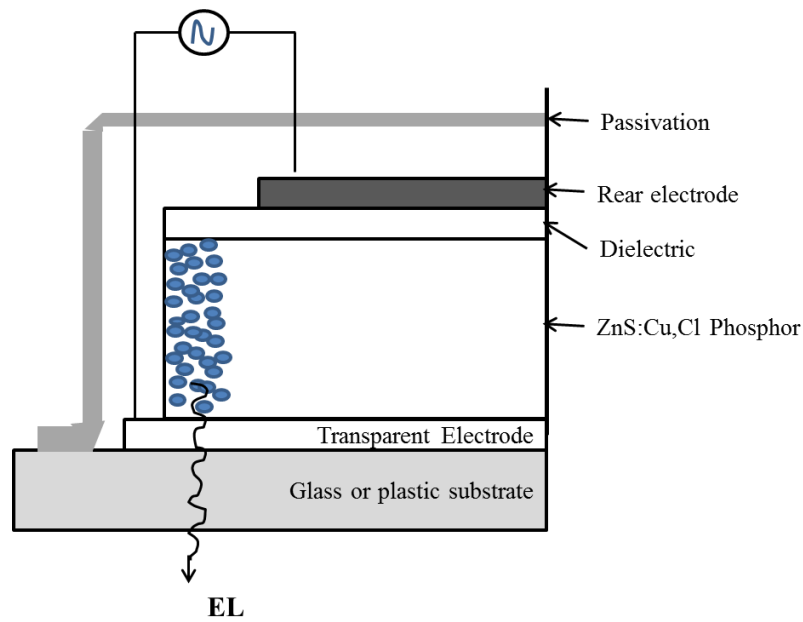


Figure 7.1: Structure of typical AC powder EL device [126]

When applying an AC voltage of about 100 - 200V, which corresponds to the electric field of the order of  $10^4 \text{ Vcm}^{-1}$  between the transparent front and reflecting rear electrodes, electroluminescence can be observed in these devices. The dependence of the luminescence ( $L$ ) on the applied voltage can be expressed by [126];

$$L = L_0 \exp \left[ - \left( \frac{V_0}{V} \right)^{1/2} \right] \quad \text{Eq 7.1}$$

Where  $L_0$  and  $V_0$  are depends on particle size of the phosphor, concentration of the powder in the dielectric, dielectric constant of the embedding medium and the device thickness.

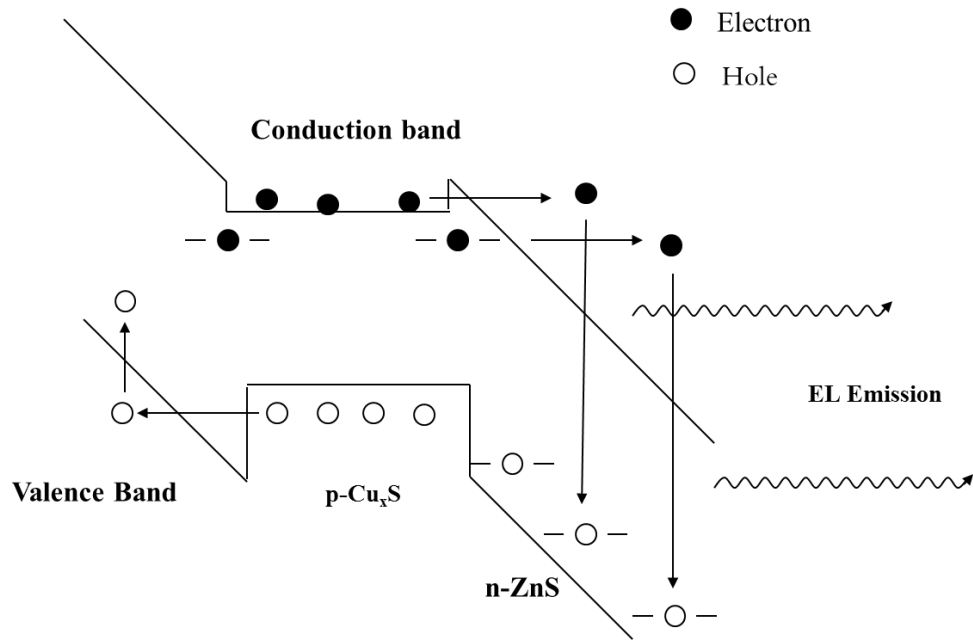


Figure 7.2 : Schematic energy band diagram of AC powder EL devices. Reproduced from [127]

The powder phosphor preparation involves firing of ZnS powders at high temperatures and subsequent cooling. When fired at high temperature, EL powders have a hexagonal structure which after further cooling transforms to cubic structure. During this transformation, Cu dopant preferentially precipitates on defects in ZnS particles and form embedded  $\text{Cu}_x\text{S}$  needles [123].

Once a sufficient electric field is applied between electrodes, these needles can induce tunnelling of electron-hole pairs as shown in figure 7.2. The holes are trapped by Cu recombination centres and once the field is reversed the emitted electrons recombine with the holes to produce light.

In terms of the transparent conductor material used in the flexible ACEL devices, carbon nanotubes [128], poly(3,4-ethylenedioxythiophene): poly(styrenesulfonate) (PEDOT:PSS) [129], ZnO and  $\text{SnO}_2$  are of interest as alternatives to ITO. Kim et al [130] reported on the use of Zr-doped ZnO (ZZO) as an alternative to ITO and materials were deposited on to glass substrates by pulsed laser deposition. The use of carbon nanotubes (CNT) [131] was reported as the front electrode on flexible ACEL devices on

polyethylene terephthalate (PET) substrates and it was reported that these devices showed a brightness of  $96.8 \text{ cd.m}^{-2}$  at 28 kHz and 50 V.

In this research work, the application of solution processed  $\text{SnO}_2\text{:Sb}$  was proposed as a potential transparent electrode layer for ACEL devices, hence to investigate this, several ACEL lamps were fabricated by use of spin coating and post processed  $\text{SnO}_2\text{:Sb}$ , using the optimum post processing conditions.

### **7.3 ACEL device fabrication**

The main aim of this section is to assess the feasibility of using the spin coated  $\text{SnO}_2\text{:Sb}$  layers as transparent electrodes for ACEL devices. Hence, for these devices post processed  $\text{SnO}_2\text{:Sb}$  was used as the transparent electrode, while copper doped zinc sulphide ( $\text{ZnS:Cu}$ ) and Silver (Ag) was used as the light emitting and back electrode respectively. Glass was used as the substrate and the transparent electrode was spin coated onto the glass substrate. The other layers were deposited by the screen printing technique.

#### **7.3.1. Post processing of transparent electrode layer**

The spin coating technique was used to deposit the  $\text{SnO}_2\text{:Sb}$  layers on to  $50 \times 50 \text{ mm}^2$ , Eagle XG glass substrates as the front electrode for ACEL devices. The thickness of the deposited layers was 1100 nm. Post processing and characterisation of the transparent electrode was conducted at NTU by the author.

The post processing conditions used to functionalised the  $\text{SnO}_2\text{:Sb}$  transparent electrode layers are summarised in Table 7.1. Thermal annealing, laser processing and combined processing techniques were used for functionalization of transparent electrode layers.

Device ID	Annealing technique of transparent electrode
NTUATOD-1	Thermal annealed at 400 <sup>0</sup> C for 1hr then KrF Laser processed (60 mJ/cm <sup>2</sup> , 1000 pulses)
NTUATOD-2	Thermal annealed at 150 <sup>0</sup> C for 2hr then KrF Laser processed (60 mJ/cm <sup>2</sup> , 1000 pulses)
NTUATOD-3	KrF Laser processed (60 mJ/cm <sup>2</sup> , 1000 pulses)
NTUATOD-4	Thermal annealed at 700 <sup>0</sup> C for 1hr

Table 7.1: Post annealing conditions of ACEL transparent electrode.

The NTUATOD-1 and NTUATOD-2 layers were initially thermal annealed at 400<sup>0</sup>C and 150<sup>0</sup>C for 1hr and 2hr respectively. Then these layers were KrF laser processed with the NTUATOD-3 layer. For comparison, the NTUATOD-4 layer is only thermal annealed at 700<sup>0</sup>C for 1 hr. The excimer laser processing system used for this work usually gives beam spot of 1.3 x 1.3 cm<sup>2</sup> area, which is not sufficient for device fabrication over the larger area. Therefore, large area laser processing was achieved by processing adjoining areas. For the ACEL electrodes, 4 x 4 cm<sup>2</sup> area was laser processed by processing nine areas as shown in figure 7.3. The X-Y translation stage associated with the excimer laser system was used to accurately position the sample area.

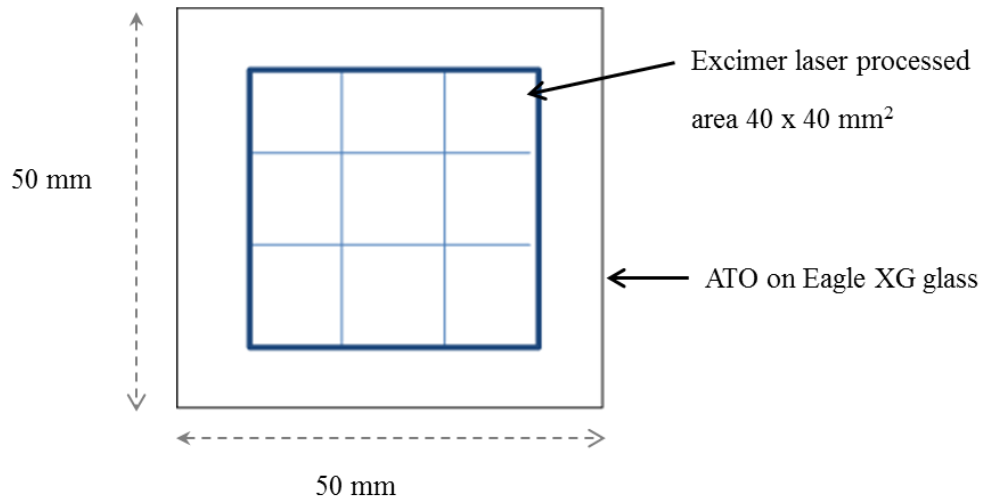


Figure 7.3: Dimensions of the excimer laser processed transparent electrode for ACEL devices

Further to processing, the sheet resistance and the transmission of the processed areas were measured. Four point probes were used to measure the sheet resistance of the transparent electrodes, while the transmission was measured by using Filmetrics spectrometer as explained in section 3.4.1.

Device ID	Sheet resistance (K $\Omega$ /sq)	Transmission at 550 nm (%)
NTUATOD-1	$0.86 \pm 0.2$	78%
NTUATOD-2	$13.1 \pm 1.3$	75%
NTUATOD-3	$26.6 \pm 4.6$	75%
NTUATOD-4	$0.12 \pm 0.03$	81%

Table 7.2 : Sheet resistance and optical transmission variation of spin coated and functionalised SnO<sub>2</sub>:Sb layers.

Table 7.2 summarises the sheet resistance and transmission of spin coated SnO<sub>2</sub>:Sb layers used as transparent electrodes.

### 7.3.1. Fabrication of other layers

As shown in figure 7.1, ACEL device is fabricated by sandwiching EL and dielectric layers between transparent and the back electrodes. The EL and back electrode for these devices were deposited by at Brunel University and the fabrication process is briefly summarised here.

Green emitting ZnS:Cu phosphor powder from Global Tungsten and Powders (GTP) was used to produce the emissive/dielectric binder ink. This ink consisted of ZnS:Cu powder in a solvent borne resin and filled with Barium titanate (BaTiO<sub>3</sub>) to increase the dielectric constant of the binder system and hence to improve the brightness of the ACEL devices. This binder ink was directly applied onto the functionalised transparent electrode (SnO<sub>2</sub>:Sb) by a screen printing technique. Further to deposition the layers are dried at 120<sup>0</sup>C for 15 mins to remove the solvents from the ink.

AG-500 silver filed electrically conductive ink from Nicomatic Ltd, UK was screen printed onto the back of the EL binder layer to form the back electrode. Further to deposition this layers are dried at 148<sup>0</sup>C for up to 30 mins to remove all the residual solvents.

## 7.4 ACEL device characterisation

Further to device fabrication, the devices were driven with an AC waveform and the spectral output was measured to compare the performances. Specifically, a Jeti Specbos 1200 spectroradiometer was used to record the luminance output and the devices were operated by applying an AC sinusoidal voltage waveform at frequencies of 400 Hz and 800 Hz respectively. The spectral output of the device based on sample NTUATOD-3 (the transparent electrode-KrF laser processed only) was not possible to record, so the luminance output of the other three devices are compared here.

Figure 7.4 (a) & (b) shows the luminance (L) as a function of applied RMS voltage (V) for EL devices when driving at 400 Hz and 800 Hz respectively. The luminescence vs. voltage (L-V) curves features a threshold voltage ( $V_{TH}$ ) of around 30 V, below which little light is emitted, and above this value the luminance increases with the applied voltage because of increased transferred charge in the phosphor/dielectric bi layer.

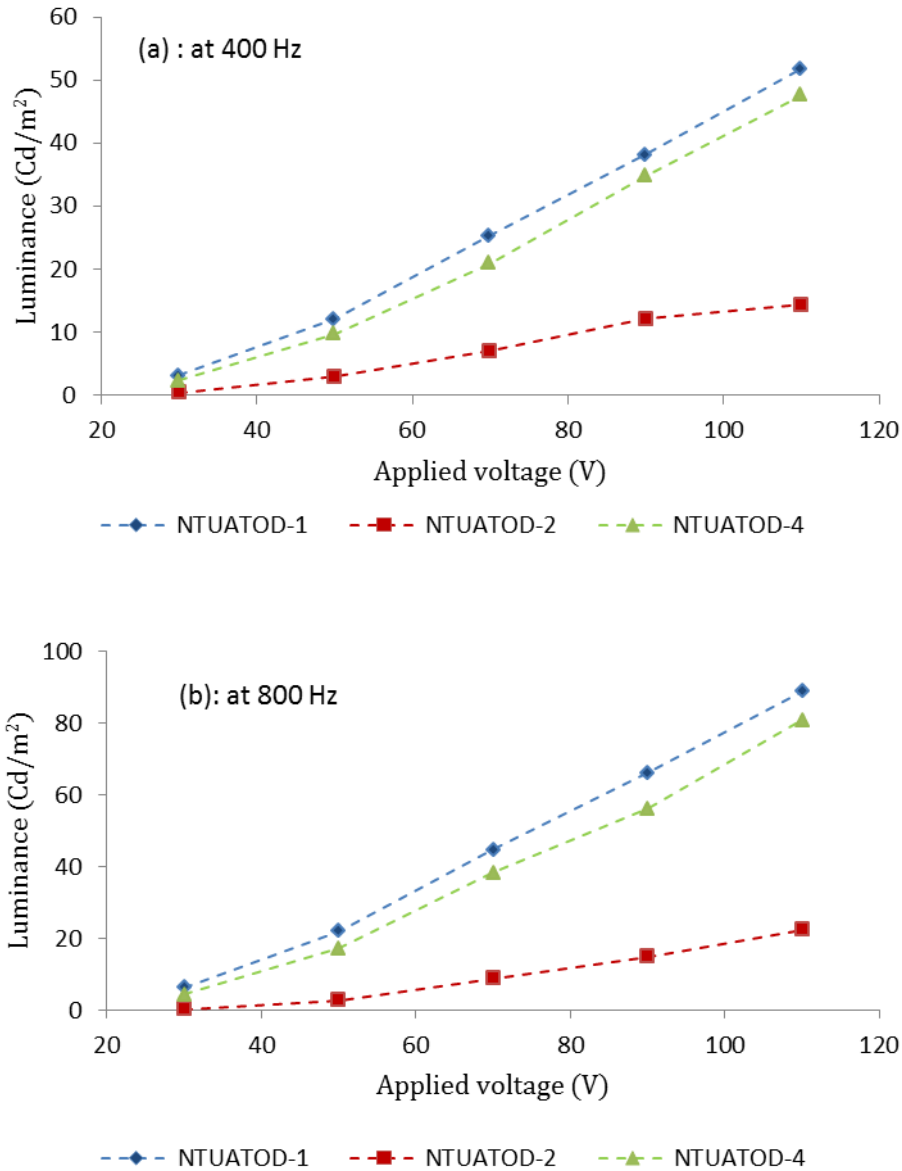


Figure 7.4 : Luminescence as a function of applied RMS voltage for ACEL devices fabricated with SnO<sub>2</sub>:Sb as transparent electrode drive at (a) 400 Hz (b) 800 Hz

For the both driving frequencies tested, the devices NTUATOD-1 and NTUATOD-4 showed same order of luminescence with the increase of applied voltage. Hence, the combined processing of low temperature thermal annealing (400<sup>0</sup>C ) followed by laser treatment gives the same order of performance as a transparent conductor for these devices as the high temperature (700<sup>0</sup>C ) processed devices. This highlights how the combination of thermal and laser processing can be used to effectively reduce the processing temperatures required to achieve functional electrodes for these type of devices. Figure 7.5 shows a photograph of the fabricated ACEL device with combined processed SnO<sub>2</sub>:Sb front electrode.

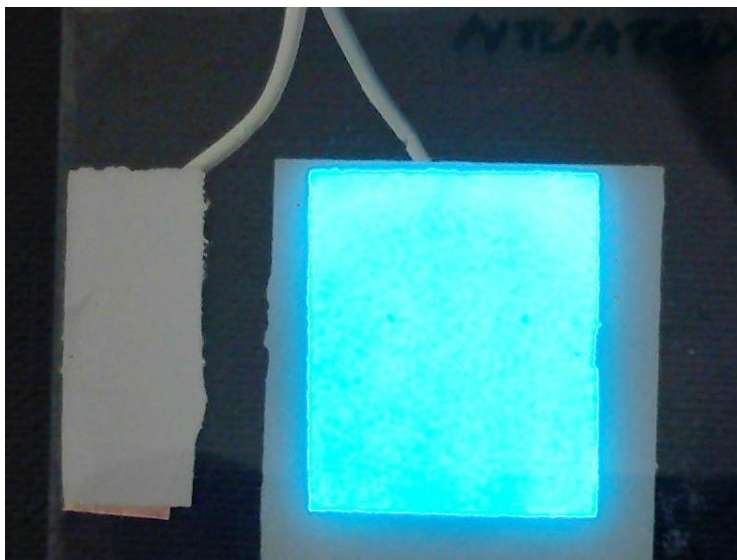


Figure 7.5 : ACEL device fabricated with spin coated and combined processed SnO<sub>2</sub>:Sb front electrode.

## 7.5 Discussion

This chapter summarises the results of an investigation into the use of low temperature processing techniques to optimise the electrical and optical properties of spin coated SnO<sub>2</sub>:Sb thin films for use in electroluminescent display devices. For comparison, ACEL devices were fabricated by thermal annealing, laser processing and combined processing of SnO<sub>2</sub>:Sb layers to use as transparent electrodes.

For all the devices tested, the transparent electrode was spin coated with the other layers screen printed. Luminescence studies shows the device which transparent electrode thermal annealing at 400<sup>0</sup>C and then laser processed shows similar brightness as the higher temperature, 700<sup>0</sup>C thermally annealed device. This is a vital step forward with potential industrial applications to fabricate low processing temperature of the display devices, especially on flexible substrates.

## **8. Conclusions and Future work**

### **8.1 Conclusions**

The aim of this research work was to investigate the use of photonic processing as a potential post processing technique to functionalise solution based nanoparticulate layers suitable for optoelectronics applications. For this research work, SnO<sub>2</sub>:Sb was selected as the TCO material of choice to investigate for potential use as transparent electrodes in ACEL displays. Via collaboration, the SnO<sub>2</sub>:Sb films were deposited by three different solution based deposition techniques (i) Inkjet Printing (ii) Dip coating and (iii) Spin coating. Further to deposition, the films were post processed to investigate the effect on electrical, optical and structural properties. Excimer laser processing was used to functionalise the SnO<sub>2</sub>:Sb films at low temperature. For comparison, thermal annealing was studied and the combined processing of thermal plus laser processing of SnO<sub>2</sub>:Sb was also discussed as a potential low temperature post processing method to functionalise the materials.

The functionalized films were then utilised for completion of a series of trial low cost, low temperature ACEL display demonstrators. The work presented in this thesis demonstrated that the luminescence of the ACEL devices fabricated by using combined processed transparent electrodes shows similar performance, in terms of electro-optical behaviour as the devices produced with high temperature thermal processed transparent electrodes.

A summary of the main research findings is as follows;

Via collaboration, the SnO<sub>2</sub>:Sb aqueous dispersions were formulated and a range of samples were dip coated to evaluate the material as a thin film. The thickness of the dip coated SnO<sub>2</sub>:Sb films were around 950 nm and the films were deposited onto Eagle 2000 glass substrates. The Initial sheet resistance of these films was around 1 MΩ/sq and the optical transmission at 550 nm was at 90%. Further to excimer laser processing, the sheet resistance of these layers was reduced to 200 kΩ/sq while the sheet resistance

of the films thermal annealed at 700<sup>0</sup>C was reduced to 360 Ω/sq. It has been shown through XRD characterisation that with the number of laser pulses, the crystallinity improves and hence reduces the sheet resistance in the excimer laser processed films.

The aqueous dispersion of SnO<sub>2</sub>:Sb was then formulated as an ink to study inkjet printing of material. The inkjet printed SnO<sub>2</sub>:Sb films showed as-deposited sheet resistance of around 4 MΩ/sq, and exhibited poor surface quality due to the coffee ring effect. Subsequently some of the inkjet printed films were laser processed and further to laser processing the sheet resistance was reduced to a factor of four. Several studies were conducted to minimize the coffee ring effect and improve the jetting and the substrate wetting of the inkjet printing. However, due to lack of consistency of the films and the difficulty in controlling deposition and/or printing processes, alternative solution based deposition techniques were considered.

Via collaboration, spin coated SnO<sub>2</sub>:Sb films were successfully deposited onto the Eagle XG glass substrates. This process provided consistent films to study the effect of laser processing and annealing on electrical and optical properties. Multiple layer SnO<sub>2</sub>:Sb films were studied to optimise the layer thickness. Following KrF and ArF laser processing of the spin coated SnO<sub>2</sub>:Sb films resulted in a reduction of sheet resistance to the tens of kΩ/sq range, from their as-deposited values of 400 kΩ/sq. while the optical transmission at 550 nm remained above 75%. Thermal annealing at 700<sup>0</sup>C of spin coated SnO<sub>2</sub>:Sb demonstrated a reduction of sheet resistance to 120 Ω/sq, but for all the lower temperature (<400<sup>0</sup>C) processed areas the measured sheet resistance was greater than 1 kΩ/sq. For all the thermal annealed films optical transmission at 550 nm remained over 80%.

As laser processing only did not result in sufficient reduction of sheet resistance of the SnO<sub>2</sub>:Sb to use as transparent electrodes for display applications, combined processing was considered. In this technique, films were initially thermal annealed at the lower temperature range (≤ 400<sup>0</sup>C) and then KrF laser processed. When SnO<sub>2</sub>:Sb films were thermal annealed at 400<sup>0</sup>C and then laser processing at 60 mJ.cm<sup>-2</sup> with 1000 laser pulses, the sheet resistance was reduced to less than 1 kΩ/sq while optical transmission was maintained at over 78%. XRD analysis showed some grain growth when thermal

processing the films at higher temperatures, but with the other processing conditions no significant grain growth was observed by XRD. The average crystalline size of the as-deposited SnO<sub>2</sub>:Sb was 6-7 nm.

The carrier concentration and Hall mobility of the as-deposited and post processed SnO<sub>2</sub>:Sb films were also studied. Further to thermal annealing and laser processing, the carrier concentration increased up to 10<sup>20</sup>cm<sup>-3</sup> and 10<sup>19</sup>cm<sup>-3</sup> respectively. For the laser processed films, the carrier concentration increases with the laser fluence while Hall mobility reduces. A different trend was observed for thermal annealed films where both the carrier concentration and mobility improves with respect to the annealing temperature.

For thermal annealed films, TEM analysis showed grain growth when films were processed at 700<sup>0</sup>C while XPS indicates a higher percentage of Sb in the top surface suggesting some segregation of Sb. TEM analysis showed some grain growth when films were KrF laser processed, but the improvement was not as prominent as with higher temperature thermal annealing.

It has been found that when films were thermal annealed at lower temperatures, grain boundary scattering limits the conduction mechanism but at the higher temperatures it may be inferred that ionized impurity scattering becomes prominent. Also it has been found that grain boundary scattering limited the conduction of laser processed films.

## **8.2 Future Work**

The proposed future work building on this study can be divided into two halves: improvement of processing and deposition techniques, and further analysis.

Although inkjet printing is a cost effective and high throughput process due to its efficient material use, it is always challenge to achieve good jetting and wetting characteristics. During this work it has not been possible to deposit consistent SnO<sub>2</sub>:Sb films by using the inkjet printing technique. Therefore it remains a great interest to

undertake further study in regard to ink rheology, droplet formation and drying processes to achieve consistent films with this material.

The aim of this study was to investigate the use of laser processing as a potential post processing technique to functionalise the solution based materials. This research work demonstrated that it has been possible to functionalise solution processed nanoparticle layers without utilising high temperature processes. Therefore it is significant to transfer these techniques to deposit materials onto flexible substrates to use in roll to roll manufacturing.

During this study the Sb concentration was kept constant, and the K&W Ltd standard SnO<sub>2</sub>:Sb dispersion was used. As the nature, quantity and structural distribution of the doping are important factors for electrical properties of TCOs it will be useful to study the electrical and optical properties of SnO<sub>2</sub>:Sb by varying the Sb doping concentration to optimise the doping.

As explained in section 2.5.2, photonic processing techniques such as Flash lamp curing are of interest to functionalise TCO materials. During this work some SnO<sub>2</sub>:Sb films were flash lamp annealed. However, as this is preliminary work relating to the flash lamp annealing of spin coated SnO<sub>2</sub>:Sb, further work is required to optimise the reproducibility and lamp parameters.

During this research work, different thicknesses of spin coated SnO<sub>2</sub>:Sb layers were deposited and the thicker layers were built up by applying the ink, spinning and air drying each layer before depositing the next consecutive layer. These layers are built of an alternating sequence of dense and porous regions. As explained in chapter 6, depending on the absorption coefficient of the material in question, the penetration depth associated with excimer lasers are <200 nm (at 248 nm). Therefore it would be of interest to study the effect of laser processing between consecutive layers instead of across the entire film following multilayer deposition. Hence, it may be possible to improve the electrical properties further by laser penetration through entire film, rather than the upper layers only – with the associated energy gradient.

In terms of further analysis, it would be useful to study the transmission spectra in the infrared region to accurately determine the plasma wavelength and the mass of free carriers (As explained in section 2.1.3.2). In addition, it would be useful to compute the dielectric function in the TCO using Drude's approach to estimate the electron density and mobility from the optical data.

Finally, although this research work has resulted completion of a series of ACEL display demonstrators which utilise the low cost, low temperature, laser processed SnO<sub>2</sub>:Sb thin films as transparent electrodes, it is also of interest to develop nanoparticulate ink and photonic processing techniques to optimise the other layers in these devices. Hence, to realise full solution processing and fabrication of display devices on flexible substrates.

## **List of References**

- [1] G. P. Crawford, *Flexible Flat Panel Displays*. John Wiley and Sons Ltd, 25 April 2005.
- [2] T. M. Lee, H. C. Choi, J. H. Noh and D. S. Kim, "EL display printed on curved surface," in *Micro Electro Mechanical Systems, 2009. MEMS 2009. IEEE 22nd International Conference on*, 2009, pp. 943-946.
- [3] S. H. Huang, P. Liu, A. Mokasdar and L. Hou, "Additive manufacturing and its societal impact: a literature review," *The International Journal of Advanced Manufacturing Technology*, pp. 1-13, 2012.
- [4] F. Garnier, R. Hajlaoui, A. Yassar and P. Srivastava, "All-Polymer Field-Effect Transistor Realized by Printing Techniques," *Science*, vol. 265, pp. 1684-1686, Sep 16. 1994.
- [5] Z. Bao, Y. Feng, A. Dodabalapur, V. R. Raju and A. J. Lovinger. High-performance plastic transistors fabricated by printing techniques. *Chemistry of Materials* 9(6), pp. 1299-1301. 1997.
- [6] M. Tredinnick, P. Barnwell and D. Malanga, "Thick film fine line patterning: A definitive discussion of the alternatives," in *SPIE Proceedings Series*, 2001, pp. 676-681.
- [7] S. I. Na, B. K. Yu, S. S. Kim, D. Vak, T. S. Kim, J. S. Yeo and D. Y. Kim, "Fully spray-coated ITO-free organic solar cells for low-cost power generation," *Solar Energy Mater. Solar Cells*, vol. 94, pp. 1333-1337, 2010.
- [8] S. L. Wilson, W. M. Cranton, R. M. Ranson, D. C. Koutsogeorgis, A. Mosley, C. B. Thomas, G. Boutaud, S. Wagland, E. A. Mastio, S. Lipiec, A. Spiller, j. Scott and S. Stoute, "P-169: Optimization of the electrical and optical properties of ink-jet printed SnO<sub>2</sub>:Sb using thermal annealing and excimer-laser processing," *SID Symposium Digest of Technical Papers* , vol 36, pp. 530-533, 2005.
- [9] Y. Marumoto, "Image Processing Apparatus, Printing Apparatus and Image Processing Method with Generation of Binary Data According to a Correspondence Relationship Defined by a Dot Arrangement", *US Patent US8154764 B2*, 2012.
- [10] A. Hancock and L. Lin, "Challenges of UV curable ink-jet printing inks-a formulator's perspective," *Pigment and Resin Technology*, vol. 33, pp. 280-286, 2004.

- [11] H. H. Lee, K. S. Chou and K. C. Huang, "Inkjet printing of nanosized silver colloids," *Nanotechnology*, vol. 16, pp. 2436, 2005.
- [12] P. Calvert, "Inkjet printing for materials and devices," *Chem.Mater*, vol. 13, pp. 3299-3305, 2001.
- [13] W. Yin, D. H. Lee, J. Choi, C. Park and S. M. Cho, "Screen printing of silver nanoparticle suspension for metal interconnects," *Korean Journal of Chemical Engineering*, vol. 25, pp. 1358-1361, 2008.
- [14] K. S. Chou, K. C. Huang and H. H. Lee, "Fabrication and sintering effect on the morphologies and conductivity of nano-Ag particle films by the spin coating method," *Nanotechnology*, vol. 16, pp. 779-784, 2005.
- [15] T. Y. Choi, D. Poulikakos and C. P. Grigoropoulos, "Fountain-pen-based laser microstructuring with gold nanoparticle inks," *Appl. Phys. Lett.*, vol. 85, pp. 13, 2004.
- [16] S. H. Ko, H. Pan, C. P. Grigoropoulos, C. K. Luscombe, J. M. J. Fréchet and D. Poulikakos, "All-inkjet-printed flexible electronics fabrication on a polymer substrate by low-temperature high-resolution selective laser sintering of metal nanoparticles," *Nanotechnology*, vol. 18, pp. 345202, 2007.
- [17] B. Ph and J. P. Borel, "Size effect on melting temperature of gold particles", *Phys. Rev.A*, vol. 13, pp. 2287–98, 1976.
- [18] W. M. Cranton, E. A. Mastio, C. B. Thomas, C. Tsakonas and R. Stevens. "Laser processing for enhanced performance thin film electroluminescent devices". *Electron. Lett.* 36, pp. 754. 2000.
- [19] J. F. Wager, D. A. Keszler and R. E. Presley, *Transparent Electronics*. Springer Publishing Company, Incorporated, 2007.
- [20] R. G. Gordon, "Criteria for choosing transparent conductors," *MRS Bull*, vol. 25, pp. 52-57, 2000.
- [21] G. Guzman, B. Dahmani, J. Puetz and M. A. Aegerter, "Transparent conducting sol–gel ATO coatings for display applications by an improved dip coating technique," *Thin Solid Films*, vol. 502, pp. 281-285, 2006.
- [22] P. D. Rack and P. H. Holloway, "The structure, device physics, and material properties of thin film electroluminescent displays," *Materials Science and Engineering: R: Reports*, vol. 21, pp. 171-219, 1998.
- [23] G. Gasparro, J. Pütz, D. Ganz and M. A. Aegerter, "Parameters affecting the electrical conductivity of SnO<sub>2</sub>: Sb sol–gel coatings," *Solar Energy Mater. Solar Cells*, vol. 54, pp. 287-296, 1998.

- [24] J. Spannhake, A. Helwig, G. Müller, G. Faglia, G. Sberveglieri, T. Doll, T. Wassner and M. Eickhoff, "SnO<sub>2</sub>: Sb-A new material for high-temperature MEMS heater applications: Performance and limitations," *Sensors Actuators B: Chem.*, vol. 124, pp. 421-428, 2007.
- [25] A. Pique and D. B. Chrisey, *Direct-Write Technologies for Rapid Prototyping Applications: Sensors, Electronics, and Integrated Power Sources*. Academic Press, 2002.
- [26] T. Giraldi, M. Escote, A. Maciel, E. Longo, E. Leite and J. Varela, "Transport and sensors properties of nanostructured antimony-doped tin oxide films," *Thin Solid Films*, vol. 515, pp. 2678-2685, 2006.
- [27] P. Edwards, A. Porch, M. Jones, D. Morgan and R. Perks, "Basic materials physics of transparent conducting oxides," *Dalton Transactions*, vol. 2004, pp. 2995-3002, 2004.
- [28] H. L. Hartnagel, A. L. Dawar, A. K. Jain, C. Jagadish and A. K. Jain, *Semiconducting Transparent Thin Films*. Taylor & Francis, Inc., 1995.
- [29] E. F. Schubert, *Doping in III-V semiconductors*, Cambridge University Press, vol. 1, 1993.
- [30] H. S. Nalwa, *Handbook of Thin Film Materials: Deposition and Processing of Thin Films*. Academic Pr, 2002.
- [31] H. Kawazoe, H. Yanagi, K. Ueda and H. Hosono, "Transparent p-type conducting oxides: design and fabrication of pn heterojunctions," *MRS Bull.*, vol. 25, pp. 28-36, 2000.
- [32] A. Facchetti and T. J. Marks, *Transparent Electronics*. Wiley Online Library, 2010.
- [33] O. Lupan, T. Pauporté, L. Chow, B. Viana, F. Pellé, L. Ono, B. Roldan Cuenya and H. Heinrich, "Effects of annealing on properties of ZnO thin films prepared by electrochemical deposition in chloride medium," *Appl. Surf. Sci.*, vol. 256, pp. 1895-1907, 2010.
- [34] S. J. Ikhmayies and R. N. Ahmad-Bitar, "An investigation of the bandgap and Urbach tail of vacuum-evaporated SnO<sub>2</sub> thin films," *Renewable Energy*, vol 49, pp 143-149, 2012.
- [35] J. Lin, Y. Zhang, Z. Ye, X. Gu, X. Pan, Y. Yang, J. Lu, H. He and B. Zhao, "Nb-doped ZnO transparent conducting films fabricated by pulsed laser deposition," *Appl. Surf. Sci.*, vol. 255, pp. 6460-6463, 2009.

- [36] H. Hartnagel, A. Dawar, A. Jain and C. Jagadish, *Semiconducting Transparent Thin Films*. Institute of Physics Pub., 1995.
- [37] T. Giraldi, M. Escote, M. Bernardi, V. Bouquet, E. Leite, E. Longo and J. Varela, "Effect of Thickness on the Electrical and Optical Properties of Sb Doped SnO<sub>2</sub> (ATO) Thin Films," *Journal of Electroceramics*, vol. 13, pp. 159-165, 2004.
- [38] H. Liu, V. Avrutin, N. Izyumskaya, Ü. Özgür and H. Morkoç, "Transparent conducting oxides for electrode applications in light emitting and absorbing devices," *Superlattices and Microstructures*, vol. 48, pp. 458-484, 2010.
- [39] H. Lee and O. Ok Park, "Electron scattering mechanisms in indium-tin-oxide thin films: grain boundary and ionized impurity scattering," *Vacuum*, vol. 75, pp. 275-282, 2004.
- [40] R. L. Petritz, "Theory of photoconductivity in semiconductor films," *Physical Review*, vol. 104, pp. 1508, 1956.
- [41] V. Geraldo, L. V. A. Scalvi, E. A. Morais, C. V. Santilli and S. H. Pulcinelli, "Sb doping effects and oxygen adsorption in SnO<sub>2</sub> thin films deposited via sol-gel," *Materials Research*, vol. 6, pp. 451-456, 2003.
- [42] L. Peng-Fei, S. Yue, Y. Zhong-Yuan, Z. Long, L. Qiong-Yao, M. Shi-Jia, H. Li-Hong and L. Yu-Min, "Electronic Structure and Optical Properties of Antimony-Doped SnO<sub>2</sub> from First-Principle Study," *Communications in Theoretical Physics*, vol. 57, pp. 145, 2012.
- [43] H. Hosono, D. C. Paine and D. S. Ginley, *Handbook of Transparent Conductors*. Springer, 2010.
- [44] T. M. Hammad and N. K. Hejazy, "Structural, electrical, and optical properties of ATO thin films fabricated by dip coating method," *International Nano Letters*, vol. 2, pp. 7, 2012.
- [45] C. Wang, C. Huang, J. Kuo and J. Huang, "Investigation of pulsed ultraviolet laser annealing of Sb/SnO<sub>2</sub> thin films on the structural, optical and electrical properties," *Surf. Coat. Technol.*, .
- [46] T. Tsuchiya, F. Kato, T. Nakajima, K. Igarashi and T. Kumagai, "Direct conversion of a metal organic compound to epitaxial Sb-doped SnO<sub>2</sub> film on a (001) TiO<sub>2</sub> substrate using a KrF laser, and its resulting electrical properties," *Appl. Surf. Sci.*, vol. 255, pp. 9808-9812, 2009 .
- [47] A. Babar, S. Shinde, A. Moholkar, C. Bhosale, J. Kim and K. Rajpure, "Structural and optoelectronic properties of antimony incorporated tin oxide thin films," *J. Alloys Compounds*, vol. 505, pp. 416-422, 2010.
-

- [48] A. De and S. Ray, "A study of the structural and electronic properties of magnetron sputtered tin oxide films," *J. Phys. D*, vol. 24, pp. 719, 2000.
- [49] W. M. Cranton, "Excimer laser processing of inkjet-printed and sputter-deposited transparent conducting SnO<sub>2</sub>:Sb for flexible electronics," *Thin Solid Films*, vol. 515, pp. 8534-8538, 2007.
- [50] C. Sandu S., V. Teodorescu S., C. Ghica, P. Hoffmann, T. Bret, A. Brioude, M. Blanchin G, J. Roger A, B. Canut and M. Croitoru, "Excimer Laser Crystallization of SnO<sub>2</sub>: Sb Sol-Gel Films," *J. Sol Gel Sci. Technol.*, vol. 28, pp. 227-234, 2003.
- [51] J. Lim, B. Y. Jeong, H. G. Yoon, S. N. Lee and J. Kim, "Inkjet-Printing of Antimony-Doped Tin Oxide (ATO) Films for Transparent Conducting Electrodes," *Journal of Nanoscience and Nanotechnology*, vol. 12, pp. 1675-1678, 2012.
- [52] N. León-Brito, A. Melendez, I. Ramos, N. J. Pinto and J. J. Santiago-Aviles, "Electrical properties of electrospun sb-doped tin oxide nanofibers," in *Journal of Physics: Conference Series*, pp. 683, 2007.
- [53] Nano materials in printed electronics, [www.plusplastic electronics.com](http://www.plusplasticelectronics.com), vol. 3, pp. 14-15, 2011.
- [54] X. Feng, J. Ma, F. Yang, F. Ji, F. Zong, C. Luan and H. Ma, "Highly thermal stable transparent conducting SnO<sub>2</sub>: Sb epitaxial films prepared on  $\alpha$ -Al<sub>2</sub>O<sub>3</sub>(0001) by MOCVD," *Appl. Surf. Sci.*, vol. 254, pp. 6601-6604, 2008.
- [55] K. Wasa, M. Kitabatake and H. Adachi, *Thin Film Materials Technology: Sputtering of Compound Materials*. Springer, 2004.
- [56] R. F. Bunshah, *Handbook of Deposition Technologies for Films and Coatings: Science, Technology, and Applications*. William Andrew Publishing, 1994.
- [57] J. L. Huang, Y. Pan, J. Y. Chang and B. S. Yau, "Annealing effects on properties of antimony tin oxide thin films deposited by RF reactive magnetron sputtering," *Surface and Coatings Technology*, vol. 184, pp. 188-193, 2004.
- [58] J. Montero, C. Guillén and J. Herrero, "Discharge power dependence of structural, optical and electrical properties of DC sputtered antimony doped tin oxide (ATO) films," *Solar Energy Mater. Solar Cells*, vol. 95, pp. 2113-2119, 2011.
- [59] S. Wakeham, M. Thwaites, B. Holton, C. Tsakonas, W. Cranton, D. Koutsogeorgis and R. Ranson, "Low temperature remote plasma sputtering of indium tin oxide for flexible display applications," *Thin Solid Films*, vol. 518, pp. 1355-1358, 2009.

- [60] M. Hwang, B. Jeong, J. Moon, S. K. Chun and J. Kim, "Inkjet-printing of indium tin oxide (ITO) films for transparent conducting electrodes," *Materials Science and Engineering: B*, vol. 176, pp. 1128-1131, 2011.
- [61] C. Brinker, A. Hurd, P. Schunk, G. Frye and C. Ashley, "Review of sol-gel thin film formation," *J. Non Cryst. Solids*, vol. 147, pp. 424-436, 1992.
- [62] J. Pütz, D. Ganz, G. Gasparro and M. Aegerter A, "Influence of the Heating Rate on the Microstructure and on Macroscopic Properties of Sol-Gel SnO<sub>2</sub>: Sb Coatings," *J. Sol Gel Sci. Technol.*, vol. 13, pp. 1005-1010, 1998.
- [63] D. Zhang, L. Tao, Z. Deng, J. Zhang and L. Chen, "Surface morphologies and properties of pure and antimony-doped tin oxide films derived by sol-gel dip-coating processing," *Mater. Chem. Phys.*, vol. 100, pp. 275-280, 2006.
- [64] D. B. Mitzi, *Solution Processing of Inorganic Materials*. Wiley Online Library, 2009.
- [65] R. R. Tummala, *Fundamentals of Microsystems Packaging*. McGraw-Hill New York:, 2001.
- [66] L. Dua, A. De, S. Chakraborty and P. Biswas, "Study of spin coated high antimony content Sn-Sb oxide films on silica glass," *Mater Charact*, vol. 59, pp. 578-586, 2008.
- [67] C. Goebbert, R. Nonninger, M. A. Aegerter and H. Schmidt, "Wet chemical deposition of ATO and ITO coatings using crystalline nanoparticles redispersable in solutions," *Thin Solid Films*, vol. 351, pp. 79-84, 1999.
- [68] G. Cao, *Nanostructures & Nanomaterials: Synthesis, Properties & Applications*. World Scientific Publishing Company, 2004.
- [69] B. Zhang, Y. Tian, J. Zhang and W. Cai, "The FTIR studies of SnO<sub>2</sub>: Sb (ATO) films deposited by spray pyrolysis," *Mater Lett*, vol 65, pp 1204-1206, 2011.
- [70] K. Rajpure, M. Kusumade, M. N. Neumann-Spallart and C. Bhosale, "Effect of Sb doping on properties of conductive spray deposited SnO<sub>2</sub> thin films," *Mater. Chem. Phys.*, vol. 64, pp. 184-188, 2000.
- [71] R. Elmqvist, "Measuring instrument of the recording type", *US Pattern-US2566443 A*, 1951.
- [72] H. P. Le, "Progress and trends in ink-jet printing technology," *The Journal of Imaging Science and Technology*, vol. 42, pp. 49-62, 1998.
-

- [73] R. McMahon, M. Smith, K. Seffen, M. Voelskow, W. Anwand and W. Skorupa, "Flash-lamp annealing of semiconductor materials—Applications and process models," *Vacuum*, vol. 81, pp. 1301-1305, 2007.
- [74] J. Leem and J. Yu, "Physical properties of electrically conductive Sb-doped SnO<sub>2</sub> transparent electrodes by thermal annealing dependent structural changes for photovoltaic applications," *Materials Science and Engineering: B*, vol. 176, pp. 1207-1212, 2011.
- [75] J. Jeng, "The influence of annealing atmosphere on the material properties of sol-gel derived SnO<sub>2</sub>: Sb films before and after annealing," *Appl. Surf. Sci.*, vol. 258, pp 5981-5986, 2012.
- [76] S. S. Park, H. Zheng and J. Mackenzie, "Sol-gel derived antimony-doped tin oxide coatings on ceramic cloths," *Mater Lett*, vol. 22, pp. 175-180, 1995.
- [77] F. Gao, K. Yu, R. Mendelsberg, A. Anders and W. Walukiewicz, "Preparation of high transmittance ZnO: Al film by pulsed filtered cathodic arc technology and rapid thermal annealing," *Appl. Surf. Sci.*, vol. 257, pp. 7019-7022, 2011.
- [78] H. Wang, M. Xu, J. Xu, M. Ren and L. Yang, "Low temperature synthesis of sol-gel derived Al-doped ZnO thin films with rapid thermal annealing process," *J. Mater. Sci. : Mater. Electron.*, vol. 21, pp. 589-594, 2010.
- [79] C. Jin, I. You and H. Kim, "Effect of rapid thermal annealing on the properties of spin-coated InZnSnO films," *Current Applied Physics*, .
- [80] S. Song, T. Yang, J. Liu, Y. Xin, Y. Li and S. Han, "Rapid thermal annealing of ITO films," *Appl. Surf. Sci.*, vol. 257, pp. 7061-7064, 2011.
- [81] T. Boudiar, C. Sandu, B. Canut, M. Blanchin, V. Teodorescu and J. Roger, "Interest of Rapid Thermal Annealing (RTA) for the Elaboration of SnO<sub>2</sub>: Sb Transparent Conducting Oxide by the Sol-Gel Technique," *J. Sol Gel Sci. Technol.*, vol. 26, pp. 1067-1070, 2003.
- [82] W. Skorupa, W. Anwand, M. Posselt, S. Prucnal, L. Rebohle, M. Voelskow, S. Zhou, R. A. McMahon, M. Smith, T. Gebel, W. Hentsch, R. Fendler, T. Luthge, A. Satta, T. M. Borseth, A. Y. Kuznetsov and B. G. Svensson, "Millisecond processing beyond chip technology: From electronics to photonics," in *Advanced Thermal Processing of Semiconductors, 2007. RTP 2007. 15th International Conference on*, 2007, pp. 41-49.
- [83] M. A. Aegerter, A. Reich, D. Ganz, G. Gasparro, J. Pütz and T. Krajewski, "Comparative study of SnO<sub>2</sub>: Sb transparent conducting films produced by various coating and heat treatment techniques," *J. Non Cryst. Solids*, vol. 218, pp. 123-128, 1997.

- [84] C. S. Sandu, "Densification and crystallization of SnO<sub>2</sub>:Sb sol-gel films using excimer laser annealing," *Appl. Surf. Sci.*, vol. s 208-209, pp. 382-387, 2003.
- [85] J. A. Jeong, J. Lee, H. Kim, H. K. Kim and S. I. Na, "Ink-jet printed transparent electrode using nano-size indium tin oxide particles for organic photovoltaics," *Solar Energy Mater. Solar Cells*, vol. 94, pp. 1840-1844, 2010.
- [86] C. G. Granqvist, "Transparent conductors as solar energy materials: a panoramic review," *Solar Energy Mater. Solar Cells*, vol. 91, pp. 1529-1598, 2007.
- [87] G. Khrypunov, A. Romeo, F. Kurdesau, D. Bätzner, H. Zogg and A. Tiwari, "Recent developments in evaporated CdTe solar cells," *Solar Energy Mater. Solar Cells*, vol. 90, pp. 664-677, 2006.
- [88] A. Morales-Acevedo, "Thin film CdS/CdTe solar cells: Research perspectives," *Solar Energy*, vol. 80, pp. 675-681, 2006.
- [89] C. M. Lampert, "Heat mirror coatings for energy conserving windows," *Solar Energy Materials*, vol. 6, pp. 1-41, 1981.
- [90] A. Khan, N. Rasmussen, V. Marinov and O. F. Swenson, "Laser sintering of direct write silver nano-ink conductors for microelectronic applications," in *Proceedings of SPIE*, 2008, pp. 687910.
- [91] D. Ganz, A. Reich and M. A. Aegerter, "Laser firing of transparent conducting SnO<sub>2</sub> sol-gel coatings," *J. Non Cryst. Solids*, vol. 218, pp. 242-246, 1997.
- [92] W. Runyan R. and T. Shaffner J., *Semiconductor Measurements and Instrumentation*. McGraw-Hill Professional, 1998.
- [93] K. H. Park, "Cross-sectional TEM specimen preparation of semiconductor devices by focused ion beam etching," in *Materials Research Society Symposium Proceedings, MRS, Pittsburgh*, 1990, pp. 271-280.
- [94] S. Newcomb, "Modern approaches to the preparation of TEM samples," *Electron Microscopy and Analysis 2003*, pp. 357-362, 2004.
- [95] S. Geng, S. Zhang and H. Onishi, "XPS Applications in Thin Films Research," *Mater. Technol.*, vol. 17, pp. 234, 2002.
- [96] A. J. Hartmann and R. N. Lamb, "X-ray photoemission spectroscopy of thin films," *Current Opinion in Solid State and Materials Science*, vol. 2, pp. 511-516, 1997.
- [97] J. C. Vickerman and I. S. Gilmore, *Surface Analysis: The Principal Techniques*. Wiley Online Library, 2009.
-

- [98] L. van der PAUYV, "A method of measuring specific resistivity and Hall effect of discs of arbitrary shape," *Philips Res.Rep*, Vol. 13, 1958.
- [99] E. H. Hall, "On a new action of the magnet on electric currents," *American Journal of Mathematics*, vol. 2, pp. 287-292, 1879.
- [100] C. Brinker, G. Frye, A. Hurd and C. Ashley, "Fundamentals of sol-gel dip coating," *Thin Solid Films*, vol. 201, pp. 97-108, 1991.
- [101] S. L. Wilson, "*Laser processing of Inkjet printed and RF magnetron sputtered SnO<sub>2</sub>:Sb*," PhD thesis, Nottingham Trent University, 2008.
- [102] A. P. Sommer and N. Rozlosnik, "Formation of crystalline ring patterns on extremely hydrophobic supersmooth substrates: Extension of ring formation paradigms," *Crystal Growth & Design*, vol. 5, pp. 551-557, 2005.
- [103] D. Soltman and V. Subramanian, "Inkjet-printed line morphologies and temperature control of the coffee ring effect," *Langmuir*, vol. 24, pp. 2224-2231, 2008.
- [104] R. D. Deegan, O. Bakajin, T. F. Dupont, G. Huber, S. R. Nagel and T. A. Witten, "Capillary flow as the cause of ring stains from dried liquid drops," *Nature*, vol. 389, pp. 827-828, 1997.
- [105] R. D. Deegan, O. Bakajin, T. F. Dupont, G. Huber, S. R. Nagel and T. A. Witten, "Contact line deposits in an evaporating drop," *Physical Review E*, vol. 62, pp. 756-765, 2000.
- [106] J. Perelaer, P. J. Smith, C. E. Hendriks, A. M. J. van den Berg and U. S. Schubert, "The preferential deposition of silica micro-particles at the boundary of inkjet printed droplets," *Soft Matter*, vol. 4, pp. 1072-1078, 2008.
- [107] K. Morii and T. Shimoda, "Film Formation by Inkjet-Behavior of Inkjet Droplets," *Journal-surface science of Japan*, vol. 24, pp. 90-97, 2003.
- [108] T. Shimoda, K. Morii, S. Seki and H. Kiguchi, "Inkjet printing of light-emitting polymer displays," *MRS Bulletin- materials research society*, vol. 28, pp. 821-828, 2003.
- [109] H. Dong, W. W. Carr and J. F. Morris, "An experimental study of drop-on-demand drop formation," *Phys. Fluids*, vol. 18, pp. 072102, 2006.
- [110] T. R. Giraldi, A. J. C. Lanfredi, E. R. Leite, M. T. Escote, E. Longo, J. A. Varela, C. Ribeiro and A. J. Chiquito, "Electrical characterization of SnO:Sb ultrathin films obtained by controlled thickness deposition," *J. Appl. Phys.*, vol. 102, pp. 034312, 2007.

- [111] I. Song, D. Ma, S. Heo and D. Moon, "P-57: Study on the wet processable antimony tin oxide (transparent conducting oxide, TCO) using anode for PLED device instead of ITO," *SID Symposium Digest of Technical Papers*, vol 40, pp 1306-1308, 2009, .
- [112] C. Terrier, J. Chatelon and J. Roger, "Electrical and optical properties of Sb: SnO<sub>2</sub> thin films obtained by the sol-gel method," *Thin Solid Films*, vol. 295, pp. 95-100, 1997.
- [113] J. Ni, X. Zhao, X. Zheng, J. Zhao and B. Liu, "Electrical, structural, photoluminescence and optical properties of p-type conducting, antimony-doped SnO<sub>2</sub> thin films," *Acta Materialia*, vol. 57, pp. 278-285, 2009.
- [114] F. Yang, X. J. Zhang, X. Wu, F. Tian and F. Gan, "Preparation of highly dispersed antimony-doped tin oxide nanopowders by azeotropic drying with isoamyl acetate," *Transactions of Nonferrous Metals Society of China*, vol. 17, pp. 626-632, 2007.
- [115] B. Zhanman, "Conduction Mechanism of Sb<sub>2</sub>O<sub>3</sub> Doped SnO<sub>2</sub> Semiconductor [J]," *Journal of Inorganic Materials*, vol. 4, 1990.
- [116] B. Thangaraju, "Structural and electrical studies on highly conducting spray deposited fluorine and antimony doped SnO<sub>2</sub> thin films from SnCl<sub>2</sub> precursor," *Thin Solid Films*, vol. 402, pp. 71-78, 2002.
- [117] U. Zum Felde, M. Haase and H. Weller, "Electrochromism of highly doped nanocrystalline SnO<sub>2</sub>: Sb," *The Journal of Physical Chemistry B*, vol. 104, pp. 9388-9395, 2000.
- [118] Q. Wan, E. N. Dattoli and W. Lu, "Transparent metallic Sb-doped SnO<sub>2</sub> nanowires," *Appl. Phys. Lett.*, vol. 90, pp. 222107-222107-3, 2007.
- [119] B. Stjerna, E. Olsson and C. Granqvist, "Optical and electrical properties of radio frequency sputtered tin oxide films doped with oxygen vacancies, F, Sb, or Mo," *J. Appl. Phys.*, vol. 76, pp. 3797-3817, 1994.
- [120] E. Shanthi, V. Dutta, A. Banerjee and K. Chopra, "Electrical and optical properties of undoped and antimony-doped tin oxide films," *J. Appl. Phys.*, vol. 51, pp. 6243-6251, 1980.
- [121] L. Lili, M. Liming and D. Xuechen, "Solvothermal synthesis and characterization of Sb-doped SnO<sub>2</sub> nanoparticles used as transparent conductive films," *Mater. Res. Bull.*, vol. 41, pp. 541-546, 2006.
- [122] R. Withnall, J. Silver, P. G. Harris, T. G. Ireland and P. J. Marsh, "AC powder electroluminescent displays," *Journal of the Society for Information Display*, vol. 19, pp. 798-810, 2012.

- [123] Y. A. Ono, *Electroluminescent Displays*. World Scientific Publishing Company Incorporated, 1995.
- [124] Elumin8, " www.elumin8.com/technologies.html," vol. 2013, .
- [125] LuminousMedia, " www.eluminousmedia.com/," vol. 2013, .
- [126] W. M. Yen and H. Yamamoto, *Phosphor Handbook*. CRC, 2006.
- [127] A. Lakshmanan, *Luminescence and Display Phosphors: Phenomena and Applications*. Nova Science Pub Incorporated, 2008.
- [128] S. Azoubel, S. Shemesh and S. Magdassi, "Flexible electroluminescent device with inkjet-printed carbon nanotube electrodes," *Nanotechnology*, vol. 23, pp. 344003, 2012.
- [129] H. E. Yin, C. H. Wu, K. S. Kuo, W. Y. Chiu, C. F. Lee, N. Li and P. J. Chen, "Synthesis and optoelectronic properties of high transparent polymer based anode materials with good wetting abilities and their application in electroluminescent devices," *Synth. Met.*, vol. 161, pp. 1878-1885, 2011.
- [130] H. Kim, J. Horwitz, W. Kim, S. Qadri and Z. Kafafi, "Anode material based on Zr-doped ZnO thin films for organic light-emitting diodes," *Appl. Phys. Lett.*, vol. 83, pp. 3809-3811, 2003.
- [131] M. J. Kim, D. W. Shin, J. Y. Kim, S. H. Park and J. B. Yoo, "The production of a flexible electroluminescent device on polyethylene terephthalate films using transparent conducting carbon nanotube electrode," *Carbon*, vol. 47, pp. 3461-3465, 2009.
- [132] E. A. Mastio, M. R. Craven, W. M. Cranton, C. B. Thomas, M. Robino and E. Fogarassy, "The effects of KrF pulsed laser and thermal annealing on the crystallinity and surface morphology of radiofrequency magnetron sputtered ZnS: Mn thin films deposited on Si," *J. Appl. Phys.*, vol. 86, pp. 2562, 1999.
- [133] D. C. Koutsogeorgis, "*Investigation of laser annealing of thin film phosphors for potential luminescent devices*," PhD. Thesis, Nottingham Trent University, July 2003.
- [134] J. McKittrick, G. Hirata, C. Bacalski, R. Sze, J. Mourant, K. Hubbard, S. Pattilo, K. Salazar, M. Trkula and T. Gosnellb, "Enhanced photoluminescent emission of thin phosphor films via pulsed excimer laser melting," *J. Mater. Res.*, vol. 13, pp 3019-3021, 1998.
- [135] G. Hirata A., J. McKittrick, M. Trkula, J. Mourant and R. Sze, "Laser melting of photoluminescent (Y 0.92Eu 0.08)<sub>2</sub>O<sub>3</sub> films," *J. Appl. Phys.*, vol. 90, pp. 3919-3924, 2001.
-

- [136] B. K. Gupta, D. Haranath, S. Saini, V. N. Singh and V. Shanker, "Synthesis and characterization of ultra-fine  $Y_2O_3:Eu_3$  nanophosphors for luminescent security ink applications," *Nanotechnology*, vol. 21, pp. 055607, 2010.
- [137] R. M. Ranson, "*Investigation into thermographic phosphors*," PhD Thesis , Nottingham trent University, 1999.

## **APPENDIX A. List of Presentations**

### *Oral presentations*

6<sup>th</sup> December 2012: Institute of Physics (IOP) Printing and Graphic science group annual student conference, Institute of Physics, London, UK

### *Poster presentations*

5<sup>th</sup> - 6<sup>th</sup> September 2011; Society for Information Display Organic Electronics UK 2011, Imperial College, UK

2<sup>nd</sup> - 3<sup>rd</sup> March 2011: Electronic Displays 2011, Nuremberg, Germany

11<sup>th</sup> – 18<sup>th</sup> July 2010; 2<sup>nd</sup> International School on Laser- surface interactions for new materials production: Tailoring structure and properties, Venice, Italy.

## APPENDIX B. Excimer Laser processing of $Y_2O_3:Eu$

### *B.1 Introduction*

Prior work in the literature regarding successful laser annealing of phosphor thin films of single layer and multilayer ZnS:Mn and SrS:CuAg has been published by the NTU displays group [132,133]. In terms of laser irradiation of  $Y_2O_3:Eu$  the available literature is more limited.

McKittrick et al [134,135] have reported the use of KrF laser to melt  $Y_2O_3:Eu$  thin films. These thin films were deposited by the chemical vapour deposition technique and during deposition the sapphire substrate was held at a fixed temperature between 400°C and 700°C. A single pulse of KrF laser at a fluence of  $1.02 \text{ J.cm}^{-2}$  caused melting which smoothed and densified the film. They also reported that following laser processing, the PL intensity was increased by 122% over that of the as-deposited film. Still there are some disadvantages with this technique, since flexible substrates are not suitable for depositions requiring these high temperatures. Therefore via collaboration, the FAB 3D research work investigated the feasibility of functionalising solution processed  $Y_2O_3:Eu$  thin films by Excimer laser processing.

Rare-earth-activated oxide phosphors are essential materials in display applications. Among these oxide-based phosphors,  $Y_2O_3:Eu$  phosphors are one of the most promising oxide-based red phosphors systems due to its excellent luminescence efficiency, colour purity, and stability. It is particularly useful for photoluminescent applications – and also can exhibit electroluminescent properties.

$Y_2O_3$  has a rare-earth sesquioxide c-type structure with each  $Y^{3+}$  ion being surrounded by six oxygen atoms sited at six corners of the cube. A  $Eu^{3+}$  ion in a  $Y_2O_3$  crystal can occupy two types of symmetric sites as;

- A low symmetric site of  $C_2$  and
- A high symmetric site of  $C_{3i}$  as shown in figure B.1

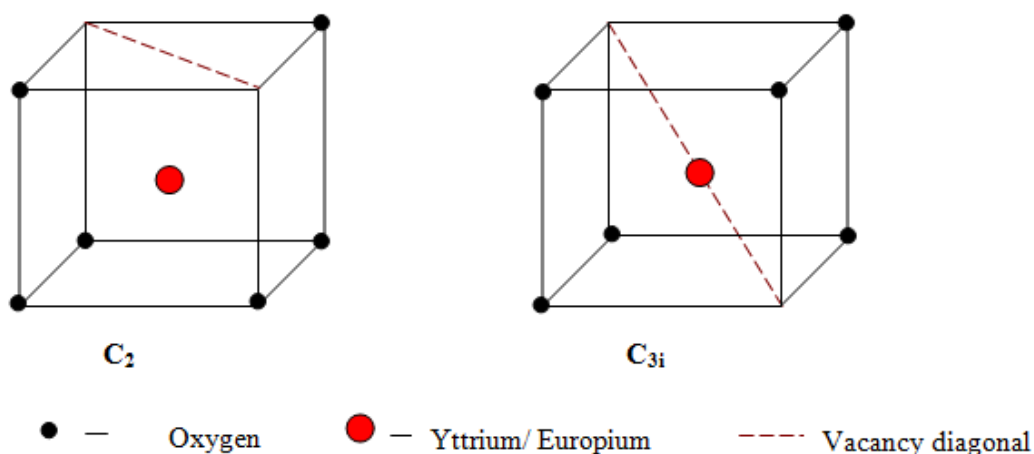


Figure B.1: Probable positions of Y/E ions in the cubic crystal structure of  $Y_2O_3$  at  $C_2$  and  $C_{3i}$  symmetry sites.

Due to the shielding effect of 4f electrons by 5s and 5p electron shell's of the  $Eu^{3+}$  ions, the vacancy diagonal of the  $C_2$  and  $C_{3i}$  has two different positions [136]. The energy level diagram of  $Eu^{3+}$  ions in the  $Y_2O_3$  lattice with all probable electric dipole transitions is shown in figure B.2 [137]. The 611 nm peak corresponds to the transition from  ${}^5D_0-{}^7F_2$ . If  $Eu^{3+}$  ion occupies the  $C_{3i}$  site, the emission of  ${}^5F_0-{}^7D_0$  transition is forbidden. On the other hand, if the  $Eu^{3+}$  ions occupies the  $C_2$  site, the emission of  ${}^5D_0-{}^7F_j$  ( $j = 1-4$ ), transitions is allowed.

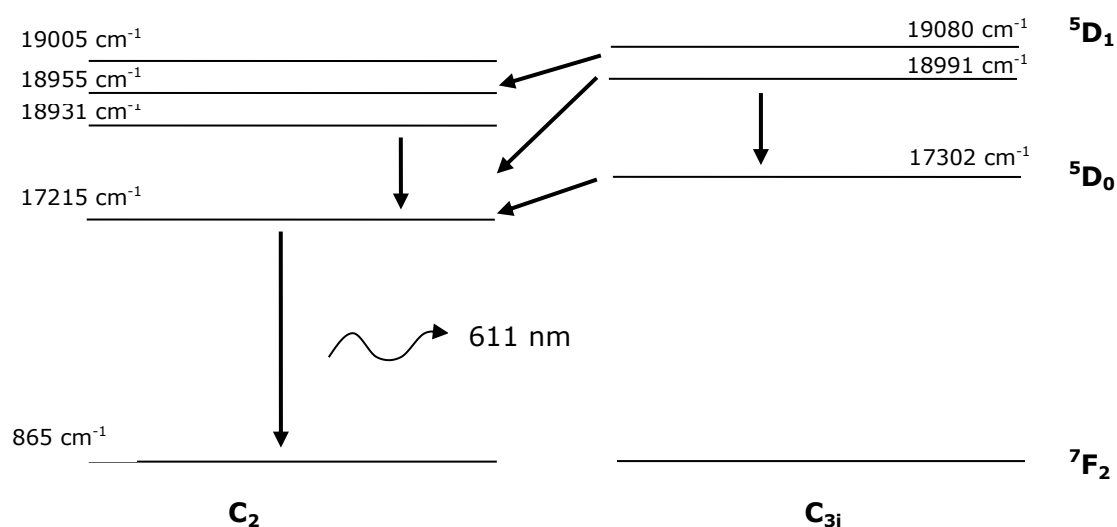


Figure B.2: Energy level diagram with possible transitions of  $Eu^{3+}$  ions.

## B.2 Photoluminescence (PL)

Photoluminescence of  $\text{Y}_2\text{O}_3:\text{Eu}$  was measured in a dark room environment to reduce the ambient illumination. A Nd:YAG laser emitting at 266 nm and He:Cd laser emitting at 326 nm were used as the excitation sources. While using the 266 nm, a set of quartz plates and a variable aperture were used to reduce the beam size and laser energy. The PL set-up used for this work is shown in figure B.3.

The laser fluence used for this work is  $\sim 1.58$  mJ/pulse. The laser beam is reflected down to the sample using a mirror, and the quartz fibre is mounted at an angle to collect the light generated and guide to the Ocean optics S2000 Miniature Fibre Optic Spectrometer including ADC1000-USB A/D Converter

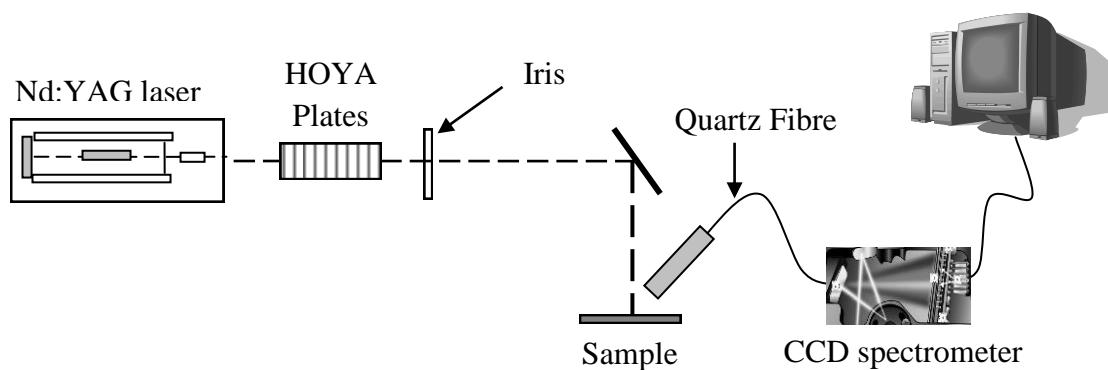


Figure B.3: schematic of photoluminescence measurement set up

Within the spectrometer, the light passes through the slit, and Filter, and then reflects off the Collimating Mirror onto the Grating. Then the gratings direct the diffracted light onto the focusing mirror which focuses first order spectra onto the CCD array and it converts the optical signal into a digital signal. The CCD array contains 2048 elements for the range of 330- 1010 nm.

### ***B.3 Thin film deposition of Y<sub>2</sub>O<sub>3</sub>:Eu***

The initial investigation was carried out using the Y<sub>2</sub>O<sub>3</sub>:Eu nanoparticulate ink based on fired Y<sub>2</sub>O<sub>3</sub>:Eu powder. The precise method of nanoparticulate ink formulation is proprietary of Brunel University and Sun Chemicals UK. The first batch of Y<sub>2</sub>O<sub>3</sub>:Eu ink has turned in a set jelly type structure and failed to inkjet print due to higher viscosity. Therefore samples were coated onto glass substrate using 12- micron k-bar. K-bar coating is a technique use to apply a layer of ink without set-up and cleaning time involved in printing. A steel bar is used to draw ink over a substrate at constant speed and pressure. The film thickness is controlled by the regular series of grooves made by winding steel wire over a steel rod.

#### ***B.3.1 k-bar coated Y<sub>2</sub>O<sub>3</sub>:Eu on glass***

Initially the laser processing of Y<sub>2</sub>O<sub>3</sub>:Eu work was carried out using K-Bar coated samples by Printed Electronics Ltd. The 12 μ k-bar was used to coat Y<sub>2</sub>O<sub>3</sub>:Eu ink onto Eagle 2000 glass substrate (5 x 5 cm<sup>2</sup>) and the first batch was made out of six samples.

The Lambda Physik LPX305i excimer laser emitting at 248 nm and 193 nm were used to laser process these samples. Firstly a sample (PEY2O3-3) was laser processed using KrF laser emitting at 248 nm. The raw laser beam was passed through a homogeniser to create 3x3 mm<sup>2</sup> uniform beam footprint at sample stage. The pressure cell with its quartz window was used to place the sample and to laser processed in a pressured environment of O<sub>2</sub>, at 140 PSI. A small reflected beam from the incident beam was measured with an energy monitor and has been calibrated so that the sample energy at the pressure cell, can be determined. (The calibration chart is shown in figure B.4).

By varying the laser fluence from 0.27 – 1.25 J.cm<sup>-2</sup> and the number of pulses up to five pulses, 25 areas were laser processed.

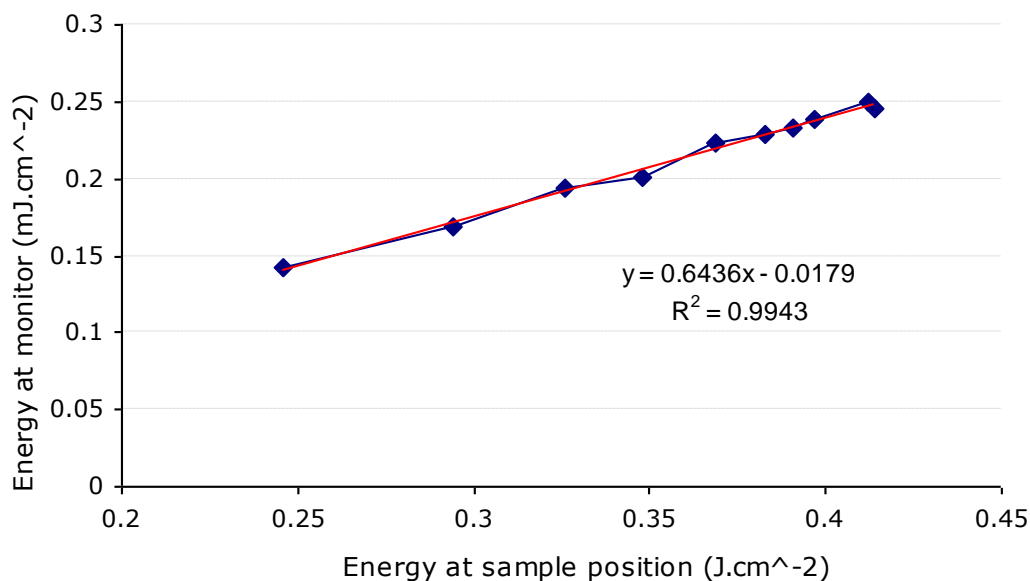


Figure B.4 : Calibration chart for the laser fluence at sample surface- 248 nm laser.

### B.3.1.1 Photoluminescence (PL)

The PL spectra of the laser processed samples were measured at room temperature using an ocean optics S2000 Miniature Fibre Optic Spectrometer including ADC1000-USB A/D Converter in the wavelength range from 330- 1000 nm. The PL was measured with two excitation wavelengths; 266 nm and 325 nm.

Figure B.5 (a) and (b) shows the PL spectra of the laser processed  $Y_2O_3:Eu$  at 325 nm and 266 nm excitation. The main emission peak was obtained at 616 nm. In both cases with 248 nm KrF laser processing, the  $Y_2O_3:Eu$  films deposited on glass show little or no enhancement to their PL intensity. This may be due to the fact that the phosphor thin films are optically transparent to the KrF laser irradiation or compared to the glass fluorescence peak that appeared in the PL spectra, the variation of the phosphor energy transition peak is difficult to detect.

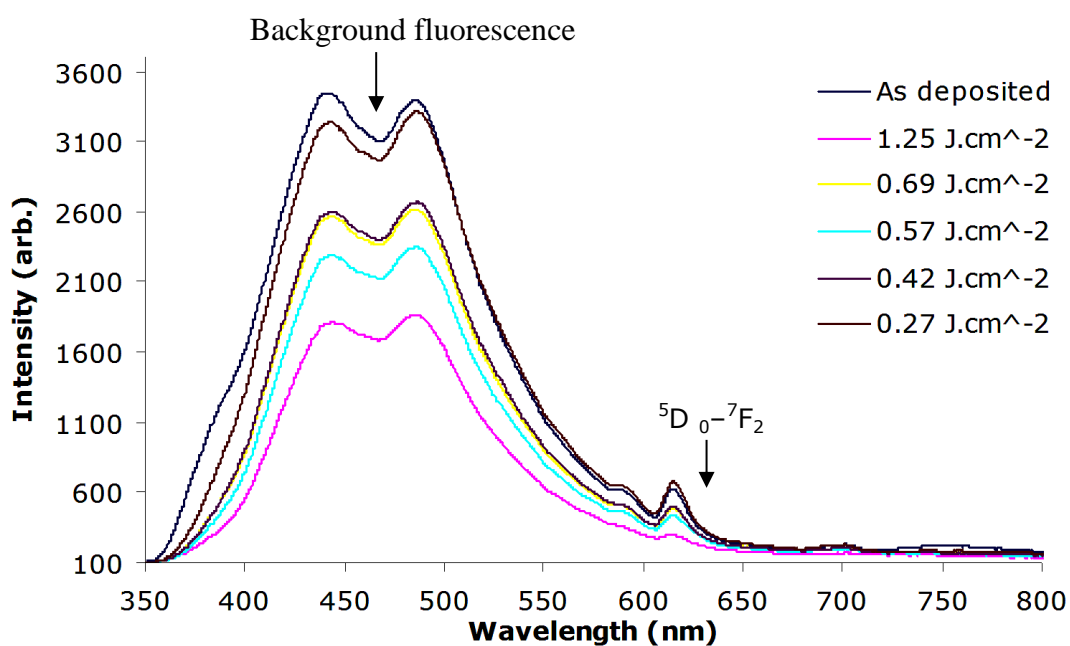


Figure B.5(a): PL emission from  $\text{Y}_2\text{O}_3:\text{Eu}$  thin film on glass substrate laser processed (at 248 nm) with 5 irradiation pulses in an  $\text{O}_2$  over pressure of 140 PSI; excitation at 325 nm.

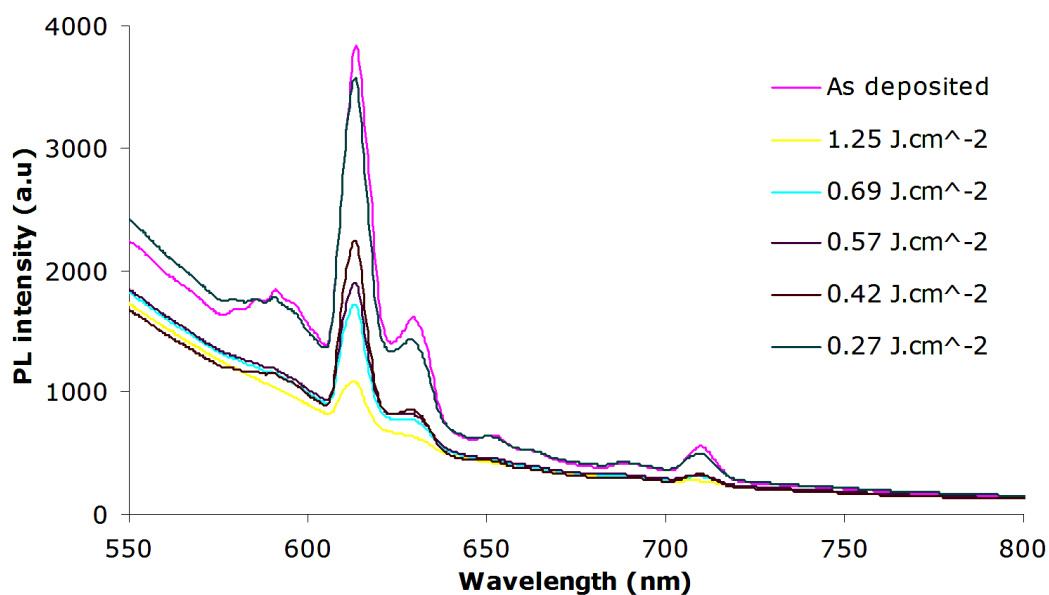


Figure B.5 (b): PL emission from  $\text{Y}_2\text{O}_3:\text{Eu}$  thin film on glass substrate laser processed (at 248 nm) with 5 irradiation pulses in an  $\text{O}_2$  over pressure of 140 PSI; excitation at 266 nm.

### B.3.1.2 Surface roughness

The surface roughness of the as-deposited and laser processed k-bar coated  $Y_2O_3:Eu$  thin films were investigated using an Atomic Force Microscopy (AFM). Figure B.6 shows the surface morphology comparison, using AFM images of as-deposited and laser processed k-bar coated  $Y_2O_3:Eu$  thin films.

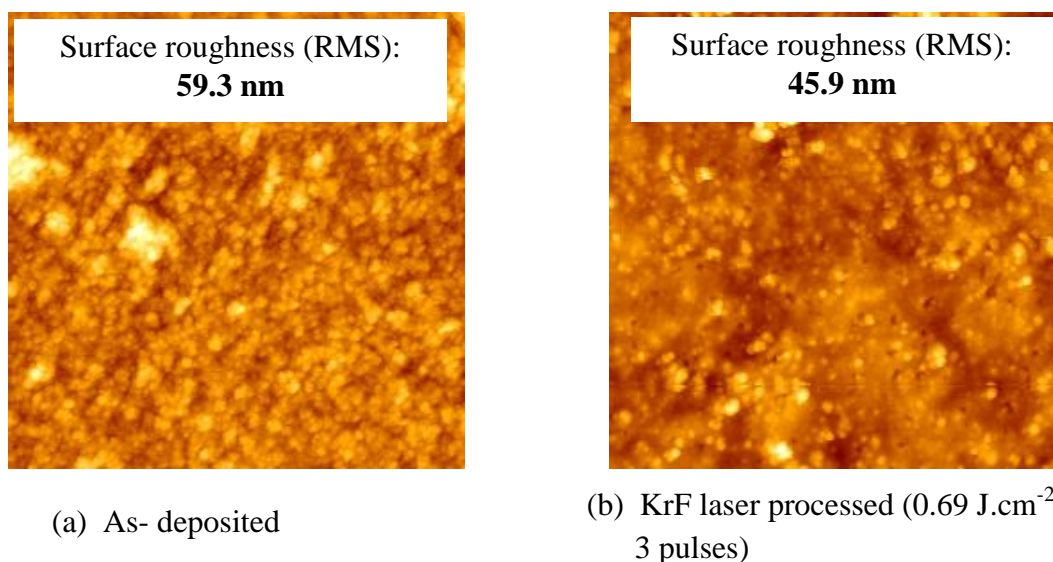


Figure B.6: AFM images of As-deposited and KrF laser processed ( $0.69 \text{ J.cm}^{-2}$ , 3 pulses) K-bar coated  $Y_2O_3:Eu$

The perspective surface representations of measured surface areas ( $10 \times 10 \mu\text{m}$ ) highlighted some surface texture variation between as-deposit and laser processed areas. Also considerable surface roughness variation was obtained when the sample was irradiated with KrF laser emitting at 248 nm at  $0.69 \text{ J.cm}^{-2}$ .

It has been demonstrated that for an efficient absorption of the laser irradiation in the  $Y_2O_3:Eu$  thin film, it is necessary to irradiate with photons of energy higher than the band gap. At lower photon energies these films are optically transparent [132]. As the KrF irradiation has lower photon energy ( $\sim 5.0 \text{ eV}$ ) than the band gap of the  $Y_2O_3$  ( $\sim 6.2 \text{ eV}$ ), the gas of the Excimer laser was changed to ArF (emitting at 193 nm,  $\sim 6.42 \text{ eV}$ ) and laser processing was undertaken on another k-bar coated  $Y_2O_3:Eu$  sample (PEY2O3-5). For this experiment the sample was thermal annealed at  $400^\circ\text{C}$  for  $\sim 1\text{hr}$  prior to the laser processing. Then a  $6 \times 6$  matrix of laser processed areas was created by

varying the laser energy from  $0.7 - 1.4 \text{ J.cm}^{-2}$  and the laser pulses from 1 to 15. As indicated in figure 3.2 the sample was placed in the pressurised cell and laser processed under an over pressure of  $\text{O}_2$ , at 140 PSI.

### B.3.1.3 Photoluminescence (PL)

Figure B.7 show the PL emission from  $\text{Y}_2\text{O}_3:\text{Eu}$  thin film thermal annealed at  $400^\circ\text{C}$  and laser processed with 5 pulses in an  $\text{O}_2$  over pressure of 140 PSI. For  $\text{Y}_2\text{O}_3:\text{Eu}$  the  $^5\text{D}_0-^7\text{F}_2$  transition peak was at 611 nm, but with these experiment conditions, it has shifted to 613 nm. This may due to the thin film layers not being fully converted to  $\text{Y}_2\text{O}_3:\text{Eu}$  phosphor. With the increase of laser fluence, significant improvement of PL intensity was observed and with the higher fluences the thin film layer shows some ablation and PL intensity starts to decrease.

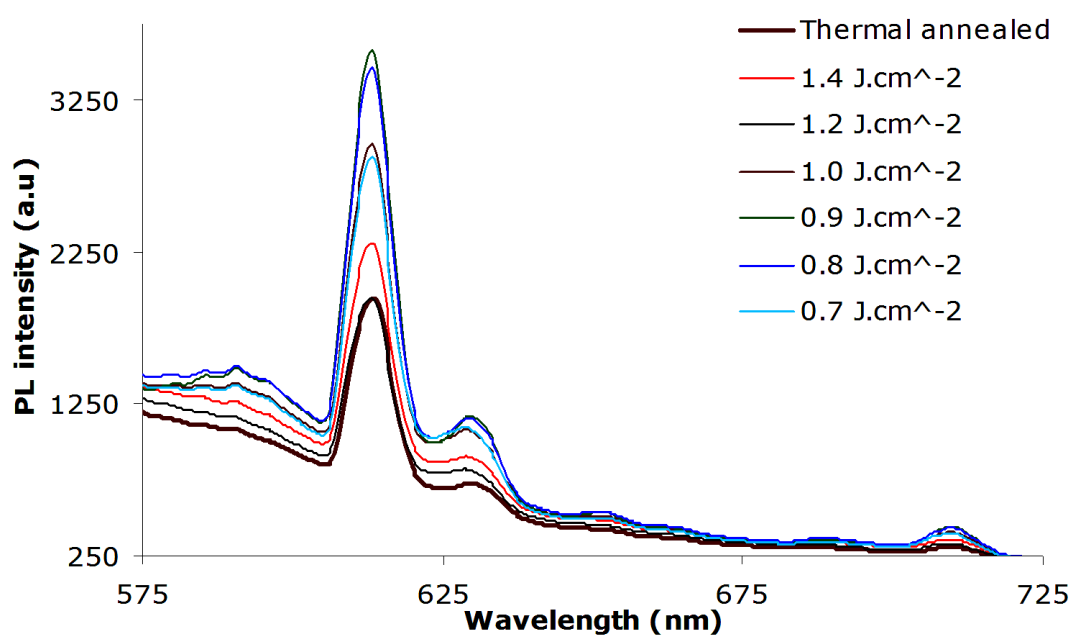


Figure B.7: PL emission of  $\text{Y}_2\text{O}_3:\text{Eu}$  thin films: thermal annealed at  $400^\circ\text{C}$  and laser processed with 5 laser pulses in 140 PSI  $\text{O}_2$ .

### ***B.3.2 Laser processing of Y<sub>2</sub>O<sub>3</sub>:Eu precursors on glass***

Subsequently, a new batch of Y<sub>2</sub>O<sub>3</sub>:Eu ink was formulated, but instead of using 'phosphor' particles, the ink was produced using the metal hydroxycarbonate phosphor precursor produced by Brunel University. The nanoparticulate ink was based on Y(OH)CO<sub>3</sub>:Eu(OH)CO<sub>3</sub> spheres and the urea precipitation method had been used to synthesis the precursors.

The sample preparation of Y<sub>2</sub>O<sub>3</sub>:Eu precursors was performed in two stages. Firstly nine samples of Y<sub>2</sub>O<sub>3</sub>:Eu precursor were inkjet printed onto glass substrates using the Xaar 126 printer head with different inkjet printing conditions to determine stable jetting and good wetting characteristics. The printing variables are; surface treatment, number of inkjet passes, printing speed and Micro-stepping. The samples inkjet printed with corona surface treatment and micro stepping showed better quality layers.

Initially, inkjet printed Y<sub>2</sub>O<sub>3</sub>:Eu samples were laser processed in air using ArF laser emitting at 193 nm. Few areas were laser processed with maximum and minimum possible fluences (0.88 J.cm<sup>-2</sup> and 1.9 J.cm<sup>-2</sup>) with 1 and 5 pulses respectively. The precursor layer was ablated with the higher number of laser pulses.

#### ***B.3.2.1 Photoluminescence (PL)***

Figure A.8 shows the PL emission spectra of laser processed Y<sub>2</sub>O<sub>3</sub>:Eu precursors. The excitation source used in this measurement was 266 nm. The prominent emission peak was observed around 615 nm.

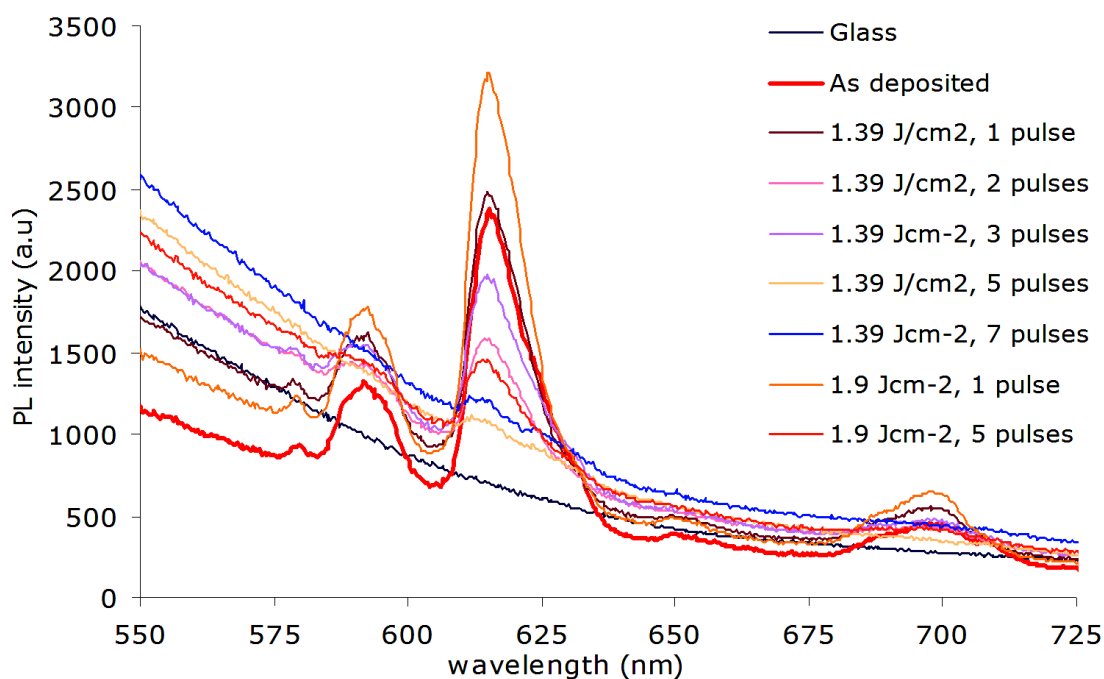


Figure B.8: PL spectra of laser processed  $\text{Y}_2\text{O}_3:\text{Eu}$  precursors on glass.

All the  $\text{Y}_2\text{O}_3:\text{Eu}$  samples prepared onto the glass substrate shows a fluorescence peak around 500 nm. Even though some improvement of PL was observed at  $1.9 \text{ J}\cdot\text{cm}^{-2}$  and  $1.39 \text{ J}\cdot\text{cm}^{-2}$  with single pulses, it is difficult to conclude due to fluctuation of this background fluorescence. Therefore the second batch of samples was deposited onto HOYA (fused silica) substrates to eliminate the background fluorescence during PL measurement.

### ***B.3.3 Laser processing of $\text{Y}_2\text{O}_3:\text{Eu}$ precursors on Fused silica***

The  $\text{Y}_2\text{O}_3:\text{Eu}$  precursor ink from PEL was used to prepare these samples. A pipette was used to drop some ink onto the HOYA substrate and dried at  $150^\circ\text{C}$  for an hour to remove the solvent residuals. Then the sample was laser processed using ArF laser (@ 193 nm) in an over pressure of Argon and Oxygen at 140 PSI respectively. The laser parameters varied for this experiment are laser fluences and number of pulses. By varying the number of laser pulses from 1 to 30 different areas was laser processed for the laser fluences from  $0.86 \text{ J}\cdot\text{cm}^{-2}$  to  $1.63 \text{ J}\cdot\text{cm}^{-2}$ .

### B.3.3.1 Photoluminescence (PL)

The PL of each processed area was then measured using 266 nm excitation. Figure B.9 (a) and (b), shows the PL emission from  $\text{Y}_2\text{O}_3:\text{Eu}$  thin films laser processed with respect to different number of laser pulses at  $1.3 \text{ J.cm}^{-2}$  and  $0.86 \text{ J.cm}^{-2}$  in an over pressure of Ar and  $\text{O}_2$  of 140 PSI respectively.

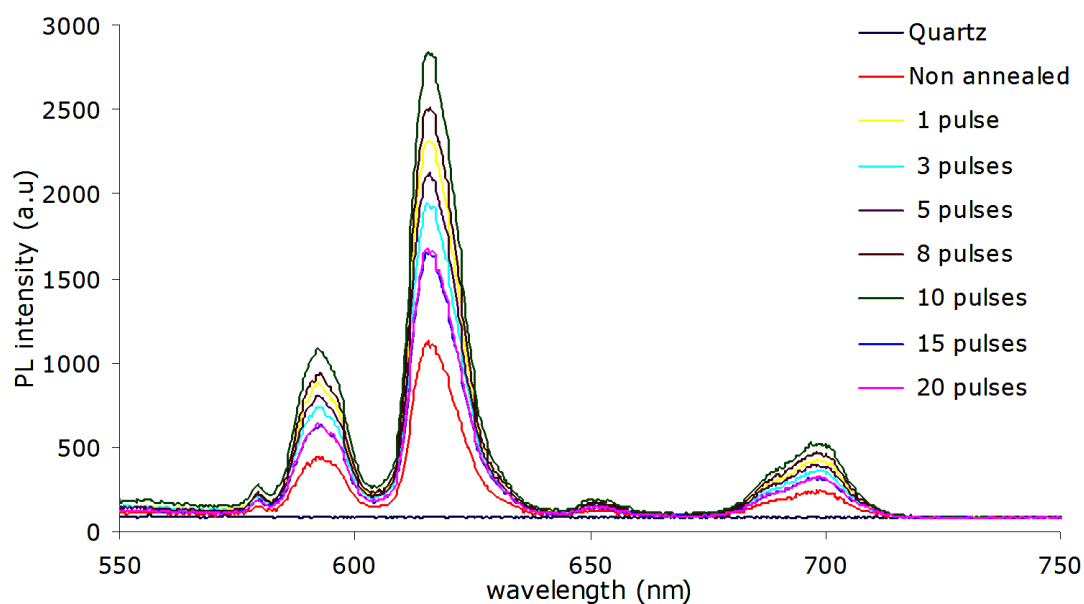


Figure B.9 (a): PL spectra of  $\text{Y}_2\text{O}_3:\text{Eu}$  laser processed with one to twenty pulses at  $1.3 \text{ J.cm}^{-2}$ , in an Ar over pressure of 140 PSI.

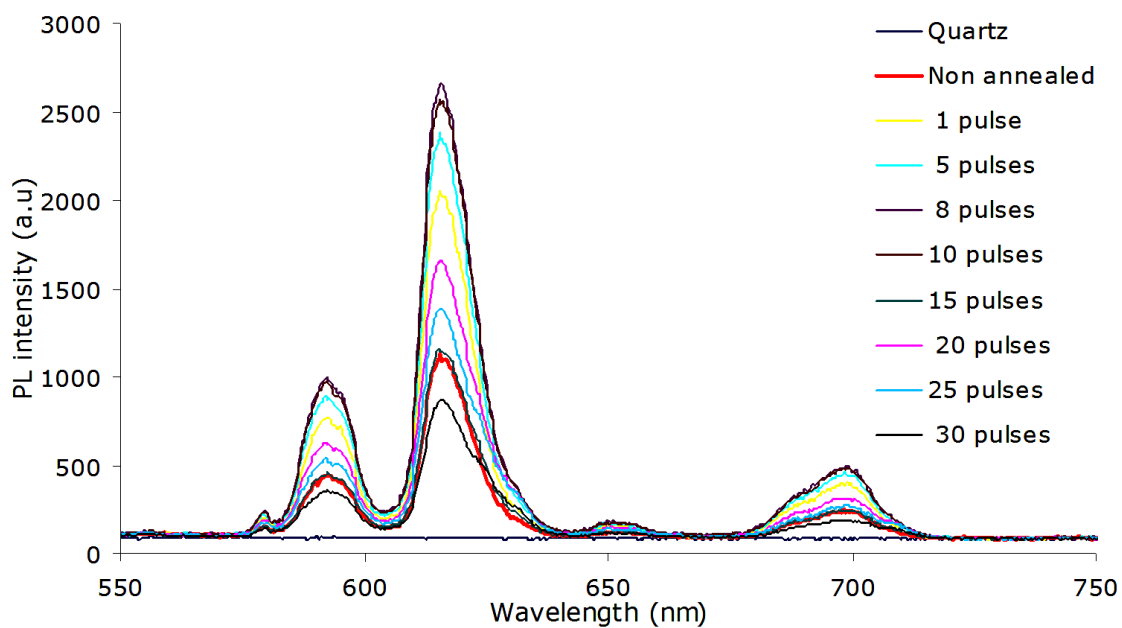
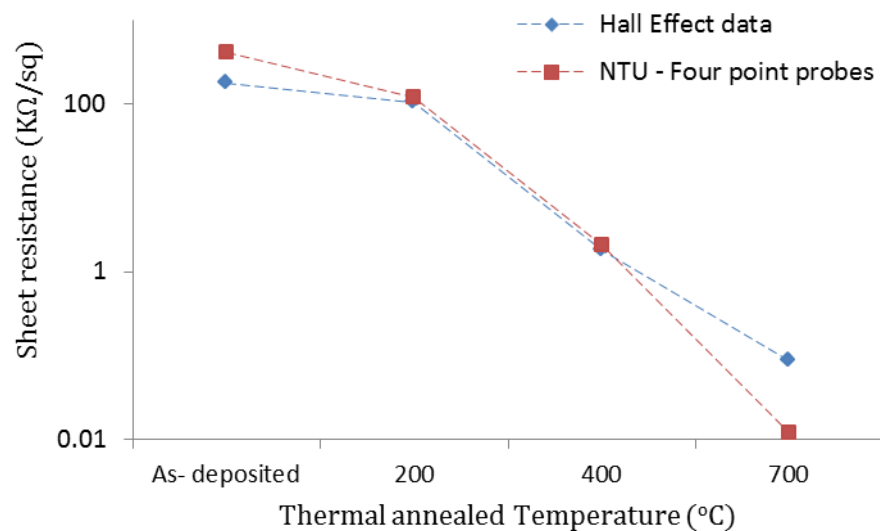


Figure B.9 (b): PL spectra of Y<sub>2</sub>O<sub>3</sub>:Eu laser processed with one to thirty pulses at 0.86 J.cm<sup>-2</sup>, in an O<sub>2</sub> over pressure of 140 PSI.

In both cases the Y<sub>2</sub>O<sub>3</sub>:Eu precursor shows significant improvement to its PL intensity with respect to the increase of number of pulses. At higher number of pulses the thin film layer shows some ablation and the PL intensity starts to lower. But still the shift in wavelength of the main peak was observed and the main peak corresponds to the energy transition from <sup>5</sup>D<sub>0</sub> - <sup>7</sup>F<sub>2</sub> has been shifted to the 616 nm.

## APPENDIX C-Comparison of sheet resistance measured by four point probes and using Hall Effect data

### 1. Thermal annealed SnO<sub>2</sub>:Sb



### 2. Excimer laser processed SnO<sub>2</sub>:Sb

